Implicit Coordinated Tactical Avoidance for UAVs within a Geofenced Airspace

Master of Science Thesis

D.C. van Wijngaarden

Technische Universiteit Delft

Implicit Coordinated Tactical Avoidance for UAVs within a Geofenced Airspace

Master of Science Thesis

by

D.C. van Wijngaarden

to obtain the degree of Master of Science
at the Delft University of Technology,

Student number:	4351185	
Thesis committee:	Dr. ir. M.M. van Paasen,	TU Delft, Chairman
	Dr. ir. J. Ellerbroek,	TU Delft, Supervisor
	Ir. B. D. W. Remes,	TU Delft, Supervisor
	Dr. O. A. Sharpanskykh,	TU Delft, Examiner

TU Delft

Preface

I would like to express my gratitude to my daily supervisors Joost Ellerbroek and Bart Remes for guiding me during my master thesis work. I would also like to thank Jacco Hoekstra who read my draft reports and attended my midterm presentation. Thank you all for all valuable feedback and critical questions which helped me to improve the quality of my graduation work.

I would also like to thank my friends, parents, family and fellow students who were always able to help me during my graduation project. I also shared a lot of good moments with them besides my graduation work.

D.C. van Wijngaarden
Delft, November 2020

List of Figures

List of Tables

Nomenclature

Abbreviations

ANSP	Air Navigation Service Provider
ATC	Air Traffic Control/Centre
ATM	Air Traffic Management
BVLOS	Beyond Visual Line of Sight
CC	Conflict Cone
CCW	Counter Clockwise
CD&R	Conflict Detection and Resolution
CPA	Closest Point of Approach
FBZ	Forbidden Beam Zone
FV	Forbidden Velocities
IRPZ	Intrusion Rate of the Protected Zone
LoS	Loss of Separation
MVP	Modified Voltage Potential
PZ	Protected Zone
RV	Reachable Velocities
SDPS	Surveillance Data Processing System
SSD	Solution Space Diagram
UAV	Unmanned Air Vehicle
UTM	UAV Traffic Management
VLOS	Visual Line of Sight
VO	Velocity Obstacle
VP	Voltage Potential
VRG	Violation Rate of Geofences

Symbols

$\hat{x}$	Unit vector directed in east direction
$\hat{x}''$	Unit vector $\hat{x}'$ rotated by ϕ'
$\hat{x}'$	Unit vector $\hat{x}$ rotated by ϕ
$\hat{y}$	Unit vector directed in north direction
$\hat{y}''$	Unit vector $\hat{y}'$ rotated by ϕ'

$\hat{y}^{'}$ Unit vector $\hat{y}$ rotated by ϕ

ϕ Rotation of a geofence vector with respect to the $\hat{x}$ unit vector

$\phi^{'}$ Half the angle between the $\hat{x}$ unit vector and a $\vec{d}_{int}$ vector

$\vec{d}_{int}$ Intruder Position Vector

$\vec{d}_{own}$ Own position vector

$\vec{d}_{rel}$ Relative position vector

$\vec{v}_{int}$ Intruder velocity vector

$\vec{v}_{own}$ Own velocity vector

$\vec{v}_{re;}$ Relative velocity vector

h_{PZ} Half the height of the PZ

R_{PZ} Horizontal radius of the PZ

t_{CPA} Time until reaching the CPA

t_{LA} Look-ahead time

Thesis Outline

This report describes the work that has been performed during this Master's thesis. The report is divided into the following two parts:

I Scientific Report

The scientific report gives and discussed the findings of the experiments that have been performed for the research described in this report.

II Preliminary Report

This report has already been graded and can be used as guidance material. The preliminary report gives the literature review and an extensive explanation of the derivation of the methods applied for the experiments that have been performed.

Contents

I

Scientific Paper

Tactical conflict resolution method for UAVs flying within a horizontally constrained airspace

Author: Dennis C. van Wijngaarden
Supervisors: Joost Ellerbroek, Bart D.W. Remes and Jacco M. Hoekstra

***Abstract*—This paper presents the derivation, implementation and safety assessment of a velocity obstacle based conflict resolution method to be used by UAVs flying within a horizontally restricted airspace by a geofence under the presence of wind. Two parameters indicating the safety of the applied conflict resolution method have been measured, i.e., the Intrusion Prevention Rate (IPR) and the Violation Prevention Rate of the Geofence (VPRG). Three coordination rule-sets have been implemented i.e., 1) geometric optimum (OPT), 2) geometric optimum from target heading (DEST) and 3) only change in heading (HDG). These rule-sets have been assessed during a safety assessment. It was concluded that the OPT rule-set performed best in terms of the IPR and the DEST rule-set performed best in terms of the VPRG under windy and wind calm conditions. The HDG rule-set performed worst in terms of both safety parameters. It was noted that both safety parameters are the lowest when conflicts occur close the geofence under windy conditions for all implemented rule-sets.**

***Index Terms*—Unmanned Aerial Vehicle, conflict detection and resolution, air traffic management, uav traffic management, solution space diagram, velocity obstacle**

I. Introduction

TODAY, the demand of Air Traffic Management (ATM) services is huge in order to ensure safe aeronautical operations. Recently, many advancements have been achieved regarding Unmanned Aerial Vehicles (UAVs) or better known as drones. These advancements lead to a reduction in operational costs and an increasing demand to those aerial robots. Research is being done to a similar system like ATM which is to be applied to UAVs in order to guarantee safe aeronautical operations in the future [1].

One of the key features of the Unmanned Traffic Management (UTM) system that is currently being developed should ensure that all UAVs stay clear of manned aviation and each other which is in accordance with the concept of operation defined by NASA [2]. Furthermore, all UAVs and their operators should be aware of the operational constraints and obstacles within a given airspace they operate in. Therefore, there is a need to incorporate Conflict Detection and Resolution (CD&R) methods within the UTM system to fulfil this feature.

However many CD&R methods have already been investigated for manned aviation within the ATM system, these methods cannot simply be applied to the UTM system due to differences in operational constraints, manoeuvres, functions, control and operational ranges of UAVs [3]. Therefore, this paper discusses the adaptation and extension of existing velocity obstacle based conflict resolution methods that have already been investigated for manned aviation [4]–[6]. Some research on velocity obstacle based conflict resolution methods have also been performed in simulation for UAVs [7], [8].

The research presented in this paper will contribute to the development of a reliable conflict resolution method to be applied in the UTM system. Although some research has already been done on conflict resolution methods for UAVs, the current research will focus on the influence of geofences and wind on the safety performance of these conflict resolution methods. A geofence is the border of a horizontally enclosed airspace in which an UAV is allowed to operate. No previous research has been performed that takes into account a geofence in the generated conflict resolution whereas the geofence is limiting the number of avoidance manoeuvres that can be performed. Furthermore, the shape of a geofence can be arbitrary for which the methods for the generation of velocity obstacles for circular shaped objects cannot be applied. Another research is done on the generation of velocity cones for arbitrary shaped objects [9]. Although a geofence can be seen as arbitrary shaped static obstacle, the velocity cone method cannot be applied to it as the own vehicle is encapsulated within the geofence resulting in a set of adjacent velocity cones spanning all possible directions. Therefore, it is inevitable to find a conflict resolution without converging to a fraction of the geofence boundary. Thus, it must be reviewed for each conflict resolution if the point at which a conflict is resolved lies within the geofence instead of reviewing if a instantaneous velocity resolution vector crosses a geofence in the future, which always happens if the magnitude of the ground speed is not equal to zero. The relative speed and position of conflicting vehicles and the selected conflict resolution determine the location at which a conflict is resolved. Then, this point needs to be validated to be located within the geofence for a valid conflict resolution. Therefore, a geofence cannot be seen as an obstacle itself but must be evaluated in combination with the geometric parameters of a conflict. Another aspect that can influence the safety performance of a conflict resolution method is the wind. In general, the operational speed at which an UAV operates is lower than for manned vehicles which makes the contribution of the wind bigger for UAVs, especially near geofences through which UAVs can be blown during conflict resolution manoeuvres. Therefore, the objective of this research is to contribute to a robust CD&R algorithm to be used on UAVs, regarding how to adapt existing CD&R techniques in order to provide an implicitly coordinated tactical CD&R approach, taking into account the limitations of geofences combined with wind by defining a set of avoidance rules to be assessed by simulations implementing adaptations of existing implicitly coordinated tactical CD&R algorithms developed for manned aviation. The conflict resolution method discussed in this work is a two dimensional method which will only find conflict resolutions in the horizontal plane. The geometry of the geofence needs to be convex for the implemented method.

This paper is structured as follows: section II describes a velocity based obstacle method that is implemented as basis for the method analysed in this paper. The resolution rule-sets that are used for the experiments described in this paper are discussed in this section as well. Section III gives the derivation of an extension of the velocity obstacle based method such that the segments of a convex geofence can be modelled as ”virtual” velocity obstacles. This section also describes how a velocity obstacle based conflict resolution method can be corrected for wind. Section IV describes the set-up of the experimental simulations. It also elaborates on the variables that are dependent and independent in the series of experimental simulations. Then, section V describes the method and parameters used for the generation of semi-random scenarios for the experimental test series. Section VI gives an overview of the results which are discussed in more depth by section VII. Finally, section VIII concludes the work and provides recommendations for future research.

II. Velocity obstacle based conflict resolution method

This section briefly describes the notion of velocity obstacles (VOs) and how these are applied within a CD&R method. The basics of velocity obstacles are explained first. Secondly, the construction of a solution space diagram (SSD) from VOs and flight envelope limits of an UAV is described. Finally, coordination rule-sets that have been implemented to calculate conflict resolutions from a SSD are explained.

A. Velocity obstacles

The theory about velocity obstacles originates from the robotics industry and is used as the basis for dynamic obstacle avoidance algorithms [10]. A velocity obstacle (VO) of a dynamic object is the set of absolute velocity vectors that lead to a collision with the object in the future. The way a VO is constructed is discussed by this section.

First of all, a so called Conflict Cone (CC) needs to be constructed before a VO can be generated. A CC is defined in the relative velocity space where the dynamic obstacle can be seen as a static object because the obstacle's speed vector is subtracted from the own speed vector in this space. A CC is the triangular relative velocity space between lines drawn from the own vehicle tangent to the edges of a circular shaped obstacle as can be seen at the left side of figure 1. The circular obstacle can be seen as the protected zone (PZ) of an UAV which is located in the centre. The protected zone needs to stay clear from other traffic during operation and its radius is set to 50 meters as already been used by other studies [1], [7], [8]. An intrusion will occur when the relative velocity vector of the own vehicle with respect the obstacle points inside the space constructed for the CC. The relative velocity vector $\vec{v}_{rel}$ is the own vehicle's velocity vector $\vec{v}_{own}$ minus the obstacle's velocity vector $\vec{v}_{obs}$.

Secondly, a Velocity Obstacle (VO) can be constructed in the absolute velocity space by translating the CC by the obstacle's velocity vector $\vec{v}_{obs}$. The own vehicle is in conflict when its absolute velocity vector $\vec{v}_{own}$ is pointing inside the constructed VO. The advantage of VOs with respect to CCs are that they can be combined in the same space with VOs of other obstacles. A graphical representation of a VO is presented at the right side of figure 1. It can also be seen in the figure that the VO is translated by the obstacle's speed vector $\vec{v}_{obs}$. The figure indicates that the own vehicle is in conflict with the dynamic obstacle as the own speed vector points into the VO.

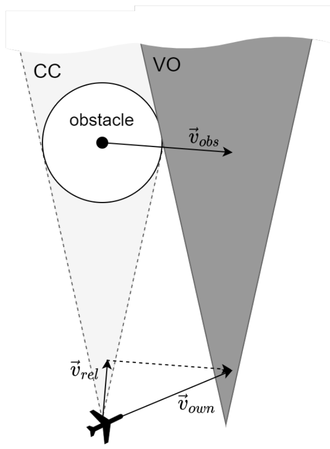

Fig. 1. Graphical representation of a Conflict Cone (CC) and Velocity Obstacle (VO).

B. Solution Space Diagram

A Solution Space Diagram (SSD) is a graphical representation of the sets of reachable velocities that lead to conflict-free and conflicting flight paths. Details on how such a diagram can be constructed are described by Ellerbroek [4] and Mercado [5]. This section shortly describes the construction and applications of the SSD.

The first step in constructing a SSD is to constrain the manoeuvring space by the aerial vehicle's maximum and minimum speed limits. This means that for rotorcraft and hybrid UAVs that there is no minimum speed limit because those vehicles are able to hover with zero horizontal velocity. The set of velocities that are within the minimum and maximum speed limits are the reachable velocities (RV). A two dimensional representation of the RV is given by figure 2a.

Secondly, the union of all VOs for each intruder is constructed and referenced as the Forbidden Velocities (FV). A graphical representation of the forbidden velocities can be found in figure 2b.

Finally, The intersection of the RV and FV is denoted as the Forbidden Reachable Velocities (FRV) which is the set of reachable velocities that will emerge a conflict with an intruder. The difference between the RV and the FV is denoted as the Achievable Reachable Velocities (ARV) which is the

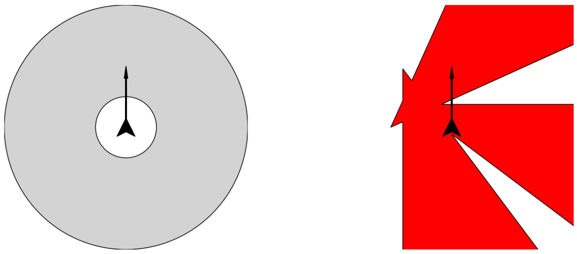

(a) Reachable velocities (RV). (b) Forbidden Velocities (FV).

Fig. 2. Visual representation of reachable and forbidden velocities.

set of reachable velocities for which the flight path is free of conflicts. The goal of a conflict resolution method that relies on velocity obstacles is to find a velocity vector that is within the ARV in order to have a conflict free flight path. A graphical representation of a final SSD is given by figure 3 which visualises the achievable and forbidden reachable velocities.

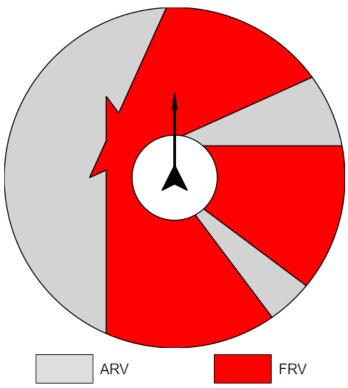

Fig. 3. SSD visualising the ARV and FRV.

C. Coordination rule-sets

Several coordination rule-sets have already been applied on velocity obstacle based conflict resolution methods in order to find conflict free paths. Borst et al. [6] for example used the SSD as a supervisory tool for air traffic controllers to aid them to select efficient and conflict free flight paths. Jenie et al. [7], [8] have applied the rules of the air as rule-set to find an implicitly coordinated conflict resolution. Another rule-set that has been applied by Ellerbroek [11] is the geometrically optimal solution. The geometric optimum conflict resolution is the velocity vector pointing in the ARV that has the smallest distance with respect to the current velocity vector. The geometric optimum conflict resolution is equal to the resolution that is calculated by the Modified Voltage Potential (MVP) conflict resolution method for single aircraft conflicts and some multi aircraft conflicts [12]. However, this does not always hold when velocity obstacles generated for geofence segments are implemented in a velocity obstacle based conflict resolution method.

The rule-set that adheres to the rules of the air can already be excluded from the current research as this rule-set cannot be applied on a head-to-head conflict for two vehicles flying close and parallel to a geofence segment as there is not enough resolution space towards this geofence segment for an avoidance manoeuvre. Therefore, only resolution rule-set can be used that are allowed to find resolutions in every direction such that conflict resolutions cannot push an UAV towards a geofence border.

The geometric optimal rule-set can be used for the current research. Also two other rule-sets can simply be derived from the geometric optimum strategy: shortest path from target heading and resolving only by changing heading [13]. The shortest path from target heading uses the same method as the geometric optimal rule-set, except that the closest resolution velocity vector is being found relative to a speed vector directed to the target location instead of the actual speed vector. The change by heading rule-set only changes the direction of the speed vector, but keeps airspeed constant. All resolution rule-sets and their abbreviations that are used throughout this paper are listed below:

- **OPT**: geometric optimum solution.
- **DEST**: geometric optimum from target heading.
- **HDG**: only change the velocity vector in terms of heading, not in magnitude.

A graphical presentation of the resolution points calculated for each rule-set is given by figure 4. It can be seen that different resolution points have been calculated for each rule-set.

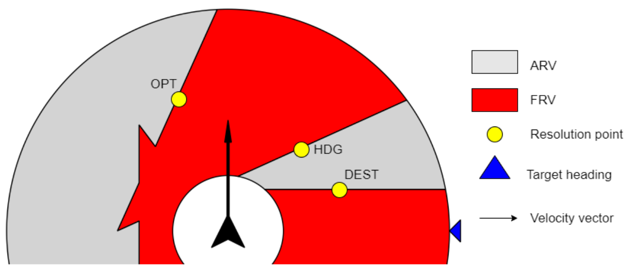

Fig. 4. Resolution points for each rule-set.

D. Resolution manoeuvre

The steps to take in order to perform a conflict resolution manoeuvre are described by this section. A vital variable to keep track of when performing a conflict resolution manoeuvre is the Closest Point of Approach (CPA). The CPA is the location at which the distance between two vehicles is at minimum for their current flight paths. Two vehicles are diverging if the CPA has been passed. A current conflict resolution manoeuvre can be ended at this point as the resolving vehicles are diverging from each other from this point onward. Therefore, this point will be referenced as the recovery point throughout this paper. The relative distance of two conflicting vehicles at the recovery point is the radius of the protected zone plus some margin during a successful conflict resolution manoeuvre. An autonomous conflict resolution manoeuvre can be performed by executing the following steps [7]:

1) Calculate a conflict resolution for the conflict according to the selected rule-set.
2) Perform a conflict resolution manoeuvre by changing the current velocity vector to the resolution speed vector.
3) Maintain the resolution speed vector until the recovery point has been passed. Reevaluate if the current flight path is conflict free, if not, go back to the first step.
4) Finally, after the recovery point has been passed, direct the flight path towards the target again to resume the mission.

E. CD&R parameters

The parameters used for the implemented velocity obstacle based conflict resolution method are given in table I. The radius of the protected zone is the radius of the circle around an UAV that has to stay clear of other traffic during operation. A Loss of Separation (LoS) occurs when another vehicle enters the protected zone. The lookahead time of the conflict detection method is the maximum time until a LoS is predicted for which a conflict resolution is performed. The simulation time is the time each scenario in the simulation test series is executed for this research.

TABLE I
PARAMETER RANGES FOR THE APPLIED CD&R METHOD

Parameter	Range	Unit
Radius of protected zone, R_{PZ}	50	[m]
Lookahead time, t_{LA}	25	[s]
Total simulation time, T	180	[s]

III. ADDING GEOFENCES TO A VELOCITY OBSTACLE BASED CD&R METHOD

This section describes the extension of the previously explained velocity obstacle based conflict resolution method when wind and geofences are implemented. First of all, the definition of a geofence is explained. Then, the math behind the generation of "virtual" velocity obstacles for geofence segments is discussed. Finally, an explanation is given on how the SSD can be adapted in order to incorporate wind in combination with geofences.

A. Geofence definition

The velocity obstacle based conflict resolution method needs to be extended in order to account for the fact that a conflict resolution has to be found within a predefined area that is horizontally constrained by a geofence. The method described by this paper can only be used for convex geofences consisting of n linear geofence segments $\vec{r}_i$ as given by equation 1. The $\vec{a}_i$ and $\vec{b}_i$ vectors are the start and end point of geofence segment i respectively. Each end point of geofence segment i is the start point of geofence segment $i+1$. The start point of geofence segment 0 is the end point of geofence segment n in order to have a closed geofence. A geofence is defined positive counter clockwise throughout this paper.

$$\vec{r}_i = \vec{a}_i + \lambda\left(\vec{b}_i - \vec{a}_i\right) \tag{1}$$

A graphical presentation of a geofence is given by figure 5. The figure shows a convex geofence that is defined counter clockwise. The area that the goefence encloses is the airspace allowed to be used for a mission. It can also be seen that each start point of a geofence segment is the end point of the previous geofence segment.

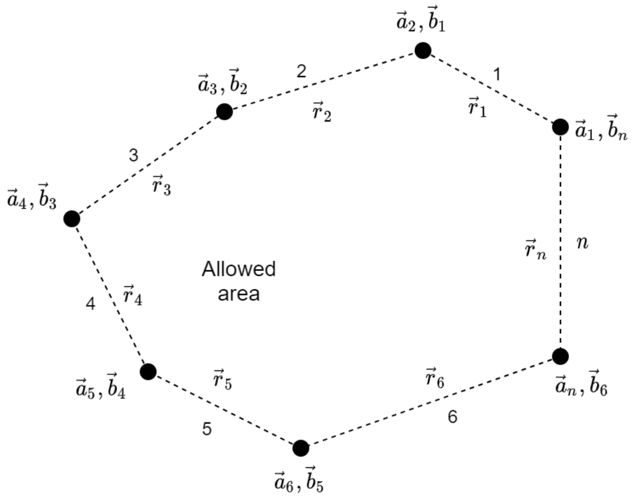

Fig. 5. Convex geofence of n segments

B. Mathematics

This section describes the mathematics behind the generation of "virtual" velocity obstacles for geofence segments. As already mentioned in section II-D, the location where two conflicting vehicles start to diverge can be set as the resolution location as both vehicles are allowed to turn back to their targets from this point onward. This point was referenced as the recovery point before. Therefore, it is important to find a set of points on the SSD which indicates where the recovery point with an intruder coincides with a given geofence segment. Marking those points on a SSD as "virtual" velocity obstacles can help to find conflict resolutions for which the recovery point lies within the geofence of a horizontally constrained airspace. Therefore, a set of resolution speed vectors $\vec{v}_{res}$ has to be found for which a conflict free path can be ensured and for which the recovery point is located within the geofence. This set of resolution speed vectors can be be visualised on a SSD as the ARV.

Equation 2 gives the position vector to the recovery points as function of a two dimensional resolution speed vector $\vec{v}_{res}$. The position of the ownship is taken as origin of the reference system and $\vec{d}_{int}$ is the intruder position vector. The $\vec{v}_{int}$ vector is the two dimensional speed vector of the intruder.

$$\vec{p}_{rec}\left(\vec{v}_{res}\right) = \frac{\vec{d}_{int}\cdot\left(\vec{v}_{res}-\vec{v}_{int}\right)}{\left(\vec{v}_{res}-\vec{v}_{int}\right)\cdot\left(\vec{v}_{res}-\vec{v}_{int}\right)}\vec{v}_{res} \tag{2}$$

The line equations of each geofence segment i given by equation 1 should be equal to equation 2 in order to find a set of resolution velocity vectors for which the recovery point coincides with the geofence segment. The set of resolution velocity points constructs the border of the ”virtual” velocity obstacle for a given intruder and a given geofence segment. Therefore, equation 3 needs to be solved for the resolution speed vector in order to construct the velocity obstacle for geofence segment i.

$$\vec{v}_{res}\frac{\vec{d}_{int}\cdot(\vec{v}_{res}-\vec{v}_{int})}{(\vec{v}_{res}-\vec{v}_{int})\cdot(\vec{v}_{res}-\vec{v}_{int})}=\vec{a}_i+\lambda\left(\vec{b}_i-\vec{a}_i\right) \quad (3)$$

Working out equation 3 results in equation 4 which gives the equation for the boundary of the ”virtual” velocity obstacle for geofence segment i. The geometry of the velocity obstacle can be elliptical, parabolic or hyperbolic depending on the sign of the b_i^2 variable. The velocity obstacle is defined along the $\hat{x}_i^{''}$ and $\hat{y}_i^{''}$ unit axes, which are rotated by the sum of the ϕ_i and $\phi_i^{'}$ angles visualised in figures 6 and 7 respectively.

$$\frac{\left(\vec{v}_{res}\cdot\hat{x}_i^{''}-C_{x_i^{''}}\right)^2}{a_i^2}+\frac{\left(\vec{v}_{res}\cdot\hat{y}_i^{''}-C_{y_i^{''}}\right)^2}{b_i^2}=1 \quad (4)$$

Figure 6 gives a graphical representation of the geofence segment aligned reference system with primary axes $\hat{x}_i^{'}$ and $\hat{y}_i^{'}$. The geofence segment aligned reference system is rotated by angle ϕ_i with respect to the initial (east, north) reference system such that the $\hat{x}_i^{'}$ primary axis is aligned with the geofence segment from $\vec{a}_i$ to $\vec{b}_i$. The $\hat{y}_i^{'}$ primary axis points always inside the enclosed geofenced area as the geofence is defined counterclockwise (CCW).

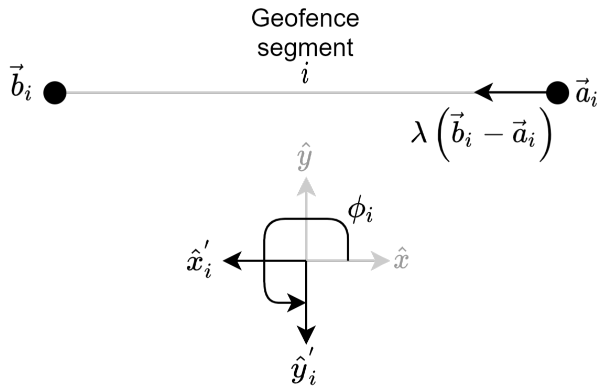

Fig. 6. Geofence segment aligned axis system rotated by ϕ_i

Figure 7 gives a representation of the axis system aligned with the ”virtual” velocity obstacle for a geofence segment. The $\hat{x}_i^{''}$ and $\hat{y}_i^{''}$ axes are the primary axes of this axis system respectively. The ”virtual” velocity obstacle aligned reference system is rotated with angle $\phi_i^{'}$ with respect to the previously defined geofence segment aligned reference system. The rotation angle $\phi_i^{'}$ depends on the relative position of the intruder with respect to the ownship in the geofence segment aligned reference system as shown in the figure. The rotation angle $\phi_i^{'}$ is mathematically presented by equation 5.

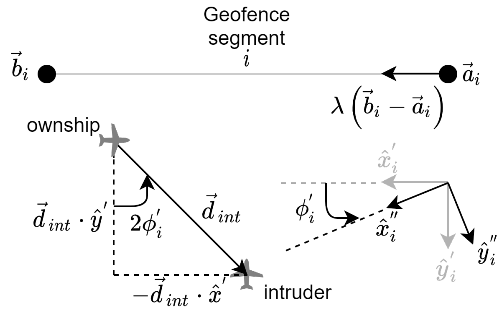

Fig. 7. Axis system of ”virtual” velocity obstacle of geofence segment i rotated by $\phi_i^{'}$ with respect to the geofence aligned axis system.

$$\phi_i^{'}=\frac{1}{2}\tan^{-1}\left(\frac{-\vec{d}_{int}\cdot\hat{x}_i^{'}}{\vec{d}_{int}\cdot\hat{y}_i^{'}}\right) \quad (5)$$

The x and y coordinates of the origin of the ”virtual” velocity obstacle for geofence segment i are given by equations 6 and 7 respectively. Note that the origin coordinates are given in the ”virtual” velocity obstacle aligned reference system along the $\hat{x}_i^{''}$ and $\hat{y}_i^{''}$ axes. The expressions for variables C_1, C_2, C_3 and C_4 are given by equations 8 - 11 respectively. The d_{geo_i} variable is the distance of the own vehicle with respect to geofence segment i.

$$C_{x_i^{''}}=-\frac{C_3}{2C_1} \quad (6)$$

$$C_{y_i^{''}}=-\frac{C_4}{2C_2} \quad (7)$$

$$C_1=\left(1+\sin\left(\phi_i^{'}\right)\frac{\vec{d}_{int}\cdot\hat{x}_i^{''}}{d_{geo_i}}\right) \quad (8)$$

$$C_2=\left(1+\cos\left(\phi_i^{'}\right)\frac{\vec{d}_{int}\cdot\hat{y}_i^{''}}{d_{geo_i}}\right) \quad (9)$$

$$C_3=\left(-2\left(\vec{v}_{int}\cdot\hat{x}_i^{''}\right)-\sin\left(\phi_i^{'}\right)\frac{\vec{d}_{int}\cdot\vec{v}_{int}}{d_{geo_i}}\right) \quad (10)$$

$$C_4=\left(-2\left(\vec{v}_{int}\cdot\hat{y}_i^{''}\right)-\cos\left(\phi_i^{'}\right)\frac{\vec{d}_{int}\cdot\vec{v}_{int}}{d_{geo_i}}\right) \quad (11)$$

The squared values of the semi-major axes of the ”virtual” velocity obstacle are given by equations 12 and 13.

$$a_i^2=\frac{-\mid\vec{v}_{int}\mid^2+C_2C_{y_i^{''}}^2}{C_1}+C_{x_i^{''}}^2 \quad (12)$$

$$b_i^2=\frac{-\mid\vec{v}_{int}\mid^2+C_1C_{x_i^{''}}^2}{C_2}+C_{y_i^{''}}^2 \quad (13)$$

C. Geometry

This section gives insight in the geometry of a ”virtual” velocity obstacle that is generated for an intruder and geofence segment. A reference scenario with five reference positions for intruders has been defined for which ”virtual” velocity obstacles for a geofence segment are visualised in this section. A top view of the reference scenario is given by figure 8. Five possible reference positions of the intruders are given in the figure. Those positions are located somewhere around the ownship which is indicated by the big black circle. The ownship is located at a distance of d_{geo} relative to a geofence segment running from $\vec{a}$ to $\vec{b}$. The groundspeed of the intruders in the scenario is set to 10 m/s directed to the west. The groundspeed of the ownship is 10 m/s directed to the north. Examples of ”virtual” velocity obstacles that can be constructed for this reference scenario are further discussed in this section.

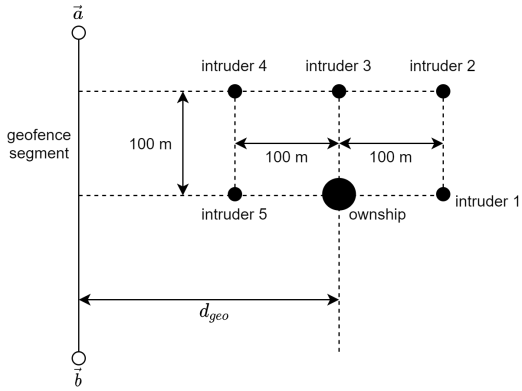

Fig. 8. Reference scenario for the generation of ”virtual” velocity obstacles for a geofence segment.

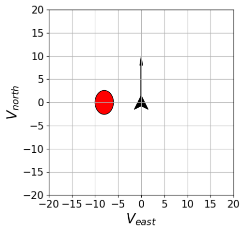

(a) ”Virtual” VO for the position of intruder 1.

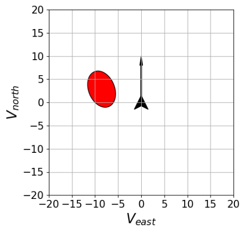

(b) ”Virtual” VO for the position of intruder 2.

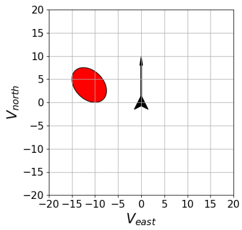

(c) ”Virtual” VO for the position of intruder 3.

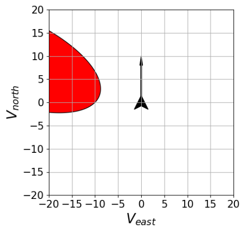

(d) ”Virtual” VO for the position of intruder 4.

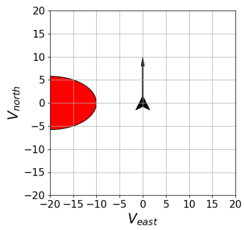

(e) ”Virtual” VO for the position of intruder 5.

Fig. 9. ”Virtual” velocity obstacles constructed for the geofence segment for each reference intruder position and $d_{geo} = 150m$.

The first aspect of the ”virtual” velocity obstacles that has been visualised is the effect that the relative position of an intruder has on the ”virtual” velocity obstacle generated for a geofence segment. The five diagrams displaying the geometry of the ”virtual” velocity obstacle for each intruder position in the reference scenario are visualised by figure 9. The distance of the ownship with respect to the geofence d_{geo} is set to 150 meters for the generation of those diagrams. In the first place, it can be noted that the axes of the ”virtual” velocity obstacle rotate by 90 degrees comparing the VO for the intruder at position 1 and position 5 with each other. This is because of the $\phi^{'}$ angle which increases from 0 degrees for intruder 1 to 90 degrees for intruder 5. It can therefore be notified that the ”virtual” VO rotates 90 degrees in total comparing the VOs for intruder 1 and intruder 5 with each other. The VOs for other intruders are rotated by $\phi^{'}$ angles ranging from 0 to 90 degrees. A second aspect that can be notified is that the ”virtual” velocity obstacle generated for intruder 4 is the largest whereas the size of the VO for intruder 1 is the smallest. Finally, all velocity obstacles generated for this example are ellipses as the b^2 variable for each VO is greater than zero.

The second aspect that has been visualised for the ”virtual” velocity obstacles is the effect the distance of the ownship with respect to the geofence has on the geometry of the ”virtual” VO. The position of intruder 2 in the reference scenario has been selected to construct ”virtual” VOs. A set of four ”virtual” VOs are visualised by figure 10 for a variety of distances with respect to the geofence of the ownship. The effect that can be notified is the negative relationship between the size of the ”virtual” VO and the distance with respect to the geofence. It can be seen from the figures that the size of the ”virtual” VO drastically increases for decreasing distance to the geofence. Figures 10a, 10b and 10c show an elliptical shaped VO whereas figure 10d shows a hyperbolic VO. This is because the b^2 variable turns negative for small distances to the geofence segment.

Another effect that has been discovered during the derivation of the ”virtual” velocity obstacle equation is that the component of the intruder’s velocity vector along the x axis of the geofence segment aligned reference system results in a pure translation of the ”virtual” VO in the same direction and with the same magnitude as this component. Therefore, it can be concluded that only the component of the speed vector of an intruder perpendicular to a geofence segment is a scaling factor for the size of a ”virtual” velocity obstacle.

A visual representation of the solution space diagram with a traditional velocity obstacle combined with a ”virtual” velocity

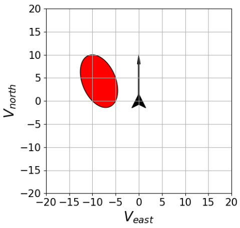

(a) ”Virtual” VO for d_{geo} = 100m.

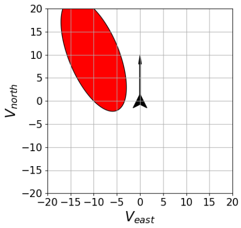

(b) ”Virtual” VO d_{geo} = 50m.

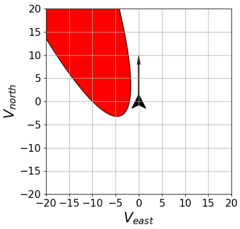

(c) ”Virtual” VO d_{geo} = 25m.

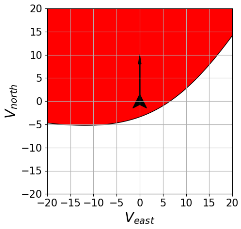

(d) ”Virtual” VO d_{geo} = 10m.

Fig. 10. ”Virtual” velocity obstacles constructed for the geofence segment for a variety of d_{geo} values based on intruder 2 of the reference scenario.

obstacle for a geofence segment is given by figure 11. The figure is constructed for intruder 2 of the reference scenario and at a distance of 100 meters with respect to the geofence.

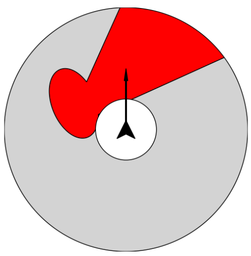

Fig. 11. The SSD for a traditional velocity obstacle of intruder 2 combined with a ”virtual” velocity obstacle for a geofence segment at d_{geo} = 100m.

D. Influence of wind on the VO based conflict resolution method

Wind has an influence on a velocity obstacle based conflict resolution method when velocity obstacles are being generated from earth fixed features such as geofences. In manned aviation, every aircraft involved in a conflict flies in about the same wind conditions for which the SSD can be generated in a body fixed reference system. However, when earth fixed velocity obstacles are being involved in the method, two corrections can be made to the SSD to correct for wind.

The first way to correct a solution space diagram for wind is to generate the diagram from an earth fixed perspective. This means that the ground speed is represented on the SSD instead of airspeed. The set of reachable velocities on the SSD that are constrained by the minimum and maximum speed of the flight envelop need to be translated by the wind vector as the sum of airspeed and wind is equal to the groundspeed. This means that the minimum an maximum groundspeed that is achieved with tailwind is higher than with headwind.

The second way to correct a SSD for wind is to construct the diagram from a body fixed perspective. This means that the airspeed is represented on the SSD. In this case, velocity obstacels that emerge from earth fixed obstacles need to be corrected for the wind in order to construct them in a body fixed reference system. This can be done by translating these velocity obstacles by the negative wind vector because airspeed is equal to groundspeed minus wind.

IV. Simulations

The outline of the simulations that have been performed for this research is presented in this section. First of all, the simulation software that has been used is introduced. Then, the dependent variables that are measured during simulations are introduced followed by a discussion on the hypotheses that have been tested in order to achieve the objective of this research. Finally, an overview of the simulation set-up is given.

A. BlueSky

A series of simulations have been executed in the open source BlueSky ATM simulator [14]. The simulator is developed and maintained by researches of the faculty of aerospace engineering of Delft University of Technology. BlueSky provides tools to simulate elements of the ATM system such as CD&R methods. The simulator provides plugin templates for CD&R methods in order to apply novel methods and strategies during simulations. BlueSky uses the OpenAP aircraft performance model in order to simulate dynamics of air vehicles [15]. The default parameters of the aircraft models that have been programmed in BlueSky are given by table II. The vertical motion parameters have been left out because the CD&R algorithm tested by this research only generates resolution manoeuvres in the horizontal plane. The table gives values for the acceleration, deceleration and maximum bank angle. The bank angle defines the turn rate of a vehicle. The dynamics for roll motion are not taken into account by the OpenAP aircraft model as the roll angle is directly set to the value of the maximum roll angle if a turn has to be made. The minimum, maximum and initial speeds of simulated aerial vehicles are randomly assigned for each scenario.

TABLE II
Standard parameters of aircraft model programmed in BlueSky ATM simulator

Parameter	Value	Unit
Horizontal acceleration / deceleration	0.5	m/s^2
Maximum bank angle	30	degrees

However BlueSky does not simulate the UTM system by default, the simulator can easily be adapted to simulate parts of the UTM system by changing constants and thresholds that are different than for manned aviation. An extension of a velocity obstacle based conflict resolution method is implemented in BlueSky as new plugin such that ”virtual” velocity obstacles of geofence segments are generated for conflicts.

B. Dependent variables

This section describes the dependent variables that have been measured during the simulations. The goal of this research is to assess the influence of geofences and wind on the applied conflict resolution method in terms of safety. The safety of an UAV can be compromised in two types of situations: an intrusion of the protected zone or a geofence violation. Therefore, two dependent variables assessing these safety criterion have been measured during simulations.

The first dependent variable that has been measured for each simulation test-series is the Intrusion Prevention Rate (IPR) which is given by equation 14 [13]. The IPR is the number of conflict resolution manoeuvres for which there was no loss of separation divided by the total number of conflicts encountered. The range of the IPR runs from 0 to 1. Values close or equal to 1 indicate good performance in terms of intrusion prevention. the n_{cnf} variable represents the number of conflicts and the n_{int} variable represents the number of intrusions.

$$IPR = \frac{n_{cnf} - n_{int}}{n_{cnf}} \tag{14}$$

The second dependent variable that has been measured for each scenario is the Violation Prevention Rate of the Geofence (VPRG) which is given by equation 15. The VPRG is the fraction of times a geofence has not been violated during a conflict divided by the total number of conflicts encountered. The number of conflicts n_{cnf} is multiplied by 2 in the numerator and denominator in the equation because two vehicles are involved in each conflict which can both violate a geofence. So a maximum of two geofences can be violated during each conflict as both vehicles in the conflict can violate the geofence during a conflict resolution manoeuvre. The range of the VPRG runs from 0 to 1. Values equal or close to 1 indicate good performance in terms of geofence violation prevention. The n_{vio} variable represents the number of geofence violations.

$$VPRG = \frac{2n_{cnf} - n_{vio}}{2n_{cnf}} \tag{15}$$

C. Hypotheses

The current research investigates the effect of geofences and wind on the safety performance of the implemented velocity obstacle based CD&R method. The performance is expressed in terms of the dependent variables presented in the previous section. The goal of this research is to contribute to a robust conflict resolution method to be applied on UAVs by assessing the performance of the implemented method for a variety of geofence geometries and wind conditions. Therefore, the following hypotheses which are stated below have been tested in simulation in order to determine the influence of geofences and wind on the performance parameters. A short elaboration on each hypothesis is also given.

1) Hypothesis 1: The IPR of the CD&R method is negatively correlated with the implementation of geofences: It is expected that the number of intrusions of the protected zone is higher for scenarios where geofences are implemented with respect to scenarios without geofences implemented. This is expected because the "virtual" velocity obstacles constructed for geofence segments reduce the solution space in terms of allowed reachable velocities which means that the chance that there is no conflict resolution to be found is greater.

2) Hypothesis 2: The IPR is uncorrelated with wind: It is expected that the number of intrusions of the protected zone is constant for scenarios in which wind is implemented with respect to wind calm scenarios. This is because every vehicle involved in the scenario encounters the same amount of wind which makes no change in the body fixed reference system.

3) Hypothesis 3: The VPRG is negatively correlated with wind: It is expected that the number of violations of the geofence increases for increasing wind speeds. This is because the earth fixed turn radius of aerial vehicles increases positively with the strength of the tailwind component. This means, especially for small geofences, that there is a higher change to violate the geofence during an avoidance manoeuvre.

4) Hypothesis 4: The IPR is negatively correlated with respect to the distance to the geofence when a conflict has been detected: It is expected that the number of intrusions is the highest for a subset of conflicts that occur close the geofence as the space of allowed reachable velocities decreases close to a geofence as the size of a "virtual" velocity obstacle of a geofence segment is negatively correlated with respect to the distance to this geofence segment.

5) Hypothesis 5: The VPRG is negatively correlated with respect to the distance to the geofence when a conflict has been detected: It is expected that the number of geofence violations is highest for conflicts that occur close to a geofence. This is in the first place because the margin with respect to the geofence is smaller when already flying close the the geofence. Secondly, the chance is higher to violate a geofence when making a turn for which the turn radius is not taken into account in the conflict resolution method. The manoeuvring vehicle can therefore slightly violate the geofence during its conflict resolution manoeuvre.

D. General Set-Up

Table III gives an overview of the test series executed in simulation. The implementation of geofences and wind are varied over test series 1 to 4. Test series 0 and 5 are used in order to validate the scenarios executed in simulation to check whether geofences are violated when traffic is following its predefined route without enabling CD&R in wind calm and windy conditions respectively. A scenario is excluded from the experiment if a geofence is violated in the validation test series since these geofence violations are the cause of the scenario definition instead of the selected conflict resolution. A total of 10000 scenarios have been generated for which 9874 scenarios are valid. Test series 1 to 4 are executed in order to compare the IPR and VPRG performance parameters to test the hypotheses for this experiment.

V. Scenario generation

Scenarios for each test series are generated according to the steps given in figure 12. It can be seen that scenarios are

TABLE III
TEST SERIES RUNNED IN SIMULATION

Number	CD&R	Geofences	Wind
0	x	x	x
1	✓	x	x
2	✓	✓	x
3	✓	x	✓
4	✓	✓	✓
5	x	x	✓

generated in 5 steps which are discussed in more detail in this section. Depending on the test series, the following semi-random generators are implemented for scenario generation: traffic, conflict scenario, wind, route and geofence. Methods, parameters and randomisation which have been used for each generator is discussed in this section.

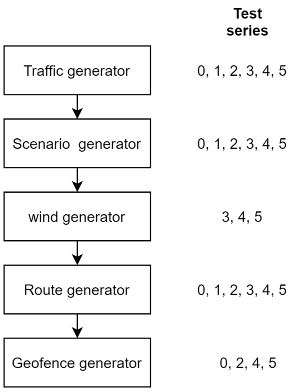

Fig. 12. Steps taken to generate a conflict scenario for each test series.

A. Traffic generator

Two aerial vehicles are generated for each scenario. Table IV gives the parameters, randomisation and ranges used to generate flight envelops for the traffic simulated in each scenario. Each vehicle involved in the scenario can be a fixed wing (FW) or rotorcraft (RC) type. The maximum and minimum speed for each vehicle is defined depending on the vehicle type. FW vehicles have a minimum speed which is δV_{FW} lower than its maximum speed. RC vehicles only have a maximum speed defined and are able to hover and fly backwards. Finally, a maximum bank angle is defined which has influence on the turn radius of the vehicle.

TABLE IV
PARAMETER RANGES AND RANDOMISATION FOR AIR VEHICLES

Parameter	Range	Randomisation	Unit
Number of vehicles, N_V	2	-	-
Vehicle type	(RC, FW)	uniform	-
Min initial speed RC, $V_{min_{initial}}$	5	-	[m/s]
Max speed RC, $V_{max_{RC}}$	(10, 20)	uniform	[m/s]
Min speed RC, $V_{min_{RC}}$	0	-	[m/s]
Max speed FW, $V_{max_{FW}}$	(15, 25)	uniform	[m/s]
Difference speed FW, δV_{FW}	(5, 10)	uniform	[m/s]
Max bank angle	30	-	[deg]

B. Conflict scenario generator

Table V gives the parameters, randomisation and ranges used for the generation of a guaranteed conflict between the two vehicles involved in each scenario. First of all, an initial track χ_v and speed that is within the flight envelop is assigned to the first vehicle in the scenario. Secondly, an initial speed is defined for the second vehicle. Then, a relative bearing d_ψ and distance to the CPA d_{CPA} for a conflict is assigned to the scenario. The track and initial location of the second vehicle in the scenario is defined by those two parameters and the time to Loss of Separation (LoS) T_{LoS}. The time to LoS is the time it takes until the protected zone is expected to be intruded during a conflict. The T_{LoS} parameter is set to 30 seconds such that it is slightly larger than the look-ahead time of 25 seconds which is set for the conflict resolution method. So, the first conflict in each scenario is detected after 5 seconds from the start of each scenario.

TABLE V
PARAMETER RANGES AND RANDOMISATION FOR CONFLICT SCENARIOS

Parameter	Range	Randomisation	Unit
Initial vehicle track, χ_v	(0, 2π)	uniform	[rad]
Time to LoS, T_{LoS}	30	-	[s]
Distance to CPA, d_{CPA}	(0, 50)	uniform	[m]
Relative conflict bearing, d_ψ	(0, 2π)	uniform	[rad]

C. Wind generator

Table VI gives the parameters, randomisation and ranges used in order to generate wind for the scenarios executed in test series 3, 4 and 5. The wind speed and wind direction are both uniformly distributed. However, the value of the windspeed in a scenario should be smaller than the minimum initial speeds of the vehicles generated for that scenario such that both vehicles can overcome full headwind in the worst case.

TABLE VI
PARAMETER RANGES AND RANDOMISATION FOR WIND

Parameter	Range	Randomisation	Unit
Wind speed, V_{wind}	(0, 20)	uniform	[m/s]
Wind direction, χ_{wind}	(0, 2π)	uniform	[rad]

D. Route generator

A route of an UAV consists of several waypoints connected by legs. Each waypoint should be overflown before the UAV can continue its way to the next waypoint.

Routes are generated in a semi-random way. Parameters, randomisation and ranges used to generate routes are given in table VII. A track χ_{leg} and a time for a leg T_{leg} are assigned to each leg in a route. The distance of the leg is the vehicle's speed times the leg time.

E. Geofence generator

A semi-random geofence is constructed by the geofence generator such that the geofence encloses the waypoints of

TABLE VII
PARAMETER RANGES AND RANDOMISATION FOR ROUTES

Parameter	Range	Randomisation	Unit
Track of leg, χ_{leg}	(0, 2π)	uniform	[rad]
Leg time, T_{leg}	(60, 120)	uniform	[s]

the routes flown by the vehicles in each scenario. The following three steps have been taken to generate a semi-random geofence around all waypoints:

1) Draw a convex hull through waypoints such that each waypoint is a corner point of the convex hull or is enclosed by the convex hull.
2) Add a margin to the convex hull which is equal to twice the turn radius of the vehicle with the largest turn radius.
3) Calculate corners of a semi-random geofence enclosing all waypoints with adequate margin.

1) Convex hull of waypoints: The first step to take to generate a geofence is to identify the waypoints that are corners of the convex hull. Figure 13 shows two routes by dotted lines and waypoints by circles. The convex hull is drawn by thick lines. The points that are corners of the hull are filled black.

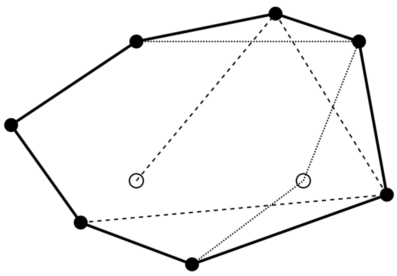

Fig. 13. A convex hull of a set of route waypoints

2) Adding margin to the convex hull: A margin should be added to the convex hull such that its vertices move outwards with two times the turn radius of the vehicle having the greatest turn radius in the scenario. This margin ensures that all vehicles involved in the scenario can make a full turn within the geofence. In this way, it can be guaranteed that every geofence violation is the result of a conflict resolution manoeuvre.

3) Calculate semi-random geofence corners: Table VIII gives the parameter and randomisation used to generate convex geofences around the waypoints of the vehicles involved in each scenario. A randomised margin R_{mar} is implemented at each corner of the geofence on top of the turn radius margin in order to make each geofence segment not perfectly parallel to the convex hull around the waypoints.

TABLE VIII
PARAMETER RANGES AND RANDOMISATION FOR GEOFENCES

Parameter	Range	Randomisation	Unit
Geofence margin, R_{mar}	(0, 50)	uniform	[m]

Figure 14 gives a graphical representation of the triangular shaded area in which a geofence corner can be placed for two adjacent hull elements. The angle at which the corner point is placed is uniformly randomised between χ_{min} and χ_{max}. The additional distance margin is also uniformly randomised according to the bounds given in table VIII.

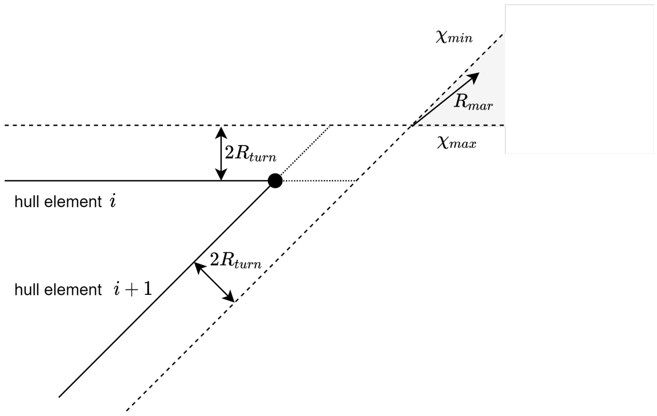

Fig. 14. Visual representation for the area in which a geofence corner point can be placed.

Connecting all calculated corner points of a geofence results in a convex geofence with adequate margin for turns at the waypoints. An example of a geofence drawn around waypoints is given by figure 15.

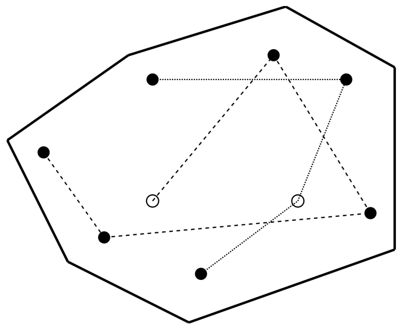

Fig. 15. Visual representation for the buffer zone used for route generation.

VI. RESULTS

This section presents the results of a series of experiments performed in four test-series. The experiments tested the intrusion prevention and geofence violation prevention capabilities of the applied CD&R algorithm.

The results are presented in the upcoming subsections on the basis of 5 relationships that have been tested for each rule-set. In the first place, the influence of geofences on the IPR has been tested. Then, the influence of the wind on the IPR and VPRG performance parameters is presented. Finally, the influence of the distance with respect to a geofence when a conflict has been detected on the IPR and VPRG performance parameters is discussed.

The type of influence that independent variables have on the dependent performance parameters can be tested using p-values calculated by the Wilcoxon signed-rank test [16]. Three types of Wilcoxon signed-rank tests can be performed on a set of data: two-sided, right-sided and left-sided. A p-value can be calculated for each type of test. The p-value gives the probability of getting results as extreme as the observed set of data assuming that the null hypothesis is true.

The null hypothesis of the two-sided Wilcoxon signed rank test is that the median of the difference between data pairs extracted from two sets of data is symmetrically distributed around zero. This means that the data-sets come from the same distribution. The alternative hypothesis of the two-sided test is that the median of the difference between data pairs extracted from two data-sets is not equal to zero. One-sided Wilcoxon signed rank tests can be performed when the null hypothesis of the two-sided test is rejected. It can be found out if the median of the difference between data pairs is greater or smaller than zero when performing a one-sided test. The null hypothesis of the right-sided test is that the median of the difference between data pairs is negative. The alternative hypothesis of this test is stating that the median of the difference between data pairs is positive. The null and alternative hypothesis for the left-sided test are defined the other way around.

The null-hypotheses are accepted or rejected according to the calculated p-values. It is assumed that a hypothesis can be accepted with significance if ($p < 0.05$). A Bonferroni correction of 5 needs to be applied to this significance level as five hypotheses are tested on the data-set. Therefore, the critical p-value p_{crit} is set to 0.01.

A. Influence of geofence implementation on the intrusion prevention rate

The first relationship that has been tested is how the number of intrusions is influenced by the introduction of geofences. Conflict data recorded for each experimental test series and conflict resolution strategy is randomly sampled in sets of each 100 conflicts. The IPR values are calculated over all of these sets of conflict data which is used for statistical analysis.

Figure 16 gives a Box and Whisker plot of the intrusion prevention rates for all experimental test scenarios with and without wind and geofences implemented. The data for each implemented resolution rule-set for each experimental test-series is visualised in the plot as box. It can be concluded from the plot that the OPT strategy is most optimal for every possible combination of wind and geofences implemented. Secondly, the HDG and DEST strategies perform about equally well in terms of intrusion prevention for wind calm scenarios. Finally, it can be concluded that the HDG strategy has most outliers below the median and performs worst in windy conditions.

A two-sided Wilcoxon signed rank test has been performed in order to find out if the IPR values for geofenced scenarios are uncorrelated with the IPR values generated for non-geofenced scenarios. The p-values that are generated by this test can be found in table IX. All p-values that are given in the table are greater than the critical p-value p_{crit} which means that the null hypothesis of this test cannot be rejected. The null hypothesis states that the IPR values generated for geofenced and non-geofenced scenarios are uncorrelated with each other. Therefore, the implementation of geofences does not significantly change the intrusion prevention performance of the applied conflict resolution method.

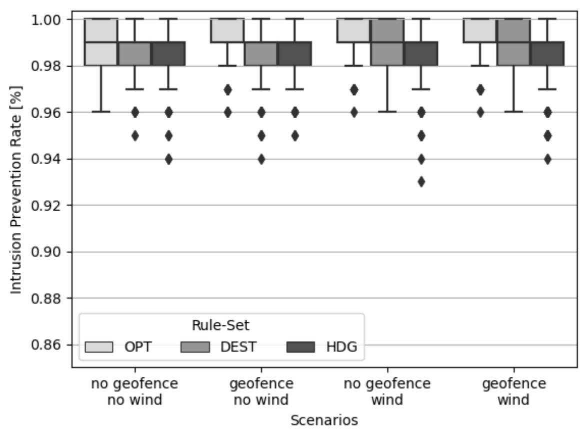

Fig. 16. Box and Whisker plot of IPR values for each rule-set for each experimental test-series.

TABLE IX
P-VALUES OF THE IPR FOR SAMPLES TAKEN FROM GEOFENCED SCENARIOS WITH RESPECT TO SAMPLES TAKEN FROM NON-GEOFENCED SCENARIOS GENERATED BY A TWO-SIDED WILCOXON SIGNED RANK TEST

	OPT	DEST	HDG
no wind	0.4336	0.8936	0.1047
wind	0.6611	0.9163	0.8088

B. Influence of wind on the performance parameters

This section presents the outcome of the analysis regarding the influence of wind on the intrusion prevention rate and violation prevention rate of the geofence respectively. The performance parameters are first compared on a macroscopic scale for which all conflict data generated by scenarios performed under windy conditions is compared with the data generated by scenarios performed under wind calm conditions. Secondly, an analysis on the performance parameters is presented on a microscopic scale. Conflict data generated by scenarios with simulated wind is subdivided into subsets categorised by wind speed for this microscopic analysis.

First of all, figure 16 can be used to show the effect that wind has on the intrusion prevention rate. It can be seen from the diagram that the experiments performed approximately irrespective of wind in terms of the intrusion prevention rate. It can be concluded that the IPR for each rule-set is uncorrelated with the presence of wind according to the p-values given in table X that are generated by a two-sided Wilcoxon signed rank test. It can be concluded that the IPR performance is not significantly different in windy conditions with respect to wind calm conditions because all p-values are greater than the critical p-value p_{crit}.

Secondly, the influence of wind on the number of geofence violations has been investigated. The conflict data is sampled in randomised sets of 100 conflicts and then used to

TABLE X
P-VALUES OF THE IPR FOR DATA SAMPLES GENERATED IN WINDY VERSUS WIND CALM SIMULATION ENVIRONMENTS GENERATED BY A TWO-SIDED WILCOXON SIGNED RANK TEST

	OPT	DEST	HDG
no geofence	0.6744	0.1980	0.2551
geofenced	0.5554	0.2358	0.2547

calculate the violation prevention rate of the geofence for each subset of data. The violation rates calculated for each subset are thereafter used for statistical analysis. Figure 17 gives a Box and Whisker plot given the VPRG values for each resolution rule-set for the scenarios in which geofences were implemented. It can be seen that there are slightly more violations of the geofence during experiments performed under windy conditions for the OPT rule-set. The HDG resolution strategy has slightly less violations of the geofence in windy conditions.

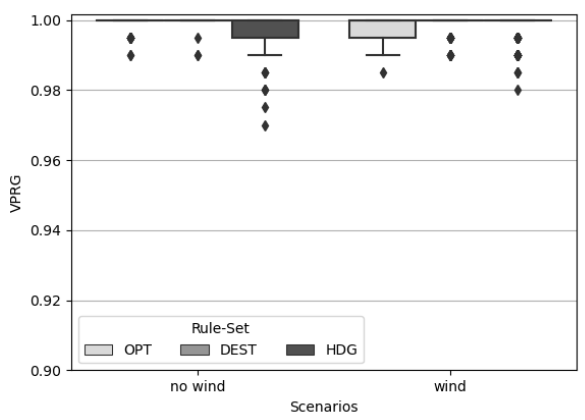

Fig. 17. Box and Whisker plot of VPRG values for each rule-set in geofenced scenarios.

A two-sided Wilcoxon signed rank test has been performed on the VPRG data recorded for windy versus wind calm data. The p-values generated by this test are given by table XI. It can be seen from the table that the p-values generated for each rule-set are smaller than the critical p-value p_{crit}. This means that the null hypothesis of this test needs to be rejected for all rule-sets. The null hypothesis of this test states that the VPRG values that are generated for conflicts under windy conditions do not come from the same distribution as the VPRG values generated for conflicts under wind calm conditions. Therefore, two one-sided Wilcoxon signed rank tests need to be performed to determine a possible relationship between wind and the number of violations of the geofence.

A left-sided Wilcoxon signed rank test on the VPRG values for windy versus wind calm scenarios is performed to check if a positive correlation of the VPRG with the implementation of wind can be rejected. Table XII gives the left-sided p-values generated by a Wilcoxon signed rank test. A positive correlation between the VPRG and the implementation of wind can be rejected for the OPT and DEST resolution strategy as the p-values corresponding to those resolution rule-sets are smaller than the critical p-value p_{crit}. Therefore, the alternative hypothesis stating that the VPRG is negatively correlated with wind can be accepted for the OPT and DEST rule-sets with significance. A positive correlation for the HDG resolution rule-set with wind cannot be rejected.

TABLE XI
P-VALUES OF THE VPRG FOR DATA SAMPLES GENERATED IN WINDY VERSUS WIND CALM SIMULATION ENVIRONMENTS BY A TWO-SIDED WILCOXON SIGNED RANK TEST

OPT	DEST	HDG
5.8314e-3	4.5492e-3	7.811e-4

TABLE XII
P-VALUES OF THE VPRG FOR DATA SAMPLES GENERATED IN WINDY VERSUS WIND CALM SIMULATION ENVIRONMENTS BY A LEFT-SIDED WILCOXON SIGNED RANK TEST

OPT	DEST	HDG
2.9157e-3	2.27462e-3	0.9996

A right-sided Wilcoxon signed rank test is performed to check whether a negative correlation of the VPRG values generated for windy versus wind calm conflicts can be rejected. The p-values generated by this test can be found in table XIII. It can be seen that the p-value for the HDG strategy is smaller than the critical p-value p_{crit} which means that a negative correlation of the VPRG values for the HDG resolution strategy can be rejected. Therefore, it can be concluded that the alternative hypothesis can be accepted for the HDG rule-set stating that the VPRG and implementation of wind is positively correlated.

TABLE XIII
P-VALUES OF THE VPRG FOR DATA SAMPLES GENERATED IN WINDY VERSUS WIND CALM SIMULATION ENVIRONMENTS BY A RIGHT-SIDED WILCOXON SIGNED RANK TEST

OPT	DEST	HDG
0.9971	0.9977	3.9059e-4

Next, a microscopic analysis is performed on the influence of wind on the intrusion and geofence violation prevention capabilities of the applied CD&R algorithm. Conflict data samples generated by scenarios performed under windy conditions are used and subdivided in three categories depending on the wind speed encountered during those conflicts. This categorised conflict data is randomly sampled in subsets of each 100 conflicts to calculate sets of intrusion and geofence violation prevention rates for each wind speed category. A no wind category is defined for which conflict data from scenarios without simulated wind has been used. The categories of wind speeds in which the data samples are subdivided are given by table XIV.

Two Box and Whisker plots giving the intrusion prevention rates for each resolution strategy for non-geofenced and geofenced scenarios are given by figures 18 and 19 respectively. The plots show that the intrusion prevention performance for all resolution strategies behave approximately independent

TABLE XIV
CATEGORISATION OF WIND SPEEDS

Wind speed category	Range
no	= 0 m/s
low	< 5 m/s
medium	(5 m/s, 10 m/s)
strong	> 10 m/s

of wind strength for non-geofenced and geofenced scenarios respectively.

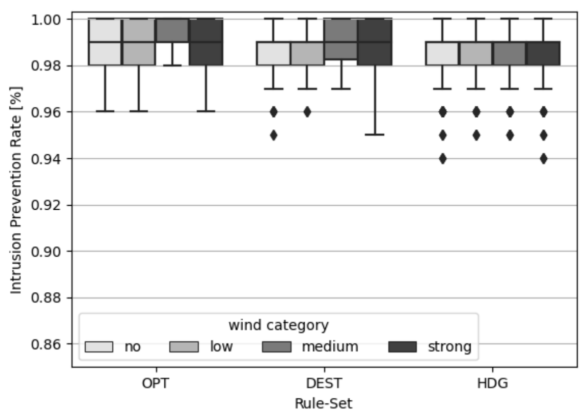

Fig. 18. Box and Whisker plot of the IPR for data samples generated by non-geofenced scenarios with wind implemented and categorised by wind strength.

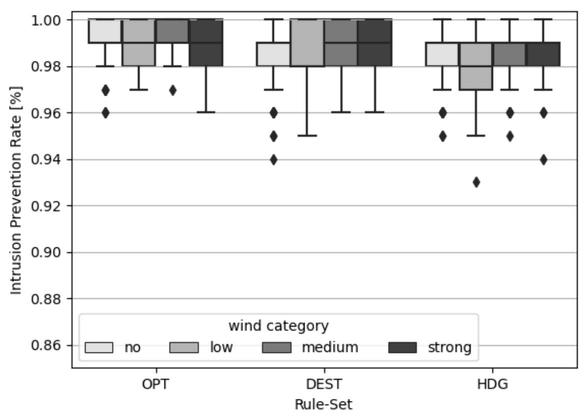

Fig. 19. Box and Whisker plot of the IPR for data samples generated by geofenced scenarios with wind implemented and categorised by wind strength.

The evidence that there is no clear correlation between wind strength and the number of intrusions is given by table XV giving the p-values of the two-sided Wilcoxon signed rank test for IPR data generated for each wind category versus the IPR data of scenarios without wind implemented. It can be seen in the table that no p-value is smaller than the critical p-value p_{crit} which means that the null hypothesis of this statistical test cannot be rejected for all rule-sets. The null hypothesis of this test states that the sets of data that are compared against each other come from the same distribution. This means that there is no correlation between the IPR data generated for each wind speed category and the IPR data for conflicts resolved in wind calm conditions.

TABLE XV
P-VALUES OF THE IPR FOR DATA SAMPLES GENERATED FOR EACH WIND CATEGORY VERSUS WIND CALM CONDITIONS GENERATED BY A TWO-SIDED WILCOXON SIGNED RANK TEST

	Wind category	OPT	DEST	HDG
non geofenced	low	0.3105	0.6580	0.5775
	medium	0.2052	0.1888	0.3436
	strong	0.4723	0.2346	0.2793
geofenced	low	0.2594	0.3961	0.0294
	medium	0.1385	0.0442	0.6822
	strong	0.5223	0.8111	0.0890

A Box and Whisker plot giving the violation prevention rate of the geofence for each rule-set and wind speed category is given by figure 20. The data samples used to generate this plot are taken from the simulated scenarios in which wind and geofences are implemented. It can be globally seen in the figure that the capabilities of preventing geofence violations decreases when the wind speed is increased for the OPT rule-set. In the first place, this behaviour is expected as wind can increase the turn radius of an air vehicle which increases the probability of violating a geofence when an avoidance manoeuvre is performed close to it. Secondly, if wind blows towards a geofence, the ground speed towards this geofence is increased which will result in a larger size of the "virtual" velocity obstacle generated for a geofence segment. The geofence violation prevention capability of the DEST strategy seems to be uncorrelated with wind speed. Finally, the value of the VPRG slightly decreases for increasing wind strength for the HDG resolution strategy.

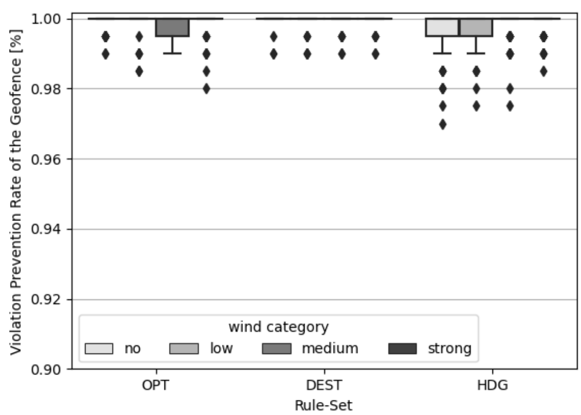

Fig. 20. Box and Whisker plot of the VPRG for data samples generated by geofenced scenarios with wind implemented and categorised by wind strength.

Table XVI gives p-values generated by a two-sided Wilcoxon signed rank test for the VPRG values recorded for each wind speed category versus the values recorded in scenarios without wind implementation. It can be seen that the p-value of the HDG resolution strategy with strong wind is lower than the critical p-value p_{crit}. This means that there is some correlation between wind strength and the geofence violation prevention performance for the HDG resolution strategy. The p-value generated by a right-sided Wilcoxon signed rank test of the VPRG for the HDG rule-set and strong wind is equal to 1.6516e-6 which is smaller than the critical p-value p_{crit}. This means that a negative correlation between the HDG rule-set and wind strength can be rejected. Therefore, it can be concluded with significance that the alternative hypothesis is true stating that there exist a positive correlation between the VPRG and wind strength for the HDG rule-set.

TABLE XVI
P-VALUES OF THE VPRG FOR DATA SAMPLES GENERATED FOR EACH WIND CATEGORY VERSUS WIND CALM CONDITIONS GENERATED BY A TWO SIDED WILCOXON SIGNED RANK TEST

Wind catgeory	OPT	DEST	HDG
low	0.9946	0.1742	0.7158
medium	4.8514e-2	2.2802e-2	3.7660e-2
strong	0.1871	0.1599	3.3031e-6

C. *Influence of distance with respect to geofence on performance parameters*

This section presents the effects of the distance with respect to the geofence on the intrusion and geofence violation prevention capabilities of the applied CD&R algorithm.

First of all, conflict data has been categorised in three groups regarding the distance with respect to the geofence at the start of the conflict. The no category encapsulates the data of all conflicts occurred in non-geofenced scenarios. The other 3 defined distance categories and their ranges can be found in table XVII.

TABLE XVII
CATEGORISATION OF DISTANCE WITH RESPECT TO THE GEOFENCE WHEN A CONFLICT ORIGINATES.

Distance category	Range
no	no geofence implementation
small	< 200 m
medium	(200 m, 400 m)
large	> 400 m

Figures 21 and 22 give Box and Whisker plots of the IPR values for each rule-set categorised by distance with respect to the geofence for wind calm and windy scenarios respectively. It can be seen from the plots that the intrusion prevention performance of all resolution strategies are positively correlated with the distance with respect to the geofence for small and medium distances. The positive correlations flattens out between the medium and large distances as can be seen in the plots.

A table with p-values generated by a two-sided Wilcoxon signed rank test on the IPR data samples for medium distances to the geofence versus small distances is given by table XVIII. It can be seen that all p-values in the table are indeed lower

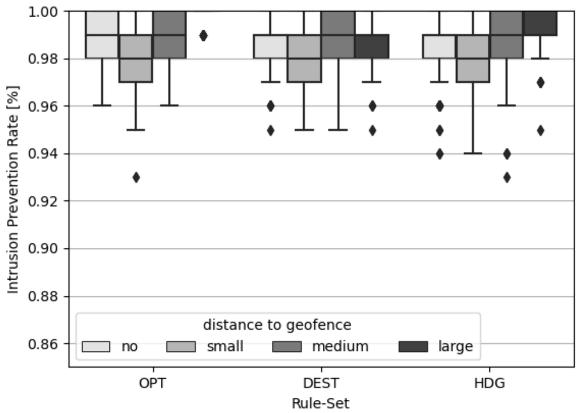

Fig. 21. Box Whisker plot of the IPR for data samples generated by geofenced scenarios without wind implemented and categorised by distance with respect to the geofence.

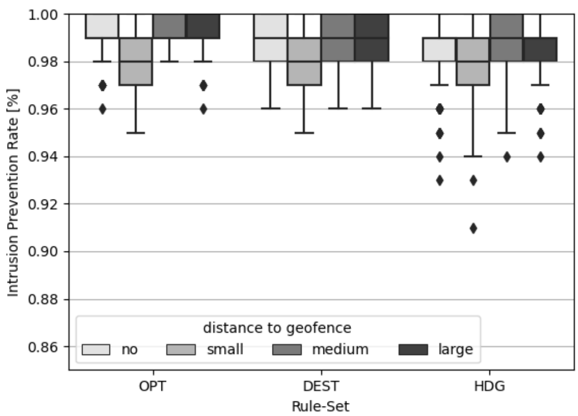

Fig. 22. Box Whisker plot of the IPR for data samples generated by geofenced scenarios with wind implemented and categorised by distance with respect to the geofence.

than the critical p-value p_{crit}. This means that it can be concluded with significance that the VPRG data comes from a different distribution and thus is somehow correlated with the distance to the geofence. Therefore, it can be assumed that there is some positive or negative correlation between the IPR values generated for conflicts at medium versus small distances with respect to the geofence.

TABLE XVIII
P-VALUES OF THE IPR FOR DATA SAMPLES GENERATED FOR MEDIUM DISTANCES TO THE GEOFENCE WITH RESPECT TO SMALL DISTANCES GENERATED BY A TWO-SIDED WILCOXON SIGNED RANK TEST

	OPT	DEST	HDG
no wind	2.3912e-3	5.0396e-3	4.4818e-11
wind	7.8925e-10	3.6332e-5	7.6248e-11

A right-sided Wilcoxon signed rank test is performed to find out if a negative correlation between the distance with respect to the geofence and the IPR values for medium versus small distances to the geofence can be rejected. The p-values generated by this test are given in table XIX. It can be seen in the table that all p-values are lower than the critical p-value p_{crit} which means that a negative correlation between the distance with respect to a geofence and the IPR value is rejected. Therefore, the alternative hypothesis stating that there is a positive correlation between the IPR and distance to the geofence can be accepted with significance.

TABLE XIX
P-VALUES OF THE IPR FOR DATA SAMPLES GENERATED FOR MEDIUM DISTANCES TO THE GEOFENCE WITH RESPECT TO SMALL DISTANCES GENERATED BY A RIGHT-SIDED WILCOXON SIGNED RANK TEST

	OPT	DEST	HDG
no wind	1.1961e-3	2.5198e-3	2.2409e-11
wind	3.9463e-10	1.8166e-5	3.8124e-11

Figures 23 and 24 give Box Whisker plots of the violation prevention rates of the geofence for each rule-set categorised by distance with respect to the geofence for wind calm and windy scenarios respectively. It can be seen that the chance of violating a geofence is the greatest when an UAV is involved in a conflict located close to a geofence. This is an expected result as the resolution space is smaller close to a geofence and it is more likely that an UAV crosses a geofence during a conflict resolution manoeuvre when it is already flying close to a geofence.

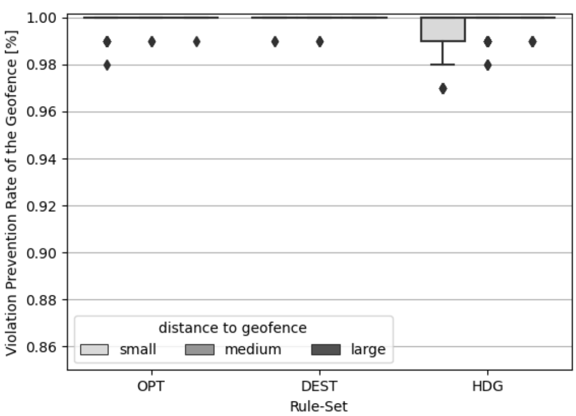

Fig. 23. Box Whisker plot of the VPRG for data samples generated by geofenced scenarios without wind implemented and categorised by distance with respect to the geofence.

A table with p-values generated by a two-sided Wilcoxon signed rank test on the VPRG data samples for large distances to the geofence versus small distances is given by table XX. It can be seen that the p-values of the DEST resolution strategy are not smaller than the critical p-value p_{crit}. This means that the VPRG data for the DEST strategy shows no clear correlation with the distance to the geofence. The other two resolution strategies show a correlation as their p-values are smaller than the critical p-value.

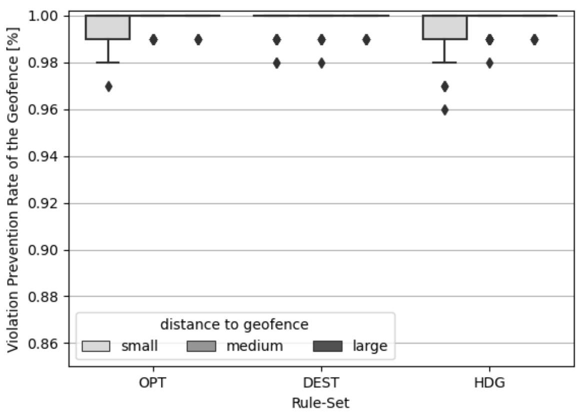

Fig. 24. Box Whisker plot of the VPRG for data samples generated by geofenced scenarios with wind implemented and categorised by distance with respect to the geofence.

TABLE XX
P-VALUES OF THE VPRG FOR DATA SAMPLES GENERATED FOR LARGE DISTANCES TO THE GEOFENCE WITH RESPECT TO SMALL DISTANCES GENERATED BY A TWO-SIDED WILCOXON SIGNED RANK TEST

	OPT	DEST	HDG
no wind	8.0519e-3	0.5995	7.0312e-10
wind	2.3545e-5	6.0171e-2	2.0623e-10

A right-sided Wilcoxon signed rank test is performed to check if a negative correlation between the distance to the geofence and the VPRG for large versus small distances to the goefence can be rejected. The p-values generated by this test are given in table XIX. It can be seen in the table that the p-values for the OPT and HDG rule-sets are lower than the critical p-value p_{crit} which means that a negative correlation between the distance with respect to the geofence and the VPRG value is rejected for these rule-sets. Therefore, the alternative hypothesis stating that there is a positive correlation between the VPRG and the distance to the geofence can be accepted with significance for the OPT and HDG rule-sets.

TABLE XXI
P-VALUES OF THE VPRG FOR DATA SAMPLES GENERATED FOR LARGE DISTANCES TO THE GEOFENCE WITH RESPECT TO SMALL DISTANCES GENERATED BY A RIGHT-SIDED WILCOXON SIGNED RANK TEST

	OPT	DEST	HDG
no wind	4.0260e-3	0.2998	3.5156e-10
wind	1.773e-5	6.0171e-2	2.0623e-10

VII. DISCUSSION

The main question that is to be answered by this research is how the implemented conflict resolution method performs in terms of intrusion prevention and geofence violations prevention under a variety of geofence geometries and wind conditions. This discussion will elaborate on the 5 hypotheses that have been stated for this research.

A. Hypothesis 1: The IPR is negatively correlated with the implementation of geofences

It was expected from the first hypothesis that the intrusion prevention of the CD&R algorithm would be negatively influenced by the implementation of geofences. However, according to the data visualised in the Box and Whisker plot given by figure 16 it can be barely concluded that the IPR data-sets generated by geofenced scenarios perform worse than for non-geofenced scenarios. This conclusions is supported by table IX which gives p-values generated by a two-sided Wilcoxon signed rank test. The input data for the p-value generation is taken from the data samples generated in non-geofenced and geofenced scenarios for each resolution strategy. All p-values are greater than the critical value p_{crit} which means that it cannot be concluded that the implementation of geofences negatively affect the intrusion prevention rate. So, the first hypothesis stating that the implementation of geofences would negatively influence the intrusion prevention rate is rejected for all resolution strategies.

It was expected that the number of intrusions would increase due to the implementation of geofences. This was expected because the "virtual" velocity obstacles generated for geofences would reduce the resolution space. However, the experimental results of this research did not support this expectation. Apparently, the influence of the geofence on the intrusion prevention rate was not observable for the full set of conflict data on which the hypothesis was tested. However, it seems like that there is a noticeable effect for conflicts at only small distance with respect to the geofence by comparing IPR values for non-geofenced scenarios with the values generated for conflicts at small distance with respect to the geofence as given by figures 21 and 22 for wind calm and windy scenarios respectively. The p-values generated by a two-sided Wilcoxon signed rank test for the IPR values recorded in scenarios without a geofence versus the IPR values for conflicts recorded in geofenced scenarios that have a small distance to the geofence are given by table XXII for wind calm and windy conditions. It can be seen that the p-values for the OPT and HDG rule-set are smaller than the critical p-value p_{crit}. This means that there is some correlation for these rule-sets.

TABLE XXII
P-VALUES GENERATED BY A TWO SIDED WILCOXON SIGNED RANK TEST OF THE IPR VALUES FOR SAMPLES TAKEN FROM CONFLICTS WITH SMALL DISTANCE TO THE GEOFENCE WITH RESPECT TO SAMPLES TAKEN FROM NON-GEOFENCED SCENARIOS

	OPT	DEST	HDG
no wind	3.4257e-4	2.7396-2	4.090e-3
wind	2.1602e-6	5.3620e-2	9.1578e-8

A left-sided Wilcoxon signed rank test has been performed in order to reject a positive correlation between the IPR for conflict data recorded in scenarios without geofence and conflicts that occurred at small distance to the geofence. The p-values generated by this test are given by table XXIII. It can be seen that the p-values of the OPT and HDG rule-sets are smaller than the critical p-value p_{crit}. This means that the hypothesis stating that the IPR and the presence of a geofence at small distance affects the intrusion prevention performance in a negative way can be accepted with significance. It is also expected that an increase in the number of vehicles flying inside the geofence can increase the effect of the goefence on the IPR performance because an increase in vehicles will decrease the manoeuvring space to resolve a conflict.

TABLE XXIII
P-VALUES OF THE IPR VALUES FOR BY A LEFT-SIDED WILCOXON SIGNED RANK TEST SAMPLES TAKEN FROM CONFLICTS WITH SMALL DISTANCE WITH RESPECT TO THE GEOFENCE WITH RESPECT TO SAMPLES TAKEN FROM NON-GEOFENCED SCENARIOS

	OPT	DEST	HDG
no wind	1.7129e-4	1.3698-2	2.0450e-3
wind	1.0801e-6	2.6810e-2	4.5789e-8

B. Hypothesis 2: The IPR is uncorrelated with wind

The intrusion prevention rate was expected to be uncorrelated with wind according to hypothesis 2. This hypothesis can be accepted for all resolution strategies according to the results presented in section VI.

C. Hypothesis 3: The violation prevention rate of the geofence is negatively correlated with wind strength for the HDG rule-set

Hypothesis 3 states that the violation prevention rate of the geofence is negatively correlated with the implementation of wind. However, this hypothesis cannot be accepted for all rule-sets according to the data presented in the results section. There is a positive correlation detected between the VPRG and wind strength for the HDG resolution strategy. This unexpected behaviour is further discussed.

The explanation of the positive correlation between the VPRG and wind strength for the HDG rule-set may be found in the equation given the violation prevention rate of the geofence as given by equation 15. The VPRG is the fraction of conflicts which have been resolved without geofence violations. So, two parameters play a roll in the determination of the violation prevention rate of the geofence: the number of conflicts and the number of geofence violations.

It was observed from the conflict data generated by each test-series that the number of conflicts for the HDG strategy increases by approximately 39% when wind is implemented with respect to scenarios without wind implemented. The increase of the number of conflicts for the OPT and DEST resolution strategies are equal to approximately 13% and 15% respectively. The number of conflicts increases faster for the HDG rule-set than for the OPT and DEST strategies. This increase in number of conflicts for the HDG strategy may lead to a decrease in geofence violation rate if those extra conflicts in windy conditions does not cause geofence violations.

The nature of those extra conflicts that occur in windy conditions for the HDG rule-sets originate from conflicts of crossing traffic at shallow angles flying at approximately the same velocity. The HDG rule-set resolves the initial conflict only by the smallest change in direction. After the conflict has been resolved, both vehicles resume their routes towards their targets inducing a new shallow angle conflicts with each other which is to be resolved next. This repeating behaviour can persist until a waypoint of one of the conflicting vehicles has been reached. The OPT and DEST rule-sets are less susceptible to this repeating behaviour as it often directly resolves conflicts without inducing new conflicts afterwards. In the first place, the accumulation of short timed conflicts for the HDG rule-set does increase the total number of conflicts whereas almost never a geofence is violated as the duration of these conflicts is short. Secondly, a strong headwind strengthens this effect as it takes longer for an UAV to reach a waypoint, which will induce more short conflicts on the leg. Therefore, the effect is the greatest for strong wind strength.

So the increase in violation prevention rate of the geofence is partly caused by an increasing number of short term conflicts with increasing wind strength for the HDG rule-set. At the other side, looking at the number of simulated scenarios in which a violation of the geofence has been detected is lower for windy conditions than for wind calm conditions for the HDG resolution strategy as can be seen in table XXIV. So the chance that a geofence is violated for a scenario with wind implemented is smaller than for a scenario with no wind implementation when the HDG rule-set is used. This effect is mainly caused for scenarios with a parallel conflict with headwind directed towards a geofence segment. The time to resolve a repeating conflict increases due to the headwind which means that some conflict can be successfully resolved before passing a geofence segment in windy conditions in contrast to scenarios without wind implemented.

TABLE XXIV
NUMBER OF SCENARIOS IN WHICH A VIOLATION OF THE GEOFENCE IS DETECTED OUT OF 9874 SCENARIOS

	OPT	DEST	HDG
no wind	13	3	115
wind	40	26	81

All in all, the positive correlation of the violation prevention rate of the geofence and wind strength of the HDG rule-set is in the first place caused by an increase of short timed shallow angle conflicts. The second cause is that the number of scenarios for which a violation of the geofence has been detected is lower for the test-series in which wind is implemented.

D. Hypotheses 4 and 5: The IPR and VPRG are negatively correlated with respect to the distance to the geofence when a conflict has been detected

According to hypotheses 4 and 5, it is expected that the the number of intrusions and goefence violations is larger for conflicts that occur close to the geofence with respect to conflicts occurring at larger distance from a geofence. Hypotheses 4 stating that the IPR is negatively correlated with the distance with respect to the geofence is accepted for all rule-sets according to the data between the small and medium distances to the geofence as presented in the results section.

Hypothesis 5 stating that the VPRG decreases for increasing distance to the geofence is accepted for the OPT and HDG rule-sets. No clear correlation has been found for the DEST rule-set. This can be explained by the fact that the DEST rule-set always selects a conflict resolution towards its target waypoint. This waypoint is always located within the geofence which results in conflict resolution manoeuvres directed inside the geofence. Therefore, the chance of violating a geofence segment is smaller for the DEST rule-set with respect to other rule-sets. This is also true for conflicts occurring close to the geofence.

VIII. CONCLUSIONS AND RECOMMENDATIONS

This research investigated the safety effects on a velocity obstacle based conflict resolution method within a horizontally restricted airspace by a geofence. The velocity obstacle based conflict resolution method has been extended with ”virtual” velocity obstacles for each conflicting intruder and geofence segment. The parameters that represent the level of safety that have been measured throughout this research are the Intrusion Prevention Rate (IPR) and Violation Prevention Rate of the Geofence (VPRG). Those safety parameters have been assessed for three implemented coordination rule-sets: (1) the geometric optimum solution (OPT), (2) geometric optimum from target heading (DEST) and (3) only change in heading (HDG).

The results show that the OPT rule-set performed best in terms of the intrusion prevention rate. At the other side, the DEST rule-set performs best in terms of violation prevention rate of the geofence. It can be concluded from the results that the intrusion and geofence violation prevention performance is negatively correlated with the distance with respect to the geofence. Both the number of intrusions and geofence violations was the highest for all-rule sets at small distances ($<$200m) with respect to the geofence. The wind also influences the safety parameters in a negative sense close to geofences. Therefore, more research is proposed on scenarios with narrow geofences in order to improve safety for conflicts occurring close to geofences.

Recommended for future research is to measure the effects of geofences for conflict resolutions generated for multi-aircraft conflicts. It is also recommended to perform real flight tests with scenarios that have been simulated during this research. The method of constructing ”virtual” velocity obstacles for geofence segments can also be adapted in the future to be able to construct velocity obstacles for concave geofences. Another aspect to look into is to incorporate the vehicle dynamics in the selection of a conflict resolution. Vehicle dynamics have not been implemented in the method which causes some minor geofence violations when a recovery point is placed close to a geofence. There is not enough space for the vehicle to turn back to its target without violating the geofence during such manoeuvres. Lastly, it is concluded that the safety parameters are the worst for conflicts occurring close to the geofence under windy conditions. Therefore, it would be recommended to perform more research on vertical conflict resolution methods which may be beneficial within narrow airspaces such as corridors.

References

[1] B. Syd Ali, "Traffic management for drones flying in the city," *International Journal of Critical Infrastructure Protection*, vol. 26, p. 100310, 2019.

[2] P. Kopardekar, J. Rios, T. Prevot, M. Johnson, J. Jung, and J. E. Robinson, "Unmanned aircraft system traffic management (UTM) concept of operations," *16th AIAA Aviation Technology, Integration, and Operations Conference*, pp. 1–16, 2016.

[3] T. Jiang, J. Geller, D. Ni, and J. Collura, "Unmanned Aircraft System traffic management: Concept of operation and system architecture," *International Journal of Transportation Science and Technology*, vol. 5, no. 3, pp. 123–135, 2016. [Online]. Available: http://dx.doi.org/10.1016/j.ijtst.2017.01.004

[4] J. Ellerbroek, K. C. R. Brantegem, M. M. Rene Van Paassen, N. De Gelder, and M. Mulder, "Experimental evaluation of a coplanar airborne separation display," *IEEE Transactions on Human-Machine Systems*, vol. 43, no. 3, pp. 290–301, 2013.

[5] G. A. Mercado Velasco, C. Borst, J. Ellerbroek, M. M. Van Paassen, and M. Mulder, "The Use of Intent Information in Conflict Detection and Resolution Models Based on Dynamic Velocity Obstacles," *IEEE Transactions on Intelligent Transportation Systems*, vol. 16, no. 4, pp. 2297–2302, 2015.

[6] C. Borst, V. A. Bijsterbosch, M. M. van Paassen, and M. Mulder, "Ecological interface design: supporting fault diagnosis of automated advice in a supervisory air traffic control task," *Cognition, Technology and Work*, vol. 19, no. 4, pp. 545–560, 2017.

[7] Y. I. Jenie, E. J. Van Kampen, C. C. De Visser, J. Ellerbroek, and J. M. Hoekstra, "Selective velocity obstacle method for deconflicting maneuvers applied to unmanned aerial vehicles," *Journal of Guidance, Control, and Dynamics*, vol. 38, no. 6, pp. 1140–1145, 2015.

[8] Y. I. Jenie, E. J. Van Kampen, J. Ellerbroek, and J. M. Hoekstra, "Safety assessment of a UAV CDR system in high density airspace using monte carlo simulations," *IEEE Transactions on Intelligent Transportation Systems*, vol. 19, no. 8, pp. 2686–2695, 2018.

[9] A. Chakravarthy and D. Ghose, "Obstacle avoidance in a dynamic environment: A collision cone approach," *IEEE Transactions on Systems, Man, and Cybernetics Part A:Systems and Humans.*, vol. 28, no. 5, pp. 562–574, 1998.

[10] P. Fiorini and Z. Shiller, "Motion planning in dynamic environments using velocity obstacles," *International Journal of Robotics Research*, vol. 17, no. 7, pp. 760–772, 1998.

[11] J. Ellerbroek, "Airborne Conflict Resolution in Three Dimensions," PhD Thesis, Delft University of Technology, 2013.

[12] J. M. Hoekstra, R. N. Van Gent, and R. C. Ruigrok, "Designing for safety: The 'free flight' air traffic management concept," *Reliability Engineering and System Safety*, vol. 75, no. 2, pp. 215–232, 2002.

[13] S. Balasooriyan, "Multi-aircraft Conflict Resolution using Velocity Obstacles," Master Thesis, Delt University of Technology, 2017.

[14] J. M. Hoekstra and J. Ellerbroek, "BlueSky ATC Simulator Project: an Open Data and Open Source Approach," in *Proceedings of the seventh International Conference for Research on Air Transport (ICRAT)*, no. June, 2016. [Online]. Available: https://www.researchgate.net/publication/304490055

[15] J. Sun, J. M. Hoekstra, and J. Ellerbroek, "OpenAP: An open-source aircraft performance model for air transportation studies and simulations," *Aerospace*, vol. 7, no. 8, 2020.

[16] F. Wilcoxon, "Individual comparisons of grouped data by ranking methods." *Journal of economic entomology*, vol. 39, no. 6, p. 269, 1946.

II

Preliminary Thesis [Already Graded]

1 Introduction

Today, a huge number of users demand services from the Air Traffic Management (ATM) system that makes safe air operations possible. In the past decade, a lot of developments have been made regarding Unmanned Aerial Vehicles (UAVs) or better known as drones. In order to keep safe aeronautical operations possible, a similar system like ATM needs to be designed and implemented for drones. The system that manages the drones within controlled airspace is named the UAV Traffic Management (UTM) system, and is currently in test and development phase by academia and industry [14]. There is need for extensive research within the new UTM system as the ATM system cannot simply be replicated for drones as this system is focused on pilots navigating from inside the aircraft instead of drone operators flying their drones semi-autonomous from their ground based control station. Furthermore, according to Jiang [9], the key differences between drone operations and manned air operations are the control, manoeuvrability, functional range and constraints regarding operations. An important part of the ATM system are Conflict Detection and Resolution (CD&R) approaches in order to keep separation between airspace users at an acceptable level of safety. The challenges of applying such CD&R approaches on UAVs emerge from the different missions, constraints and configurations compared to manned aviation. Whereas manned air vehicles fly from origin to destination, an UAV can perform survey missions. Another challenge is to find a conflict resolution within an airspace constrained by a geofence which may not be crossed by the UAV. Finally, UAVs come in a variety of configurations such as rotorcraft, fixed wings and hybrids for which existing CD&R methods need to be reviewed en re-tuned.

The goal of this research is to contribute to a robust CD&R algorithm that can be used on UAVs. The goal will be reached by adapting velocity obstacle based CD&R methods developed for ATM, taking into account geofence constraints and the influence of wind on the UAV's flight dynamics. As a result of the research, recommendations will be made on the implementation and future research of a CD&R algorithm including geofence protection. The results can be valuable for the body of knowledge as the influence of geofence constraints on a CD&R algorithm have never been studied before. Furthermore, a reliable CD&R system should be operational in the near future as part of UTM.

The research described in this report will make use of a velocity obstacle based CD&R method. The master thesis of Balasooriyan [1] is used as main input for the development of this method. Balasorooriyan did research on autonomous conflict resolution strategies based on a Solution Space Diagram (SSD). The SSD will be extended with geofences as velocity obstacles for usage on UAVs. Several rule-sets for conflict resolution have been tested by Balasooriyan [1] and will be re-evaluated for UAVs with geofences implemented. A new rule-set will be developed to strive for better performance for UAV missions within geofenced airspaces. This research will not focus on multi aircraft conflict situations, but only on single conflict pairs. Furthermore, only horizontal conflict resolutions will be assessed during the experiments to be done for this research.

Section 1.1 of this introduction gives the research objective, research framework, research questions and research activities. Finally, the outline of this report is discussed in section 1.2.

1.1. Research Objective and Research Questions

This section describes the research objective, research framework, research questions and research activities to be performed for this research.

The research objective for this research is defined as follows:

The research objective is to contribute to a robust CD&R algorithm to be used on UAVs, regarding how to adapt existing CD&R techniques in order to provide an implicitly coordinated tactical CD&R approach, taking into account the limitations of geofences combined with wind by defining a set of avoidance rules to be assessed by simulations and flight tests implementing adaptations of existing implicitly coordinated tactical CD&R algorithms developed for manned aviation.

A research framework has been developed in order to reach the research objective. The research framework is given by figure 1.1. The research framework assists in shaping the research project in order to reach the research objective.

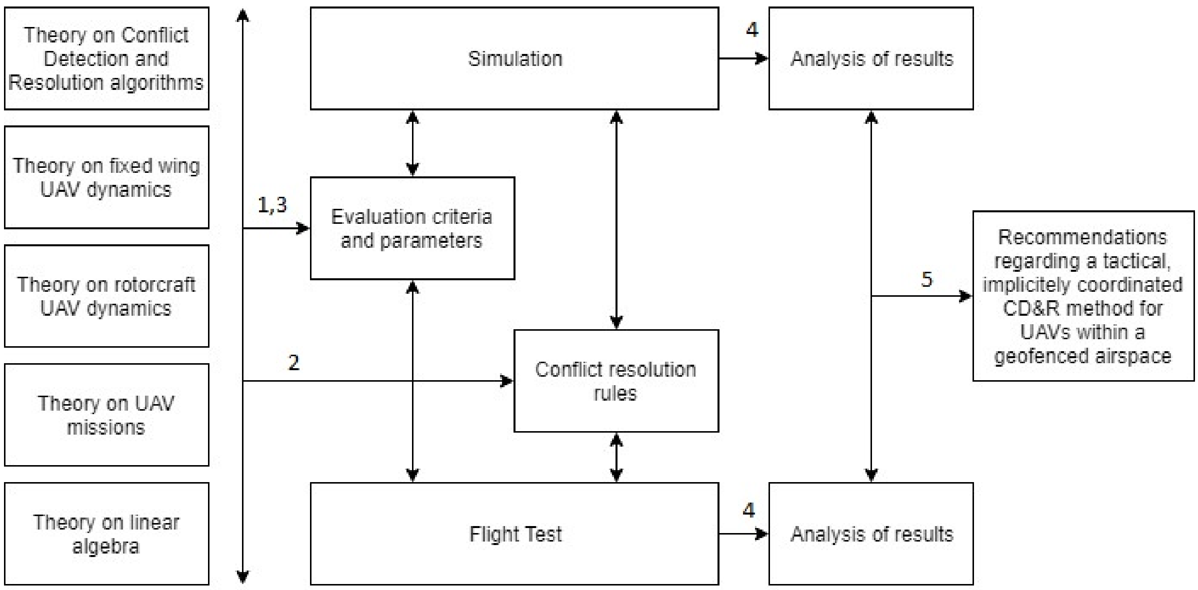

Figure 1.1: Research Framework

Each horizontal arrow in the research framework represents one or multiple research questions that need to be answered throughout the research. Numbers above the horizontal arrows correspond to a research question number that are listed below:

1. What criteria are relevant for assessing the performance of a CD&R algorithm?
2. What CD&R algorithms are suitable to be adapted and implemented on UAVs?
3. What values need to be assigned to the constant parameters implemented in the CD&R algorithm?
    (a) What is the value that needs to be assigned to the lookahead time in order to have adequate time for a tactical avoidance manoeuvre?
    (b) What are the range of values to be assigned to simulated drone models to have an adequate representation of drones flying today?
4. What is the performance of the CD&R algorithm with different sets of avoidance rules considering the set of assessment criteria?
5. What do we learn by comparing the results from the simulations and tests of the CD&R algorithms in order to make recommendations on how to develop a tactical, implicit coordinated CD&R algorithm for UAVs?

A list of seven research activities have been set-up that will assist in answering the research questions by the end of this research project. The research activities are indicated below.

Research Activity 1. Literature Review

A literature review will be performed in order to answer research questions 1, 2 and 3. Possible candidates of existing velocity based CD&R strategies as well as assessment criteria for those algorithms will be derived from literature. Also the parameters for the CD&R algorithm as well as parameters to be used for UAV simulation models will be extracted from literature.

Research Activity 2. Define CD&R algorithm

This research activity will help to answer research question 2. An existing CD&R method will be selected during this activity to be extended with a geofence protection in a later stage.

Research Activity 3. Extend CD&R algorithm with wind and geofences implemented

The selected CD&R algorithm will be extended with a geofence protection in order to be able to test the influence of the geofences on the performance of the implemented algorithm. The CD&R algorithm will also be adapted for wind during this stage of research.

Research Activity 4. Programming simulation

A simulation will be programmed in order to generate data regarding the performance of a CD&R algorithm running on an UAV with geofences and wind implemented. This data is needed as input for research question 4 which covers the analysis of results generated during a set of simulations.

Research Activity 5. Program software for flight test

Software to run on a real UAV will be programmed in order to validate a simulated test scenario with a real life scenario in order to be able to answer research questions 4 and 5.

Research Activity 6. Analysis results

Analysis will be performed on the test data set coming from the simulations and flight test. Those results will be visualised in plots and given by tables.

Research Activity 7. Evaluate performance

The performance of the CD&R algorithm can be evaluated from the analysis of results. Performance of the CD&R algorithm will be expressed in probabilities that the horizontal protected zone around an UAV is penetrated by an intruder as well as the probability that during an avoidance manoeuvre the geofence is violated.

1.2. Outline

The goal of this report is to give the results of the preliminary phase of this research. The report is structured as follows:

Chapter 2 describes the architecture of a CD&R system and identifies the scope of this research within this architecture. Chapter 3 describes the velocity obstacle based CD&R algorithms that will be implemented, adapted and re-tuned for this research. Chapter 4 describes the extension of the algorithm regarding the implementation of a geofence as velocity obstacles. Chapter 5 gives a description of the algorithm parameters, experiments to be performed and the expected form of the experimental results. Finally, chapter 6 concludes this report.

2

CD&R Architectures

A CD&R architecture is discussed in this section that gives an overview of different CD&R approaches for UAVs. This architecture can be used in order to identify possible approaches to take during the research discussed in this report. An overview of a CD&R architecture proposed for UAVs is discussed in section 2.1. Finally, the scope of this research that focuses on the cooperative layer of safety of the CD&R architecture is discussed in section 2.2. The role of UTM within the cooperative layer of safety is discussed in this section as well.

2.1. Multilayered Architecture

A multilayered CD&R architecture is already in place for manned aviation [7] as shown by figure 2.1. The figure shows six "layers of safety" ranging from procedural avoidance by scheduling flights to "see and avoid" manoeuvres based on the estimated time to a collision. This indicates that different CD&R approaches have been developed for different types of encounters depending on the time to Loss of Separation (LoS).

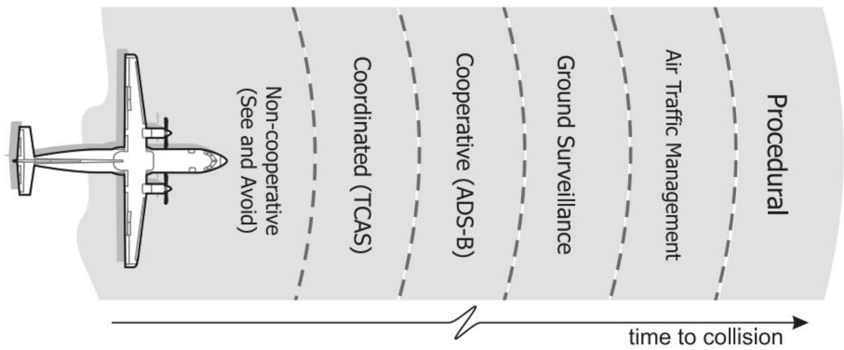

Figure 2.1: Multilayered CD&R architecture implemented for manned flight. Adapted from [7].

It is vital for safety that a multilayered CD&R architecture is to be identified for UAVs such that a fail safe CD&R system can be investigated and developed. Jenie [7] proposes in his paper a CD&R taxonomy for UAVs based on the type of surveillance, coordination, manoeuvres and autonomy. Each layer of safety in the CD&R taxonomy can be seen as a combination of those four factors. Each of those factors will be elaborated on next.

Surveillance The following three types of surveillance have been identified by Jenie [7] that are used in aviation:

1. Centralised-dependent surveillance
2. Distributed-dependent surveillance
3. Independent surveillance

Centralised-dependent surveillance includes systems that retrieve information from a common station or a network of stations. This type of surveillance is included in the first three layers of safety in manned aviation as given by figure 2.1. However, systems like radar can not be used to detect UAVs as those vehicles are limited in size and lack metal parts in the construction.

Distributed-dependent surveillance means that surveillance data is received from the air vehicles that are involved in the system. This means that each vehicle cooperatively broadcast its flight state data.

Finally, independent surveillance means that all vehicles obtain data of intruders using on-board sensor systems. This can be compared with the "see and avoid" procedure performed in general aviation. For UAVs, this type of surveillance includes for example computer vision in order to detect other traffic.

Coordination The following three types of coordination have been identified by Jenie [7] which will be explained in more detail.

1. Explicitly coordinated avoidance
2. Implicitly coordinated avoidance
3. Uncoordinated avoidance

Explicitly coordinated avoidance is applied if all involved vehicles have an explicit coordination link with each other. Vehicles coordinate their avoidance manoeuvres by confirming resolution advisories between pairs of aircraft having a conflict. An example of an explicitly coordinated collision avoidance system is TCAS being used in manned aviation.

Implicitly coordinated avoidance is used when each vehicle involved in a conflict performs an avoidance manoeuvre according to a common set of rules without coordinating the resolution advisory with other traffic. A form of implicitely coordinated avoidance are the "rules of the air".

Uncoordinated avoidance is used when each vehicle decides on a resolution itself without communicating the resolution advisory or using a common algorithm to generate the resolution. This type of coordination has not been implemented in manned aviation due to the high level of complexity and risk involved with this coordination type. However this method may be implemented for drones performing a aggressive escape-manoeuvre as last resort.

Types of Avoidance Manoeuvre Three types of avoidance manoeuvres that can be performed have been identified by Jenie [7] and are further discussed next.

1. Strategic manoeuvre
2. Tactical manoeuvre
3. Escape manoeuvre

Strategic manoeuvres are made as long-range actions which change the initially flight path significantly. Strategic manoeuvres are computed in the planning phase of a flight. Several waypoints in terms of horizontal and vertical location are added or altered in order to perform a strategic manoeuvre.

Tactical manoeuvres are performed as a mid-range actions that influences a small part of the initial flight path. The manoeuvre aims to make a deviation from the initial flight path as small as possible, but making sure that separation thresholds are met.

Escape manoeuvres are performed as last resort in order to bring the ownship to safety. Those manoeuvres are being performed according to the "see and avoid" principle in manned aviation and based on sensor inputs when performed by UAVs.

Types of Autonomy Two types of autonomy have been identified by Jenie [7] and explained in more detail.

1. Manual
2. Autonomous

Manual avoidance is performed when a human operator makes the final decision regarding the avoidance resolution. A resolution advisory that needs to be confirmed by an UAV operator can be classified as manual.

Autonomous avoidance is performed when a conflict resolution is being calculated on-board and directly executed by the vehicle itself. Those type of manoeuvres are beneficial to be executed on drones flying Beyond Visual Line Of Sight (BVLOS) as the drone operator has limited situational awareness. Research has to be focused on this type of avoidance to be developed for UAVs.

Jenie [7] presented at the end of his paper a proposed taxonomy for UAVs as multilayered architecture based on the feasibility of the combinations of types of surveillance, coordination, manoeuvres and autonomy. Each layer can be seen as a generic CD&R approach combining those factors. The proposed CD&R architecture for UAVs compared to manned aviation is shown by figure 2.2.

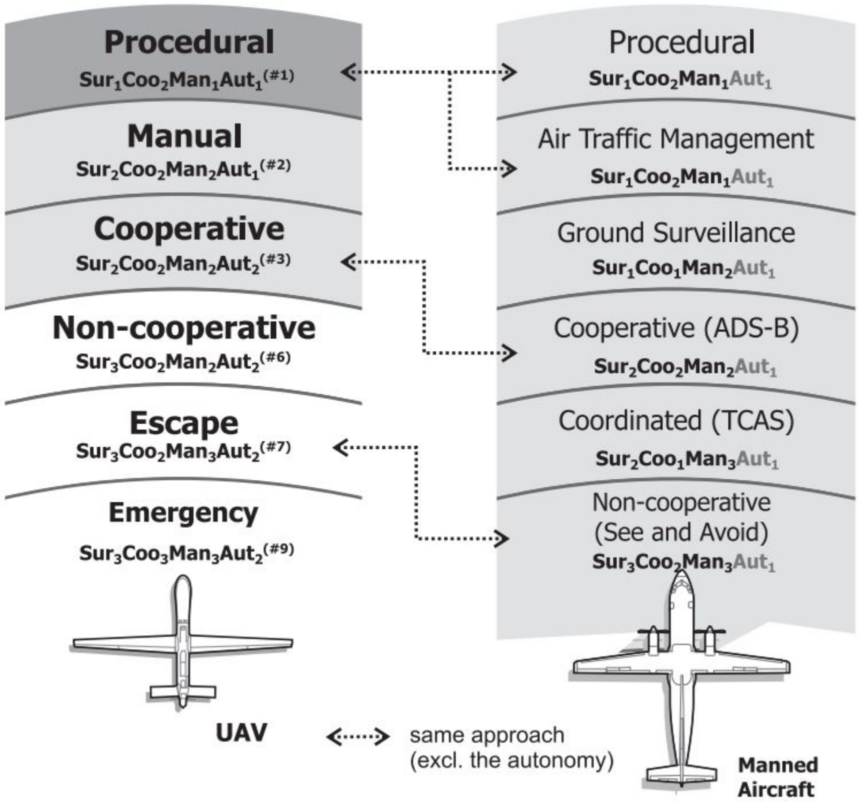

Figure 2.2: Multilayered CD&R architecture for UAVs compared to manned flight. Adapted from [7].

The proposed CD&R architecture for UAVs [7] consists of 6 safety layers that are slightly different from the layers implemented in manned aviation. This research focuses on a tactical implicit coordinated CD&R algorithm for UAVs. Therefore, the cooperative safety layer will be further investigated for this research. The next section gives a more in depth explanation of the cooperative safety layer.

2.2. Cooperative Layer of Safety by UTM

The cooperative layer in the multilayered CD&R architecture given by figure 2.2 for UAVs includes autonomous, tactical implicitly coordinated CD&R methods based on a distributed dependent surveillance system [7]. There is need for an organised traffic management system as the demand for low altitude flights by UAVs is increasing today. A Concept of Operation (ConOps) initiated by NASA is the UAS Traffic Management (UTM) research initiative [10]. The UTM system is an application that aims for safe and efficient UAV operations in low altitude airspace as defined by Korpardekar et al. [10]. UTM aims for flexibility where possible and structure when necessary. The UTM system is based on the following principles [10]:

1. Only authenticated UAV operators are allowed to operate in a given airspace.

2. UAVs have to stay clear of each other and manned aviation.

3. UAV operators need to be aware of constraints, people and obstacles within the airspace they are operating in.

4. UAVs used for public safety have priority over other UAVs and manned aviation.

UTM service providers are needed in order to accomplish those basic principles. The service providers are responsible to establish a connection between drones and Air Navigation Service Providers (ANSPs). The ANSPs can provide clearances to UAV operators via the UTM service providers.

UTM service providers can also help to add a distributed dependent surveillance system to UAVs by sharing state information such as velocity and current location with nearby traffic. Syd Ali [14] proposes an architectural communication framework for UTM in his paper. The architectural framework is visualised by figure 2.3.

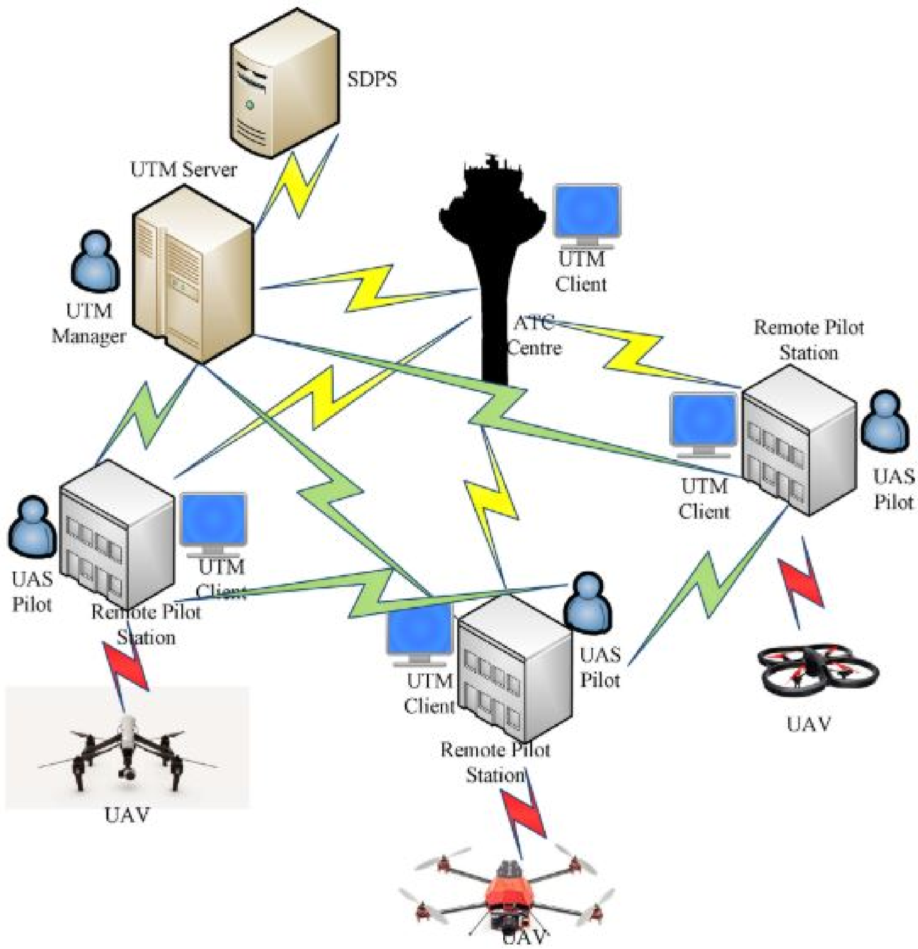

Figure 2.3: UTM architectural framework. Adapted from [14].

There is a central Surveillance Data Processing System (SDPS) in the UTM architectural framework as can be seen in figure 2.3. This server provides state information regarding manned and UAV traffic in real-time. The SDPS is connected to a UTM server which is maintained by an UTM service provider. Air Traffic Control (ATC) centres and UAV operators are connected to UTM servers of service providers.

UAV operators need to use the UTM service in order to send their flightplans to ATC and to receive clearances from ATC. UTM also increases situational awareness to UAV operators by visualising airspace restrictions, geofences and real-time surveillance data on a map.

ATC centres make use of the UTM system in order to give clearances to UAV operators. Surveillance data obtained by systems of the ATC centres is being shared with the UTM service providers. The UTM service providers share the obtained surveillance data from UAVs with the ATC centres in order to increase situational awareness of ATC.

The cooperative layer of safety in the CD&R architecture given by figure 2.2 can by implemented using the UTM framework as depicted in figure 2.3. It can be seen that the cooperative safety layer is the highest layer in the CD&R architecture which requires fully autonomous avoidance by a tactical manoeuvre. Surveillance data received from UTM providers can be categorised as implicitly coordinated dependent-distributed surveillance and can be used on-board of UAVs to generate autonomous conflict resolutions when the cooperative safety layer is triggered. UAVs can be connected to the UTM system by means of cellular network techniques such as 4G and 5G as suggested by Syd Ali [14]. The UAVs can use this surveillance data in order to generate velocity obstacles of nearby traffic and calculate tactical avoidance manoeuvres in case of conflicts.

3

Velocity Obstacle Based CD&R Methods

Velocity obstacle based CD&R methods are being investigated for manned aviation as explained in the papers by Van Dam et al. [17], Ellerbroek et al. [3] and Mercado et al. [12].

The notion of the concept of velocity obstacles is adopted from Martinoli et al. [11]. A velocity obstacle maps the colliding velocities with intruders to the own aircraft's velocity space. A collision avoidance manoeuvre can be performed by selecting a velocity outside the zones marked by velocity obstacles.

Several tactical CD&R approaches based on velocity obstacles that are found in literature are discussed in this chapter. First some definitions regarding CD&R are introduced by section 3.1 followed by an overview of conflict detection equations given by section 3.2. The basics of velocity obstacles and the solution space diagram are discussed in section 3.3. The possible strategies and rule-sets that are being used in order to resolve conflicts are discussed in section 3.4. Finally, section 3.4.3 gives an overview of conflict resolution rule-sets to be applied during experiments.

3.1. CD&R Definitions

A CD&R method consists of three parts: a conflict, a detection strategy and a resolution strategy. Terminology related to each of those three parts will be discussed in this section. In the first place, section 3.1.1 explains the definition of a conflict. Secondly, section 3.1.2 describes the definitions regarding conflict detection. Finally, section 3.1.3 describes definitions regarding conflict resolutions. Terminology and parameter names regarding CD&R are in line with the master thesis of Balasooriyan [1] and adopted from it.

3.1.1. Conflict Definitions

In order to detect and resolve conflicts, the definition of a conflict will be described throughout this section. UAVs are not allowed to fly too close to each other in terms of horizontal and vertical distance. A horizontal separation minimum of 50 meters for UAVs has already been selected by Jenie [6] and Tan [15]. The height of the minimal vertical separation has not yet been defined in literature. The set of airspace around a vehicle that contains the separation minimums is called the Protected Zone (PZ) as given by figure 3.1.

Definition 1. The **Protected Zone (PZ)** around a vehicle is a flat disk around the vehicle with a radius of R_{PZ} that is equal to the horizontal separation minimum and height h_{PZ} which is equal to 2 times the vertical separation minimum. No other traffic is allowed to penetrate the PZ of the ownship. The PZ is graphically visualised by figure 3.1.

A Loss of Separation (LoS) occurs when the PZ is penetrated by an intruder.

Definition 2. There is a **Loss of Separation (LoS)** when the PZ of the ownship is penetrated by an intruder.

An important parameter of a CD&R algorithm is the look-ahead time. A look-ahead time is selected depending on the layer of safety of the CD&R architecture and type of platform (UAV or manned traffic). A look-ahead time of 25 seconds has been defined by Jenie et al. [5] for tactical avoidance manoeuvres performed by UAVs which is in the scope of this research.

Definition 3. The **look-ahead time** (t_{LA}) is the time a CD&R algorithm looks ahead in order to detect future conflicts.

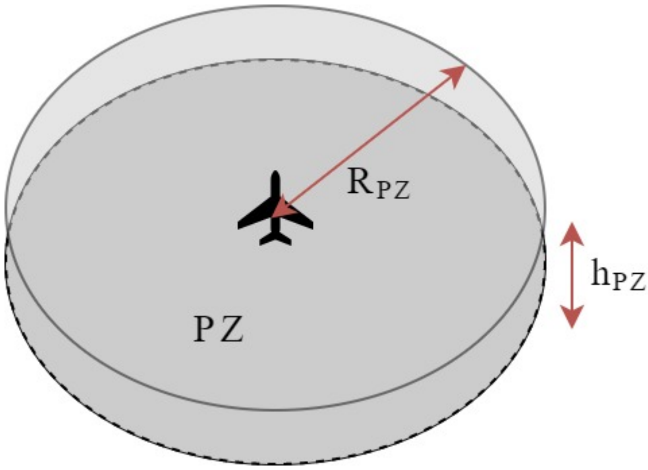

Figure 3.1: Visualisation of the PZ around an aircraft.

Finally, a conflict can be defined as the detection of a LoS within the selected look-ahead time of the CD&R algorithm.

Definition 4. A **conflict** is defined as soon there is a LoS detected within the look-ahead time of the CD&R algorithm.

3.1.2. Conflict Detection

The definitions regarding conflict detection are explained in this section. The following definition for conflict detection is quoted from Balasooriyan [1]: *"Conflict detection is the process of propagating expected trajectories of the ownship and intruders into the near future in order to find possible conflicts".* This means that all possible conflicts within the look-ahead-time are being evaluated by the detection algorithm.

Definition 5. The following definition of conflict detection is quoted from [1]: *"**Conflict detection** is the process of propagating expected trajectories of the ownship and intruders into the near future in order to find possible conflicts".*

An important parameter regarding detected conflicts is the Closest Point of Approach (CPA). The CPA gives the minimum distance between the ownship and an intruder when their expected trajectories are propagated. There is a conflict detected when the separation at the CPA is smaller than the horizontal radius of the PZ. A visual representation of the CPA is given by figure 3.2. It can be concluded that there is a conflict situation depicted in the figure as the separation at the CPA is smaller than the horizontal PZ radius of the ownship.

Definition 6. The **Closest Point of Approach (CPA)** is the minimum distance encountered between the ownship and an intruder when expected flight trajectories are propagated.

Thus VOs can help to detect conflicts and help to find a solution to a conflict by selecting a resolution speed of the ownship outside the velocity obstacle. The Solution Space Diagram (SSD) will be discussed later which will elaborate on additional constraints that have to be taken into account finding conflict resolutions for aerial vehicles.

3.1.3. Conflict Resolution

The definitions regarding conflict resolutions are explained in this section. The following definition for conflict resolution is quoted from Balasooriyan [1]: *"Conflict Resolution is the process of propagating expected trajectories of intruders into the near future to find the manoeuvres of the ownship that would resolve conflicts".*

Definition 7. The following definition of conflict resolution is quoted from [1]: *"**Conflict Resolution** is the process of propagating expected trajectories of intruders into the near future to find the manoeuvres of the ownship that would resolve conflictss".*

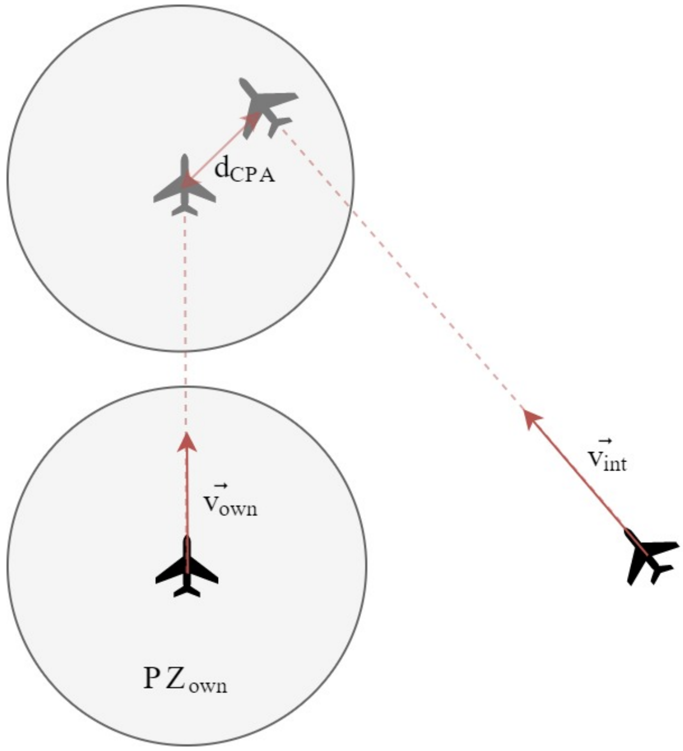

Figure 3.2: Geometry of an horizontal conflict between the ownship and an intruder aircraft.

3.2. Conflict Detection Equations

This section describes the conflict detection equations. Equations stated in this section are adopted and in line with the master thesis of Balasooriyan [1].

The relative velocity vector $\vec{v}_{rel}$ of the ownship with respect to the intruder can be calculated using equation 3.1. The relative velocity vector with respect to an intruder is equal to the own velocity vector $\vec{v}_{own}$ minus the velocity vector of the intruder $\vec{v}_{int}$.

$$\vec{v}_{rel} = \vec{v}_{own} - \vec{v}_{int} \tag{3.1}$$

The magnitude of the relative velocity vector is calculated using equation 3.2 by taking the absolute value of the relative velocity vector.

$$v_{rel} = |\vec{v}_{rel}| \tag{3.2}$$

The relative position vector $\vec{d}_{rel}$ of the own aircraft with respect to an intruder can be calculated using equation 3.3. The relative distance vector with respect to an intruder is equal to the own position vector $\vec{d}_{own}$ minus the position vector of the intruder $\vec{d}_{int}$.

$$\vec{d}_{rel} = \vec{d}_{own} - \vec{d}_{int} \tag{3.3}$$

The magnitude of the relative position vector is calculated using equation 3.4 by taking the absolute value of the relative position vector.

$$d_{rel} = \left|\vec{d}_{rel}\right| \tag{3.4}$$

The distance to the CPA can be calculated using equation 3.5. The distance to the CPA can be calculated by the dot product of the negative relative position vector $\vec{d}_{rel}$ and the relative velocity unit vector.

$$t_{CPA} \cdot v_{rel} = -\vec{d}_{rel} \cdot \frac{\vec{v}_{rel}}{v_{rel}} \tag{3.5}$$

Rewriting equation 3.5 in terms of the time to CPA t_{CPA} yields equation 3.6.

$$t_{CPA} = -\frac{\vec{d}_{rel} \cdot \vec{v}_{rel}}{v_{rel}^2} \tag{3.6}$$

The distance from the intruder to the CPA can be calculated using Pythagorean theory as given by equation 3.7.

$$d_{CPA} = \sqrt{d_{rel}^2 - t_{CPA}^2 \cdot v_{rel}^2} \tag{3.7}$$

The distance inside the protected zone to the CPA can also be calculated using Pythagorean theory using equation 3.8.

$$d_{in} = \sqrt{R_{PZ}^2 - d_{CPA}^2} \tag{3.8}$$

The distance to LoS is defined by equation 3.9. There is a LoS at the time when the PZ is penetrated. The distance to LoS is calculated by subtracting the distance in the PZ from the distance to the CPA.

$$d_{LoS} = v_{rel} \cdot t_{CPA} - d_{in} \tag{3.9}$$

The time to LoS is calculated by equation 3.10. The time to Los is equal to the time to CPA minus the time the aircraft spends inside the PZ until reaching the CPA.

$$t_{LoS} = t_{CPA} - \frac{d_{in}}{v_{rel}} \tag{3.10}$$

A conflict is detected when the time to LoS t_{LoS} is smaller or equal to the look-ahead time of the CD&R algorithm.

3.3. Velocity Obstacles

The equations and explanations given in this section are derived from Martinoli [11] and are rewritten in such a way that it matches the terminology used by Jenie [5] and Balasooriyan [1]. Firstly, the basics of velocity obstacles are explained in section 3.3.1. Secondly, section 3.3.2 explains how to construct a Solution Space Diagram (SSD) using velocity obstacles. the SSD gives a graphical overview of the reachable velocity vectors that are conflict free and which reachable velocity vectors generate conflicts.

3.3.1. Basics of Velocity Obstacles

The theory about velocity obstacles originated from robotics and are described in Martinoli's book [11]. This section explains the basics of velocity obstacles which knowledge is needed for a velocity obstacle based CD&R method.

First of all, before constructing a velocity obstacle, a so called Conflict Cone (CC) has to be constructed in the relative velocity reference frame. Therefore the relative velocity vector of the ownship with respect to an intruder needs to be computed. A CC is constructed in the relative velocity space. In this velocity space, the intruder can be seen as a static object and the relative velocity is used to detect any intrusion of the PZ in the future. A graphical representation of the relative velocity vector and a conflict cone is given by figure 3.3. The conflict cone is generated by drawing two tangent lines from the location of the ownship to the edges of the PZ of the intruder. Each relative velocity vector $\vec{v}_{rel}$ that points inside the CC causes a conflict as can be seen in the figure. Therefore, the CC is the set of relative velocity vectors for which a conflict with an intruder emerges.

Definition 8. A **Conflict Cone (CC)** is the set of relative velocity vectors $\vec{v}_{rel}$ for which a conflict with an intruder emerges.

When a CC is converted to the absolute velocity reference system of the ownship, it is called a Velocity Obstacle (VO). A velocity obstacle can be constructed by translating a CC by the intruder velocity vector $\vec{v}_{int}$ as is depicted in figure 3.4. The VO contains the set of ownship velocities that will emerge a conflict with an intruder.

Definition 9. A **Velocity Obstacle (VO)** is the set of absolute velocity vectors $\vec{v}_{own}$ of the ownship for which a conflict with an intruder emerges.

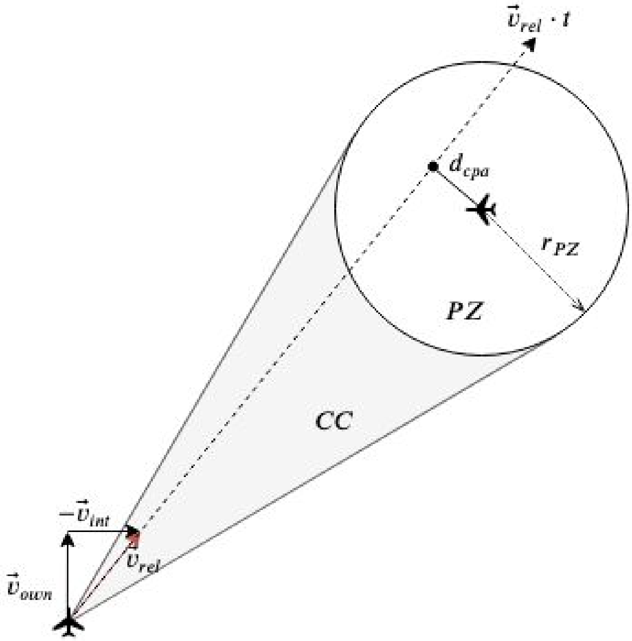

Figure 3.3: Conflict Cone (CC) visualisation.

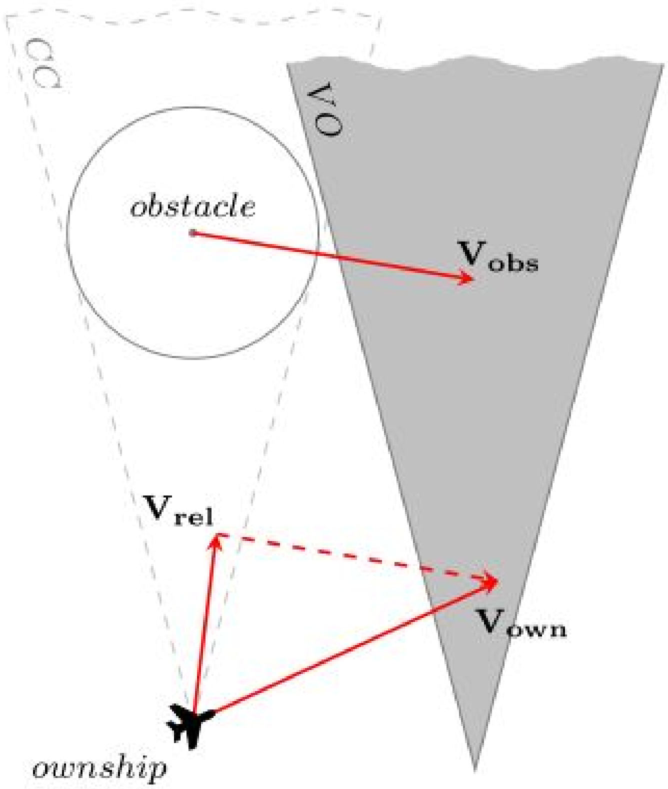

Figure 3.4: Velocity Obstacle (VO) visualisation. Adapted from [1]

3.3.2. The Solution Space Diagram

This section describes the Solution Space Diagram (SSD) that can be constructed from the set of VOs from each intruder and data on the maximum and minimum reachable speeds of the ownship. As already explained by section 3.3.1, a VO is a part of the velocity space that will emerge a conflict with an intruder if the velocity vector of the ownship points inside this VO. Taking the union of all VOs results in a map giving the Forbidden Velocities (FV) for the ownship for which conflicts emerge. The mathematical equation for the FV is given by equation 3.11. A graphical representation of a FV is given by figure 3.5.

Definition 10. The **Forbidden Velocities (FV)** are the union of all VOs for the ownship. The velocity vector of the ownship will emerge a conflict when pointing inside the FV.

$$FV = \bigcup_{i=0}^{N} VO_i \tag{3.11}$$

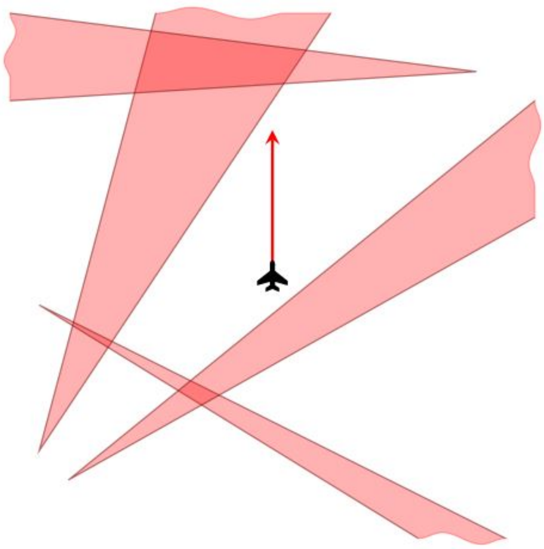

Figure 3.5: A graphical representation of a FV. Adapted from [1].

The SSD also takes into account the speed limitations of the ownship. Normally, aircraft have a maximum reachable speed and a minimal speed at which it stalls. Basically the Reachable Velocities (RV) are the set of velocities for which the length of the velocity vector is in between the maximum and minimum reachable speeds of the ownship. The mathematical form of the RV is given by equation 3.12. A graphical representation of a RV is given by figure 3.6.

Definition 11. The **Reachable Velocities (RV)** is the set of velocities the ownship can reach. The reachable velocity is smaller or equal than the maximum velocity V_{max}, but bigger or equal than the minimum velocity V_{min}.

$$RV = \left\{(x,y) \in \mathbb{R}^2 | x^2 + y^2 \geq V_{min}^2, x^2 + y^2 \leq V_{max}^2\right\} \tag{3.12}$$

Now the set of FVs and RVs have been defined, two new sets of velocity space can be introduced that are visualised by a SSD. Firstly, the set of Forbidden Reachable Velocities (FRV) is the set of RVs that intersects the set of FVs. The FRV is the set of velocities that can be reached by the ownship, but are emerging conflicts with other traffic. The FRV is mathematically expressed by equation 3.13.

Definition 12. The **Forbidden Reachable Velocities (FRV)** is the set of RVs intersecting the FVs.

$$FRV = RV \cap FV \tag{3.13}$$

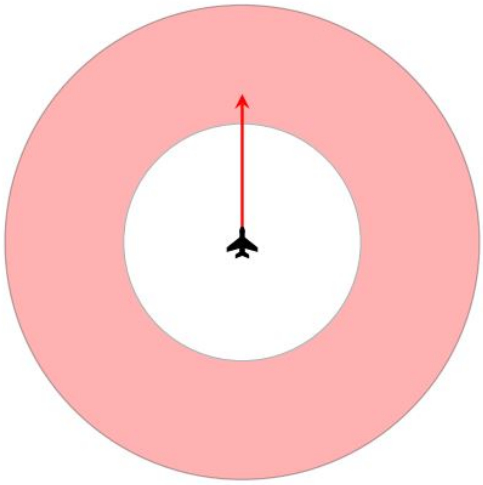

Figure 3.6: A graphical representation of a RV. Adapted from [1].

Secondly, the set of Allowed Reachable Velocities (ARV) is the set of RVs excluding the set of intersecting FVs. The ARV is the set of velocities that can be reached by the ownship for a conflict free flight path. The ARV is given by equation 3.14.

Definition 13. The **Allowed Reachable Velocities (ARV)** is the set of RVs excluding the set of intersecting FVs.

$$ARV = RV \cap FV^C \tag{3.14}$$

A graphical representation of a SSD visualising the FRV and the ARV is given by figure 3.7.

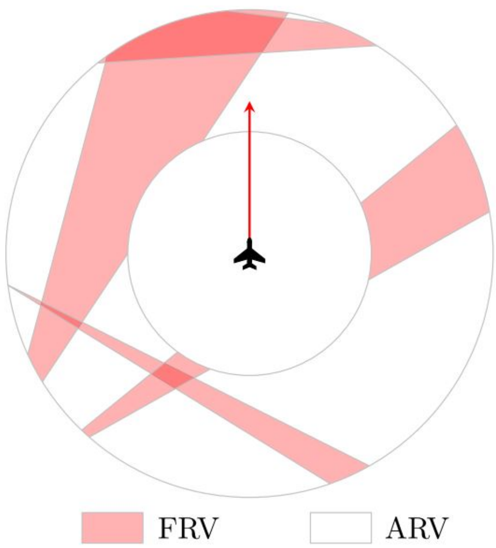

Figure 3.7: Visualisation of the FRV and ARV. Adapted from [1]

.

3.4. Conflict Resolution Strategies

Several strategies that can be used in order to resolve a conflict that are based on a velocity obstacle method are described in this section. First the Modified Voltage Potential (MVP) method is discussed in section 3.4.1.

Other strategies that can be used in order to resolve a conflict are discussed in section 3.4.2. Finally, section 3.4.3 gives a selection of conflict resolution strategies that will be applied during the experiments described in chapter 5.

3.4.1. Modified Voltage Potential

The Voltage Potential (VP) CD&R method has already been discussed in literature in 1994 by Eby [2]. The method was designed such that manned flight could following non-fixed routes via collision free paths in order to increase efficiency and airspace capacity compared to fixed routes. The MVP is a self-organising system such that traffic can reach its destination without violating the minimum separation criteria through actions performed by each individual entity in the system.

The VP conflict resolution method can be represented by a space of positively charged particles representing air traffic. A negatively charged particle represents the destination of the charged traffic. The traffic tends to move towards its destination due to the mutual attraction of opposite charges. In the meantime, the positive particles remain separated with adequate distance due to the mutual repulsion force between like charges.

However a potential field is too simplistic to apply as CD&R, it is a good starting point. In order to ensure enough separation between air traffic, Lincoln Laboratory developed an algorithm that retains the basic potential field features, but is useful to remain adequate separation [2].

Later, Hoekstra et al. [4] adapted the VP algorithm to the Modified Voltage Potential (MVP) in order to use as airborne separation module. The MVP method uses the predicted future positions of the ownship and the intruder at the CPA to generate an avoidance speed vector. The avoidance vector starts at the predicted point of CPA and is directed from the CPA perpendicular to the edge of the PZ of the intruder as can be seen in figure 3.8. The length of the avoidance vector is equal to the intrusion of the PZ of the intruder. The avoidance manoeuvre should be accomplished within the time until the CPA is reached. Therefore, by dividing the avoidance vector by the time until reaching CPA yields the avoidance velocity vector. Avoidance vectors are summed in the case of multiple conflicts within the look-ahead time. The overall resolution is self-organised if all entities in the system apply the MVP method for avoidance.

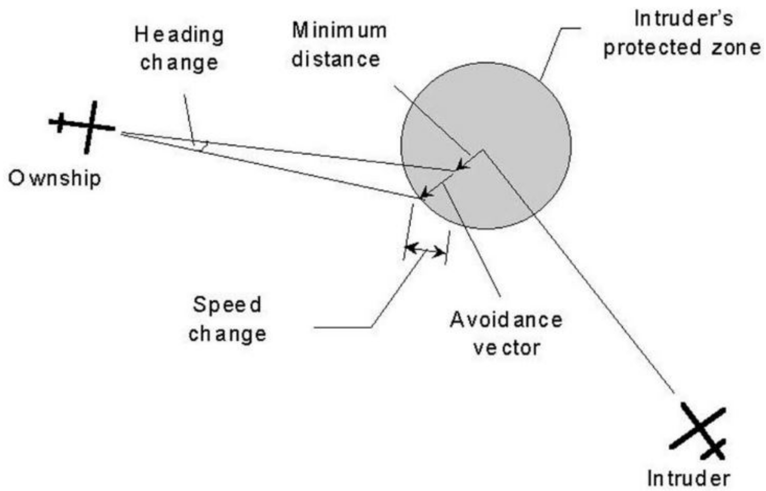

Figure 3.8: The MVP conflict resolution method. Adapted from [4]

3.4.2. Other Strategies

Other conflict resolution strategies based on velocity obstacles have been tested in an ATM simulator by Balasooriyan [1]. Six non prioritised resolution strategies have been tested that will be briefly discussed next.

Resolution Strategy 1. The shortest way out (**OPT**) strategy selects the closest point on the ARV from the current velocity vector.

Resolution Strategy 2. The clockwise turning (**RIGHT**) strategy only allows right-turning resolution velocities by reducing the left side of the ARV.

Resolution Strategy 3. The heading change (**HDG**) strategy only allows the ownship to resolve conflicts by means of a heading change.

Resolution Strategy 4. The speed change (**SPD**) strategy only allows the ownship to resolve conflicts by means of changing the magnitude of the velocity vector.

Resolution Strategy 5. The shortest from target heading (**DEST**) strategy only allows an avoidance manoeuvre in the direction closest to the target heading.

Resolution Strategy 6. The rules of the air (**ROTA**) strategy uses the rules of the air to resolve conflicts. This means that vehicles coming from the right have priority and that the direction of avoidance is directed to the right in case of a head-on conflict.

A visualisation of those 6 resolution strategies are graphically indicated on a SSD given by figure 3.9. Next, the selection of candidate strategies that are of interest for the current research are presented in section 3.4.3.

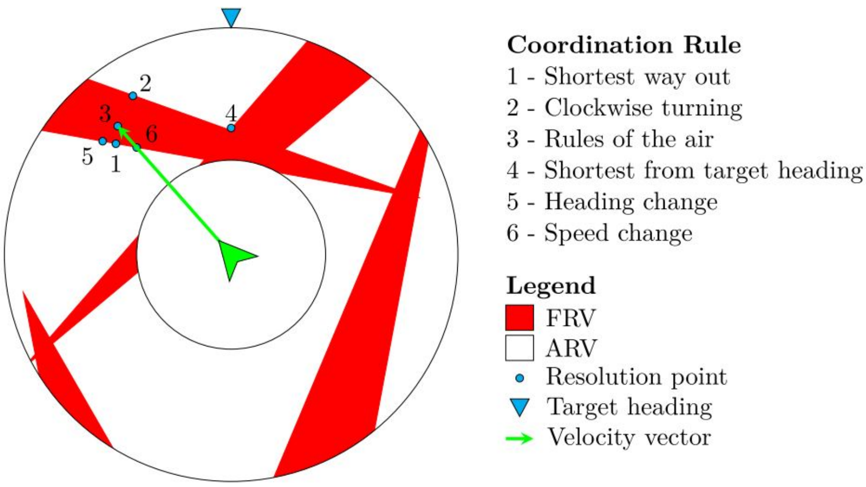

Figure 3.9: Resolution strategies indicated on a SSD. Adapted from [1]

3.4.3. Candidate Strategies

This section describes which conflict resolution strategies will be used for the experiments of this research. The applicability of the strategies discussed in sections 3.4.1 and 3.4.2 will be assessed for the current research. The biggest additional constraint of the current research is the horizontally constrained airspace in which an avoidance manoeuvre has to be performed.

Because of the horizontal constraints on the airspace, the clockwise turning and rules of the air resolution strategies have been excluded for this research. Those two strategies have a fixed direction to avoid which will not always be possible with the presence of geofences and wind. For example, if a geofence segment is located at the right side of the ownship, the rules of the air and the clockwise strategy are not applicable as the ownship has no room at the right side to perform an avoidance manoeuvre. Also the MVP is not applicable within a geofenced airspace as the direction of avoidance of the MVP method depends on the predicted situation at the CPA.

To summarise, the following strategies will be assessed in the experiments described in chapter 5:

1. Shortest way out (OPT)
2. Shortest from target heading (DEST)
3. Heading change (HDG)
4. Speed change (SPD)

Additionally, a new set of avoidance rules can be implemented and tested based on the results of the experiments described in chapter 5. For example, a rule-set that gives priority to UAVs that fly close to geofences can be tested.

4

Modelling a Geofence as Velocity Obstacle

For the research described in this thesis, the SSD has been extended in order to create velocity obstacles regarding convex geofences which may not be crossed during an UAV mission. A velocity obstacle of a geofence is being generated as soon as a conflict is detected by the CD algorithm. The velocity obstacle of a geofence maps the set of resolution velocities for which the CPA with an intruder lies outside the geofence.

4.1. Equation derivation

A geofence segment is represented by a linear line in a two dimensional axis system where $\hat{x}$ and $\hat{y}$ are the primary axes and are oriented in East and North direction respectively. Each line composing the convex geofence is named a geofence segment. A simple linear vector equation is represented by equation 4.1, where $\vec{r}$ represents the line vector for each value of parameter λ. The vectors $\vec{a}$ and $\vec{b}$ represent two distinct position vectors of two arbitrary points on the line vector. A visual representation of a geofence segment as vector is given by figure 4.1. The index of an geofence segment is denoted by i.

$$\vec{r} = \vec{a} + \lambda\vec{u} = \vec{a} + \lambda\left(\vec{b} - \vec{a}\right) \tag{4.1}$$

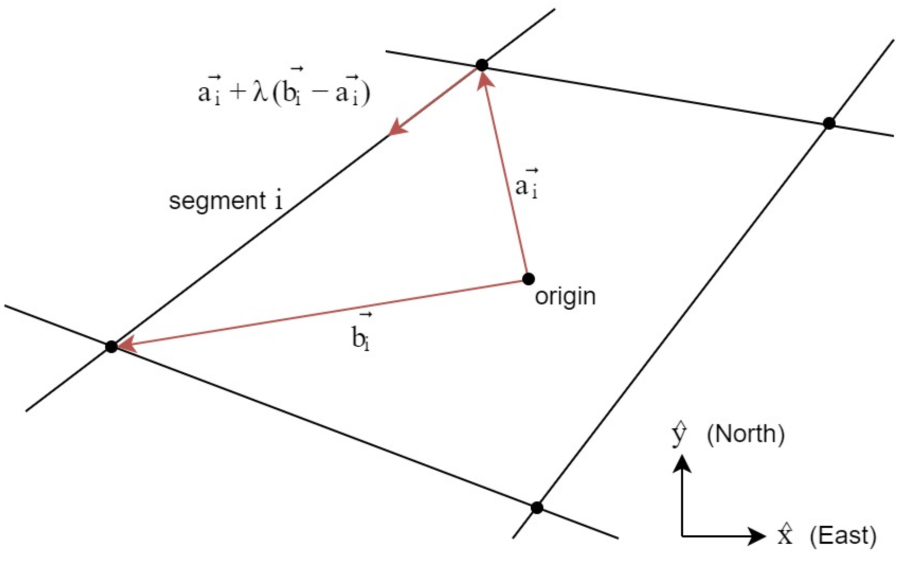

Figure 4.1: Visualisation of the reference axis system and a convex geofence segment as vector.

The value giving the time to the CPA is given by equation 4.2. The time to the CPA is referenced as time to resolution t_{res} in the equation as the CPA is located at the resolution point $\vec{p}_{res}$ for a given resolution speed vector $\vec{v}_{res}$. The vectors $\vec{d}_{own}$ and $\vec{d}_{int}$ represent the position vectors of the ownship and an intruder respectively. The $\vec{v}_{res}$ and $\vec{v}_{int}$ represent the own resolution speed and intruder speed vectors respectively.

$$t_{res} = -\frac{\left(\vec{d}_{own} - \vec{d}_{int}\right)\cdot(\vec{v}_{res} - \vec{v}_{int})}{(\vec{v}_{res} - \vec{v}_{int})\cdot(\vec{v}_{res} - \vec{v}_{int})} \tag{4.2}$$

In order to calculate the resolution position $\vec{p}_{res}$ in a two dimensional space, one has to multiply the resolution speed vector $\vec{v}_{res}$ with the time to resolution t_{res} and add the current position $\vec{d}_{own}$ of the ownship. The equation used to calculate the resolution position is given by equation 4.3.

$$\vec{p}_{res} = t_{res}\vec{v}_{res} + \vec{d}_{own} = -\frac{\left(\vec{d}_{own} - \vec{d}_{int}\right)\cdot(\vec{v}_{res} - \vec{v}_{int})}{(\vec{v}_{res} - \vec{v}_{int})\cdot(\vec{v}_{res} - \vec{v}_{int})}\vec{v}_{res} + \vec{d}_{own} \tag{4.3}$$

The value of the time until reaching the resolution point $\vec{p}_{res}$ should be in the future and thus should take a value greater than zero as indicated by equation 4.4.

$$t_{res} \geq 0 \tag{4.4}$$

Equation 4.3 should be solved for the positive values of t_{res}. Therefore the numerator of equation 4.2 should be equal or smaller than zero as the denominator is always positive because it is an inner vector product. That is why equation 4.5 should hold for any calculated resolution.

$$\left(\vec{d}_{own} - \vec{d}_{int}\right)\cdot(\vec{v}_{res} - \vec{v}_{int}) \leq 0 \tag{4.5}$$

The resolution point $\vec{p}_{res}$ and a line segment $\vec{r}$ of the convex geofence coincide when $\vec{p}_{res}$ is equal to $\vec{r}$. The 2D space around the own aircraft can be modelled with the own aircraft located at the origin of the axis system such that equation 4.6 holds.

$$\vec{d}_{own} = \vec{0} \tag{4.6}$$

Setting the position of the own aircraft $\vec{d}_{own}$ at the origin of the axis system results in a simplification of equation 4.3. The $\vec{d}_{own}$ term drops out of the equation resulting in the form given by equation 4.7.

$$\vec{p}_{res} = \frac{\vec{d}_{int}\cdot(\vec{v}_{res} - \vec{v}_{int})}{(\vec{v}_{res} - \vec{v}_{int})\cdot(\vec{v}_{res} - \vec{v}_{int})}\vec{v}_{res} \tag{4.7}$$

The resolution points $\vec{p}_{res}$ that lie on geofence segment i can be found using equation 4.8 by substituting $\vec{p}_{res}$ by the line vector equation of a geofence segment as given by equation 4.1.

$$\vec{v}_{res}\frac{\vec{d}_{int}\cdot(\vec{v}_{res} - \vec{v}_{int})}{(\vec{v}_{res} - \vec{v}_{int})\cdot(\vec{v}_{res} - \vec{v}_{int})} = \vec{a}_i + \lambda\left(\vec{b}_i - \vec{a}_i\right) \tag{4.8}$$

The resolution points $\vec{p}_{res}$ should be located within the geofence such that a UAV can perform its avoidance manoeuvre without geofence violations. Therefore, it is important to solve equation 4.8 for the resolution velocity vector $\vec{v}_{res}$ such that velocity obstacles can be constructed for convex geofence segments and visualised on a SSD.

Another reference system will be introduced that is parallel to a geofence segment by rotating the reference system by angle ϕ_i such that the rotated $\hat{x}$ axis is parallel to the geofence segment in Counter Clockwise (CCW) direction as visualised by figure 4.2. The primary axes of this new geofence segment aligned axis system are called $\hat{x}_i^{'}$ and $\hat{y}_i^{'}$ respectively. The axis system can be rotated using the rotation matrix R given by equation 4.9.

$$R = \begin{bmatrix} \cos(\phi_i) & -\sin(\phi_i) \\ \sin(\phi_i) & \cos(\phi_i) \end{bmatrix} \tag{4.9}$$

The distance from the ownship to a geofence segment d_{geo_i} can be expressed in terms of the primary axes of the axis system aligned with the geofence segment. As the $\hat{x}_i^{'}$ axis is parallel to the geofence segment in CCW direction, the $\hat{y}_i^{'}$ axis points towards the inside of the geofence as can be seen in figure 4.2. The distance of the own aircraft with respect to the geofence segment can therefore be expressed as a dot product given by equation 4.10. Performing a dot product between the primary $\hat{y}_i^{'}$ axis and an arbitrary point on the geofence segment gives the negative distance from the ownship to that geofence segment.

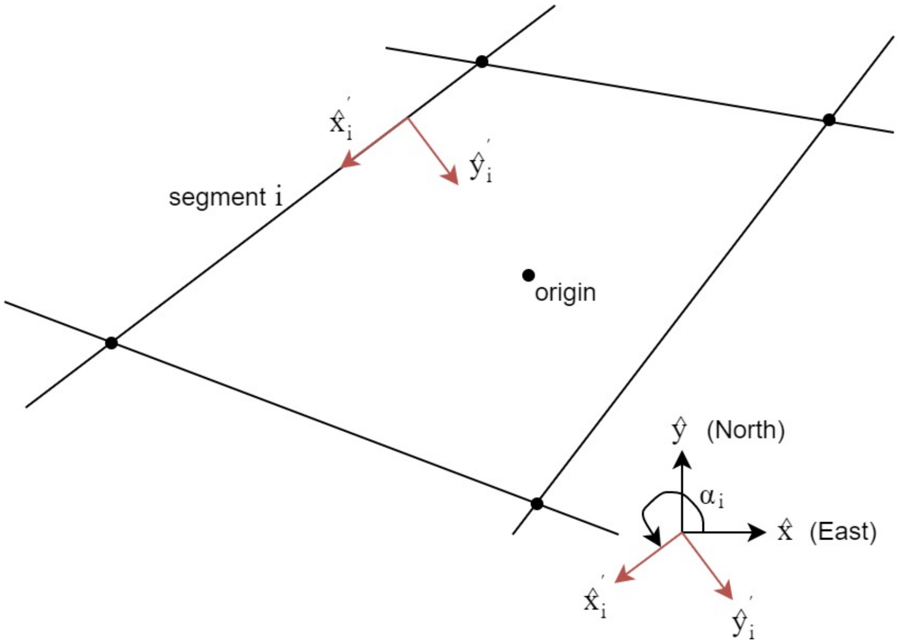

Figure 4.2: Visualisation of the rotated axis system by angle α_i to align it with geofence segment i.

$$\vec{a}_i \cdot \hat{y}_i' = \vec{b}_i \cdot \hat{y}_i' = -d_{geo_i} \tag{4.10}$$

Performing a dot product with $\hat{y}_i'$ on both sides of equation 4.8 yields equation 4.11.

$$\left(\vec{v}_{res} \cdot \hat{y}_i'\right) \frac{\vec{d}_{int} \cdot (\vec{v}_{res} - \vec{v}_{int})}{(\vec{v}_{res} - \vec{v}_{int}) \cdot (\vec{v}_{res} - \vec{v}_{int})} = -d_{geo_i} \tag{4.11}$$

Rewriting equation 4.11 in terms of $\vec{v}_{res}$ coordinates in terms of the reference system aligned with the geofence gives equation 4.12.

$$\left(\vec{v}_{res} \cdot \hat{y}_i'\right) \frac{\left(\vec{d}_{int} \cdot \hat{x}_i'\right)\left(\vec{v}_{res} \cdot \hat{x}_i'\right) + \left(\vec{d}_{int} \cdot \hat{y}_i'\right)\left(\vec{v}_{res} \cdot \hat{y}_i'\right) - \vec{d}_{int} \cdot \vec{v}_{int}}{\left(\vec{v}_{res} \cdot \hat{x}_i'\right)^2 - 2\left(\vec{v}_{res} \cdot \hat{x}_i'\right)\left(\vec{v}_{int} \cdot \hat{x}_i'\right) + \left(\vec{v}_{res} \cdot \hat{y}_i'\right)^2 - 2\left(\vec{v}_{res} \cdot \hat{y}_i'\right)\left(\vec{v}_{int} \cdot \hat{y}_i'\right) + \vec{v}_{int} \cdot \vec{v}_{int}} = -d_{geo_i} \tag{4.12}$$

Reordering equation 4.12 such that the right side of the equation equals zero yields equation 4.13.

$$\begin{aligned} &\left(\vec{v}_{res} \cdot \hat{x}_i'\right)^2 - 2\left(\vec{v}_{res} \cdot \hat{x}_i'\right)\left(\vec{v}_{int} \cdot \hat{x}_i'\right) + \left(\vec{v}_{res} \cdot \hat{y}_i'\right)^2 - 2\left(\vec{v}_{res} \cdot \hat{y}_i'\right)\left(\vec{v}_{int} \cdot \hat{y}_i'\right) + \vec{v}_{int} \cdot \vec{v}_{int} \\ &+ \left(\vec{v}_{res} \cdot \hat{y}_i'\right) \frac{\left(\vec{d}_{int} \cdot \hat{x}_i'\right)\left(\vec{v}_{res} \cdot \hat{x}_i'\right) + \left(\vec{d}_{int} \cdot \hat{y}_i'\right)\left(\vec{v}_{res} \cdot \hat{y}_i'\right) - \vec{d}_{int} \cdot \vec{v}_{int}}{d_{geo_i}} = 0 \end{aligned} \tag{4.13}$$

Collecting resolution speed terms in terms of the primary axes parallel to the geofence $\hat{x}_i'$ and perpendicular to the geofence pointing inwards $\hat{y}_i'$ yields equation 4.14.

$$
\begin{aligned}
&\left(\vec{v}_{res}\cdot\hat{x}_i^{'}\right)^2\\
&+\left(\vec{v}_{res}\cdot\hat{x}_i^{'}\right)\left(-2\vec{v}_{int}\cdot\hat{x}_i^{'}\right)\\
&+\left(\vec{v}_{res}\cdot\hat{y}_i\right)^2\left(1+\frac{\vec{d}_{int}\cdot\hat{y}_i^{'}}{d_{geo_i}}\right)\\
&+\left(\vec{v}_{res}\cdot\hat{y}_i^{'}\right)\left(-2\vec{v}_{int}\cdot\hat{y}_i^{'}-\frac{\vec{d}_{int}\cdot\vec{v}_{int}}{d_{geo_i}}\right)\\
&+\left(\vec{v}_{res}\cdot\hat{x}_i^{'}\right)\left(\vec{v}_{res}\cdot\hat{y}_i^{'}\right)\left(\frac{\vec{d}_{int}\cdot\hat{x}_i^{'}}{d_{geo_i}}\right)\\
&+\vec{v}_{int}\cdot\vec{v}_{int}=0
\end{aligned}
\tag{4.14}
$$

It can be concluded from equation 4.14 that a cross term between the resolution speed terms is present in the geofence aligned reference system. Assume that there exists a rotation angle $\phi^{'}$ with respect to the geofence segment aligned reference system such that the cross term cancels out of the equation. The $\left(\vec{v}_{res}\cdot\hat{x}_i^{'}\right)$ and $\left(\vec{v}_{res}\cdot\hat{y}_i^{'}\right)$ terms can be expressed in this new rotated reference frame with primary axes $\hat{x}_i^{''}$ and $\hat{y}_i^{''}$ using the transformation matrix R' given by equation 4.15.

$$
R^{'}=\begin{bmatrix}\cos\left(\phi_i^{'}\right) & -\sin\left(\phi_i^{'}\right)\\ \sin\left(\phi_i^{'}\right) & \cos\left(\phi_i^{'}\right)\end{bmatrix}
\tag{4.15}
$$

Expressing $\hat{x}_i^{'}$ and $\hat{y}_i^{'}$ in terms of $\hat{x}_i^{''}$ and $\hat{y}_i^{''}$ using the transformation matrix given by equation 4.15 yields equations 4.16 and 4.17 respectively.

$$
\hat{x}_i^{'}=R^{'T}\hat{x}_i^{''}=\hat{x}_i^{''}\cos\left(\phi_i^{'}\right)-\hat{y}_i^{''}\sin\left(\phi_i^{'}\right)
\tag{4.16}
$$

$$
\hat{y}_i^{'}=R^{'T}\hat{y}_i^{''}=\hat{x}_i^{''}\sin\left(\phi_i^{'}\right)+\hat{y}_i^{''}\cos\left(\phi_i^{'}\right)
\tag{4.17}
$$

The $\left(\vec{v}_{res}\cdot\hat{x}_i^{'}\right)$ and $\left(\vec{v}_{res}\cdot\hat{y}_i^{'}\right)$ terms in equation 4.14 can be rewritten in terms of the axis system rotated by an additional angle of $\phi_i^{'}$. Applying the rotation matrix given by equation 4.15 yields the relevant terms present in equation 4.14 in terms of the $\hat{x}_i^{''}$ and $\hat{y}_i^{''}$ primary axes as given by equations 4.18 - 4.22.

$$
\left(\vec{v}_{res}\cdot\hat{x}_i^{'}\right)^2+\left(\vec{v}_{res}\cdot\hat{y}_i^{'}\right)^2=\left(\vec{v}_{res}\cdot\hat{x}_i^{''}\right)^2+\left(\vec{v}_{res}\cdot\hat{y}_i^{''}\right)^2
\tag{4.18}
$$

$$
\left(\vec{v}_{res}\cdot\hat{y}_i^{'}\right)^2=\left(\vec{v}_{res}\cdot\hat{x}_i^{''}\right)^2\sin^2\left(\phi_i^{'}\right)+\left(\vec{v}_{res}\cdot\hat{y}_i^{''}\right)^2\cos^2\left(\phi_i^{'}\right)+2\left(\vec{v}_{res}\cdot\hat{x}_i^{''}\right)\left(\vec{v}_{res}\cdot\hat{y}_i^{''}\right)\cos\left(\phi_i^{'}\right)\sin\left(\phi_i^{'}\right)
\tag{4.19}
$$

$$
\left(\vec{v}_{res}\cdot\hat{x}_i^{'}\right)=\left(\vec{v}_{res}\cdot\hat{x}_i^{''}\right)\cos\left(\phi_i^{'}\right)-\left(\vec{v}_{res}\cdot\hat{y}_i^{''}\right)\sin\left(\phi_i^{'}\right)
\tag{4.20}
$$

$$
\left(\vec{v}_{res}\cdot\hat{y}_i^{'}\right)=\left(\vec{v}_{res}\cdot\hat{x}_i^{''}\right)\sin\left(\phi_i^{'}\right)+\left(\vec{v}_{res}\cdot\hat{y}_i^{''}\right)\cos\left(\phi_i^{'}\right)
\tag{4.21}
$$

$$
\begin{aligned}
&\left(\vec{v}_{res}\cdot\hat{x}_i^{'}\right)\left(\vec{v}_{res}\cdot\hat{y}_i^{'}\right)\\
&=\left(\left(\vec{v}_{res}\cdot\hat{x}_i^{''}\right)^2-\left(\vec{v}_{res}\cdot\hat{y}_i^{''}\right)^2\right)\cos\left(\phi_i^{'}\right)\sin\left(\phi_i^{'}\right)+\left(\vec{v}_{res}\cdot\hat{x}_i^{''}\right)\left(\vec{v}_{res}\cdot\hat{y}_i^{''}\right)\left(\cos^2\left(\phi_i^{'}\right)-\sin^2\left(\phi_i^{'}\right)\right)
\end{aligned}
\tag{4.22}
$$

Collecting terms of $\left(\vec{v}_{res}\cdot\hat{x}_i^{''}\right)$ and $\left(\vec{v}_{res}\cdot\hat{y}_i^{''}\right)$ and their exponentials and cross terms results in the equation form given by equation 4.23.

$$
\begin{aligned}
&\left(\vec{v}_{res}\cdot\hat{x}_i''\right)^2\left(1+\sin\left(\phi_i'\right)\frac{\left(\vec{d}_{int}\cdot\hat{y}_i'\right)\sin\left(\phi_i'\right)+\left(\vec{d}_{int}\cdot\hat{x}_i'\right)\cos\left(\phi_i'\right)}{d_{geo_i}}\right)\\
&+\left(\vec{v}_{res}\cdot\hat{y}_i''\right)^2\left(1+\cos\left(\phi_i'\right)\frac{\left(\vec{d}_{int}\cdot\hat{y}_i'\right)\cos\left(\phi_i'\right)-\left(\vec{d}_{int}\cdot\hat{x}_i'\right)\sin\left(\phi_i'\right)}{d_{geo_i}}\right)\\
&+\left(\vec{v}_{res}\cdot\hat{x}_i''\right)\left(-2\left(\vec{v}_{int}\cdot\hat{x}_i'\right)\cos\left(\phi_i'\right)-2\left(\vec{v}_{int}\cdot\hat{y}_i'\right)\sin\left(\phi_i'\right)-\sin\left(\phi_i'\right)\frac{\vec{d}_{int}\cdot\vec{v}_{int}}{d_{geo_i}}\right)\\
&+\left(\vec{v}_{res}\cdot\hat{y}_i''\right)\left(2\left(\vec{v}_{int}\cdot\hat{x}_i'\right)\sin\left(\phi_i'\right)-2\left(\vec{v}_{int}\cdot\hat{y}_i'\right)\cos\left(\phi_i'\right)-\cos\left(\phi_i'\right)\frac{\vec{d}_{int}\cdot\vec{v}_{int}}{d_{geo_i}}\right)\\
&+\left(\vec{v}_{res}\cdot\hat{x}_i''\right)\left(\vec{v}_{res}\cdot\hat{y}_i''\right)\left(\frac{\left(\vec{d}_{int}\cdot\hat{x}_i'\right)\left(\cos^2\left(\phi_i'\right)-\sin^2\left(\phi_i'\right)\right)+2\left(\vec{d}_{int}\cdot\hat{y}_i'\right)\sin\left(\phi_i'\right)\cos\left(\phi_i'\right)}{d_{geo_i}}\right)\\
&+\left(\vec{v}_{int}\cdot\hat{x}_i'\right)^2+\left(\vec{v}_{int}\cdot\hat{y}_i'\right)^2=0
\end{aligned}
\tag{4.23}
$$

It was assumed that there exist a rotation angle ϕ_i' such that the cross term $\left(\vec{v}_{res}\cdot\hat{x}_i''\right)\left(\vec{v}_{res}\cdot\hat{y}_i''\right)$ cancels out in equation 4.23. Therefore equation 4.24 should hold for rotation angle ϕ_i'.

$$
-\frac{\vec{d}_{int}\cdot\hat{x}_i'}{\vec{d}_{int}\cdot\hat{y}_i'}=\frac{2\sin\left(\phi_i'\right)\cos\left(\phi_i'\right)}{\cos^2\left(\phi_i'\right)-\sin^2\left(\phi_i'\right)}=\tan\left(2\phi_i'\right)
\tag{4.24}
$$

Equations 4.25 and 4.26 can be used to express the primary $\hat{x}_i''$ and $\hat{y}_i''$ axes in terms of the primary axes parallel and perpendicular to the geofence respectively.

$$
\hat{x}_i''=R\hat{x}_i'=\hat{x}_i'\cos\left(\phi_i'\right)+\hat{y}_i'\sin\left(\phi_i'\right)
\tag{4.25}
$$

$$
\hat{y}_i''=R\hat{y}_i'=-\hat{x}_i'\sin\left(\phi_i'\right)+\hat{y}_i'\cos\left(\phi_i'\right)
\tag{4.26}
$$

Terms given by equations 4.27 - 4.30 can be simplified when rewriting them in terms of the $\hat{x}_i''$ and $\hat{y}_i''$ primary axes.

$$
\left(\vec{d}_{int}\cdot\hat{x}_i'\right)\cos\left(\phi_i'\right)+\left(\vec{d}_{int}\cdot\hat{y}_i'\right)\sin\left(\phi_i'\right)=\vec{d}_{int}\cdot\hat{x}_i''
\tag{4.27}
$$

$$
-\left(\vec{d}_{int}\cdot\hat{x}_i'\right)\sin\left(\phi_i'\right)+\left(\vec{d}_{int}\cdot\hat{y}_i'\right)\cos\left(\phi_i'\right)=\vec{d}_{int}\cdot\hat{y}_i''
\tag{4.28}
$$

$$
\left(\vec{v}_{int}\cdot\hat{x}_i'\right)\cos\left(\phi_i'\right)+\left(\vec{v}_{int}\cdot\hat{y}_i'\right)\sin\left(\phi_i'\right)=\vec{v}_{int}\cdot\hat{x}_i''
\tag{4.29}
$$

$$
-\left(\vec{v}_{int}\cdot\hat{x}_i'\right)\sin\left(\phi_i'\right)+\left(\vec{v}_{int}\cdot\hat{y}_i'\right)\cos\left(\phi_i'\right)=\vec{v}_{int}\cdot\hat{y}_i''
\tag{4.30}
$$

Setting the cross term given in equation 4.23 equal to 0 and substitution of the simplified terms given by equations 4.27 - 4.30 yields equation 4.31.

$$
\begin{aligned}
&\left(\vec{v}_{res}\cdot\hat{x}_i^{''}\right)^2\left(1+\sin\left(\phi_i^{'}\right)\frac{\vec{d}_{int}\cdot\hat{x}_i^{''}}{d_{geo_i}}\right)\\
&+\left(\vec{v}_{res}\cdot\hat{y}_i^{''}\right)^2\left(1+\cos\left(\phi_i^{'}\right)\frac{\vec{d}_{int}\cdot\hat{y}_i^{''}}{d_{geo_i}}\right)\\
&+\left(\vec{v}_{res}\cdot\hat{x}_i^{''}\right)\left(-2\left(\vec{v}_{int}\cdot\hat{x}_i^{''}\right)-\sin\left(\phi_i^{'}\right)\frac{\vec{d}_{int}\cdot\vec{v}_{int}}{d_{geo_i}}\right)\\
&+\left(\vec{v}_{res}\cdot\hat{y}_i^{''}\right)\left(-2\left(\vec{v}_{int}\cdot\hat{y}_i^{''}\right)-\cos\left(\phi_i^{'}\right)\frac{\vec{d}_{int}\cdot\vec{v}_{int}}{d_{geo_i}}\right)\\
&=-\left(\vec{v}_{int}\cdot\hat{x}_i^{'}\right)^2-\left(\vec{v}_{int}\cdot\hat{y}_i^{'}\right)^2
\end{aligned}
\tag{4.31}
$$

Then define terms given by equations 4.32 - 4.35 in order to make equation 4.31 readable in one line.

$$C_1=\left(1+\sin\left(\phi_i^{'}\right)\frac{\vec{d}_{int}\cdot\hat{x}_i^{''}}{d_{geo_i}}\right)\tag{4.32}$$

$$C_2=\left(1+\cos\left(\phi_i^{'}\right)\frac{\vec{d}_{int}\cdot\hat{y}_i^{''}}{d_{geo_i}}\right)\tag{4.33}$$

$$C_3=\left(-2\left(\vec{v}_{int}\cdot\hat{x}_i^{''}\right)-\sin\left(\phi_i^{'}\right)\frac{\vec{d}_{int}\cdot\vec{v}_{int}}{d_{geo_i}}\right)\tag{4.34}$$

$$C_4=\left(-2\left(\vec{v}_{int}\cdot\hat{y}_i^{''}\right)-\cos\left(\phi_i^{'}\right)\frac{\vec{d}_{int}\cdot\vec{v}_{int}}{d_{geo_i}}\right)\tag{4.35}$$

Substituting the expressions given by equations 4.32 - 4.35 into equation 4.31 yields equation 4.36.

$$\left(\vec{v}_{res}\cdot\hat{x}_i^{''}\right)^2C_1+\left(\vec{v}_{res}\cdot\hat{y}_i^{''}\right)^2C_2+\left(\vec{v}_{res}\cdot\hat{x}_i^{''}\right)C_3+\left(\vec{v}_{res}\cdot\hat{y}_i^{''}\right)C_4=-|\vec{v}_{int}|^2\tag{4.36}$$

Rewriting equation 4.36 gives equation 4.37 for which the expressions of $C_{x_i}^{''}$ and $C_{y_i}^{''}$ are given by equations 4.38 and 4.39 respectively.

$$C_1\left(\vec{v}_{res}\cdot\hat{x}_i^{''}-C_{x_i^{''}}\right)^2+C_2\left(\vec{v}_{res}\cdot\hat{y}_i^{''}-C_{y_i^{''}}\right)^2=-|\vec{v}_{int}|^2+C_1C_{x_i^{''}}^2+C_2C_{y_i^{''}}^2\tag{4.37}$$

$$C_{x_i^{''}}=-\frac{C_3}{2C_1}\tag{4.38}$$

$$C_{y_i^{''}}=-\frac{C_4}{2C_2}\tag{4.39}$$

Now by defining a_i^2 and b_i^2 terms as given by equations 4.40 and 4.41 yields equation 4.42, which reflects the geometry of the VO generated for geofence segment i as result of a conflict with an intruder. More explanation about the geometry of those velocity obstacles is explained in section 4.2.

$$a_i^2=\frac{-|\vec{v}_{int}|^2+C_1C_{x''}^2+C_2C_{y_i^{''}}^2}{C_1}=\frac{-|\vec{v}_{int}|^2+C_2C_{y_i^{''}}^2}{C_1}+C_{x_i^{''}}^2\tag{4.40}$$

$$b_i^2=\frac{-|\vec{v}_{int}|^2+C_1C_{x''}^2+C_2C_{y_i^{''}}^2}{C_2}=\frac{-|\vec{v}_{int}|^2+C_1C_{x_i^{''}}^2}{C_2}+C_{y_i^{''}}^2\tag{4.41}$$

$$\frac{\left(\vec{v}_{res}\cdot\hat{x}_i^{''}-C_{x_i^{''}}\right)^2}{a_i^2}+\frac{\left(\vec{v}_{res}\cdot\hat{y}_i^{''}-C_{y_i^{''}}\right)^2}{b_i^2}=1\tag{4.42}$$

4.2. Geometry of Velocity Obstacles

It can be concluded from equation 4.42 that the VOs generated for geofence segments are elliptical shaped or shaped like another conical section such as a hyperbola or parabola. Since the range for the value of the secondary rotation angle $\phi_i^{'}$ is running from $-\frac{\pi}{2}$ to $\frac{\pi}{2}$, the value of b^2 can turn negative whereas the value of a^2 remains always positive. The VO of a geofence segment will be shaped depending on the sign of the b^2 parameter. The VO will be elliptical for positive values of b^2. The VO will turn into a hyperbolic shape for negative values of the b^2 parameter. Last, the VO will be shaped parabolic if the b^2 parameter tends to go the infinity.

Appendix A describes the VOs of geofence segments in more detail. Section A.1 gives an overview of the algorithms to be implemented in computer code in order to construct VOs of geofence segments. Section A.2 gives insight in the correlations and shapes of the VOs of geofence segments.

5

Experimental Set-Up

This chapter describes the parameters, set-up and the expected form of the results of the experiments to be performed. The parameters being used for the CD&R algorithm are discussed by section 5.1. Section 5.2 describes the simulation experiments to be performed according to a set of hypotheses that are being tested.. The form of the experimental simulation results is discussed in this section as well. Section 5.3 gives a brief explanation how flight test data can be used in order to validate simulation results. Finally, section 5.4 discussed the outcome and relevance of the current research to the body of knowledge.

5.1. Parameters

The parameters that are being set for the experiments are discussed in this section. The parameters regarding the models of simulated UAVs are being extracted from literature in order to represent a representative range of UAVs that are being operated today. Parameter tables are given in this section presenting parameters to be set for the CD&R algorithm to be operated. There is a distinction made between general parameters that are constant irrespective of the UAV platform or experiment type. Other more specific parameters are given that depends on the UAV platform type and experiment type.

General parameters for the CD&R algorithm are given by table 5.1. Those parameters are constant for simulation experiments and flight tests and are irrespective of UAV platform type. The value for the radius of the protected zone and look-ahead time are taken from the paper of Jenie [5], which describes a simulation experiment on a velocity obstacle based CD&R method for UAVs. The maximum value of the wind speed is adopted from the flying rules of the Rescue UAV Challenge [16], which represent real operation maximums for drones being developed in the near future.

Parameter	Symbol	Value / Range	Unit
Protected Zone Radius	R_{PZ}	50 [5]	m
Lookahead Time	$t_{lookahead}$	25 [5]	s
Wind Direction	w_{dir}	$[0, 2\pi]$	rad
Wind Speed	V_{wind}	[0, 12.5] [16]	m/s

Table 5.1: General CD&R parameters.

Specific parameters for simulated rotorcraft UAVs are given by table 5.2. This table gives the specific parameter values and ranges for rotorcraft UAVs to be simulated during the experiments. It is assumed that a rotorcraft can hover an thus can reach a minimum airspeed of 0 m/s. A range for the maximum airspeed is given which contains the maximum airspeeds the majority of rotorcraft UAVs can reach.

Parameter	Symbol	Value / Range	Unit
Minimum Speed	V_{min}	0	m/s
Maximum Speed	V_{max}	[10, 20]	m/s

Table 5.2: Specific parameters for ATM simulation of rotorcraft

Specific parameters for simulated fixed wing UAVs are given by table 5.3. This table gives the specific parameter ranges for fixed wing UAVs to be simulated during the experiments. The minimum and maximum airspeed ranges are chosen in such a way that it contains the majority of commercial fixed wing UAVs as also given by the paper of Jenie [8]. It is assumed that the minimum speeds of fixed wings are 10 to 5 m/s lower then the maximum reachable speeds.

Parameter	**Symbol**	**Value / Range**	**Unit**
Minimum Speed	V_{min}	[V_{max} - 10, V_{max} - 5]	m/s
Maximum Speed	V_{max}	[15, 25] [8]	m/s

Table 5.3: Specific parameters for ATM simulation of fixed wing

Specific parameters for the rotorcraft UAV to be used for the flight test are given by table 5.4. The custom build rotorcraft is limited to a maximum airspeed of 5 m/s as can be found in the table.

Parameter	**Symbol**	**Value / Range**	**Unit**
Minimum Speed	V_{min}	0	m/s
Maximum Speed	V_{max}	5	m/s

Table 5.4: Specific parameters for flight test of rotorcraft

Specific parameters for the fixed wing UAVs to be used for the flight test are given by table 5.5. A commercially available Parrot Disco [13] will be used as fixed wing during the flight test experiment.

Parameter	**Symbol**	**Value / Range**	**Unit**
Minimum Speed	V_{min}	7	m/s
Maximum Speed	V_{max}	16.67 [13]	m/s

Table 5.5: Specific parameters for flight test of fixed wing.

5.2. ATM Simulation Experiments

Several simulations will be performed in an ATM simulation in order to test the performance of the applied CD&R method. The experiments are designed according to a set of hypotheses defined in section 5.2.2 in order to accomplish the research objective given in section 1.1. Dependent and independent variables that will be measured and controlled during the simulations are given in section 5.2.1. The simulation experiments to be performed are described by section 5.2.3. Assumptions and limitations regarding the simulation experiments can be found in section 5.2.4. Finally, the expected form of the results is described in section 5.2.5.

5.2.1. Variables

This section describes the independent variables that will be controlled during the simulated test series described in section 5.2.3. The dependent performance parameters that are used to measure the performance of the CD&R method are described afterwards.

Independent Parameters The independent variables being set during the experimental test series described in section 5.2.3 are the wind direction. wind speed, geofence geometry, initial UAV position vectors and initial UAV velocity vectors.

Dependent Performance Parameters The performance of the applied CD&R algorithm is expressed by the performance parameters given by equations 5.1 and 5.2.

The performance parameter given by equation 5.1 is the Intrusion Rate of the Protected Zone (IRPZ) for a given test series i as given by table 5.6 in section 5.2.3. The n_{sim_i} variable is the number of simulations performed in test series i. The n_{LoS_i} parameter is the number of experiments where a LoS has been detected in test series i. The IPRZ can take values between 0 and 1 for which the highest value represents the best performance.

The performance parameter given by equation 5.2 is the Violation Rate of the Geofence (VRG). The n_{gv_i} variable is the number of times a geofence has been violated during test series i. The range of the VRG is between -1 and 1 as two aircraft per simulation can violate the geofence. The higher the VRG the better the performance of the CD&R algorithm regarding geofence violations.

$$IRPZ_i = \frac{n_{sim_i} - n_{LoS_i}}{n_{sim_i}} \tag{5.1}$$

$$VRG_i = \frac{n_{sim_i} - n_{gv_i}}{n_{sim_i}} \tag{5.2}$$

5.2.2. Hypotheses

The experiments to be performed are shaped by a set of null hypotheses that are discussed in this section. The set of hypotheses is composed in order to accomplish the research objective as introduced in section 1.1 and restated below.

"The research objective is to contribute to a robust CD&R algorithm to be used on UAVs, regarding how to adapt existing CD&R techniques in order to provide an implicitly coordinated tactical CD&R approach, taking into account the ***limitations of geofences combined with wind*** *by defining a set of avoidance rules to be assessed by simulations and flight tests implementing adaptations of existing implicitly coordinated tactical CD&R algorithms developed for manned aviation."*

The effect of the geofences and wind on the performance of the CD&R method are a vital part to test during this research. Therefore five hypotheses are defined that will be tested to measure the performance of the method.

Hypothesis 1. The IRPZ of the CD&R method is negatively correlated with the implementation of geofences within the CD&R method.

It is expected that the implementation of geofences within the CD&R algotithm will negatively affect the IRPZ as the ARV decreases and the FRV increases. This means that there is less available velocity space to resolve a conflict, thus increasing the probability to encounter a LoS.

Hypothesis 2. The IRPZ and VRG of the CD&R method with geofences implemented are negatively correlated with the size of the geofenced area.

The IRPZ and VRG are expected to be negatively correlated with the area covered by the geofence. The IRPZ is expected to go down for a smaller geofenced area since the allowed manoeuvre space in terms of the ARV decreases as it is more likely that the UAV is acting closer to the geofence. In in appendix section A.2.1 can be found that when the ownship is acting closer to a geofence segment, the size of the geofence VO increases which will result in a smaller ARV. The VRG is also expected to be negatively correlated with the area covered by a geofence as the absolute manoeuvring space is smaller due to the enclosed airspace in which the avoidance manoeuvre needs to be performed. Thus it is more likely that a geofence will be violated within smaller airspaces.

Hypothesis 3. The IRPZ of the CD&R method is not correlated with wind speed.

A constant wind speed is expected to have no effect on the IRPZ of the CD&R method as the ARV in the body fixed reference frames of the conflicting vehicles does not change by adding wind.

Hypothesis 4. The IRPZ and VRG of the CD&R method with geofences implemented is negatively correlated with wind speeds.

Wind adds extra constraints on the earth fixed reference system. The turn radius changes in the earth fixed reference system due to wind which add extra constraints on the direction in which an avoidance manoeuvre can be performed which will negatively affect the IRPZ. Furthermore, the change that an air vehicle is blown over a geofence segment is also increased which would negatively influence the VRG.

Hypothesis 5. The IRPZ and VRG of the CD&R method with geofences implemented is negatively correlated with the distance to the geofence when a conflict is detected.

Finally, it is expected that when a distance with respect to a geofence at the moment a conflict is detected will negatively influence the IRPZ and VRG. This is because the size of a VO emerged from a geofence segment is negatively correlated with the distance to that geofence segment as can be found in appendix section A.2.1. This will negatively affect the ARV which will reduce the solution space which will negatively influence the IRPZ. Furthermore, it is likely that the chance an UAV crosses a geofence segment is higher when its position is closer to it which will negatively influence the VRG.

5.2.3. Experiments

A number of steps should be taken to be able to test the five hypotheses given in section 5.2.2. The first step is to generate a set of n_1 semi-random UAV scenarios in which two UAVs will encounter a horizontal conflict. Secondly, for each scenario a set of n_2 convex geofences with four vertices for both UAVs will be generated to test the influence of the geofence on the CD&R algorithm. Finally, a set of n_3 wind scenarios is to be generated in order to test the influence of wind on the performance of the CD&R algorithm.

Combining the conflict scenarios, geofences and wind conditions will result in the test matrix given by table 5.6. Each combination of conflict scenario, geofences and wind conditions will be tested resulting in a total number of $n_1 \cdot n_2 \cdot n_3$ scenarios to be performed in simulation for each candidate resolution strategy given in section 3.4.3.

Test series	Experiment number	UAV Scenario	Geofence Scenario	Wind Scenario
1	$[\mathbf{1}, \mathbf{n_1}]$.0.0	$[\mathbf{1}, \mathbf{n_1}]$	None	None
2	$[\mathbf{1}, \mathbf{n_1}].[\mathbf{1}, \mathbf{n_2}]$.0	$[\mathbf{1}, \mathbf{n_1}]$	$[\mathbf{1}, \mathbf{n_1}].[\mathbf{1}, \mathbf{n_2}]$	None
3	$[\mathbf{1}, \mathbf{n_1}]$.0.$[\mathbf{1}, \mathbf{n_3}]$	$[\mathbf{1}, \mathbf{n_1}]$	None	$[\mathbf{1}, \mathbf{n_3}]$
4	$[\mathbf{1}, \mathbf{n_1}].[\mathbf{1}, \mathbf{n_2}].[\mathbf{1}, \mathbf{n_3}]$	$[\mathbf{1}, \mathbf{n_1}]$	$[\mathbf{1}, \mathbf{n_1}].[\mathbf{1}, \mathbf{n_2}]$	$[\mathbf{1}, \mathbf{n_3}]$

Table 5.6: Experimtents to be performed in an ATM simulator

Tests will be performed in four test series as can be read from table 5.6. Each tests series is meant to measure performance of the CD&R algorithm by varying conflict scenarios, geofences and wind. The first test series is meant in order to measure the performance of the baseline CD&R method without the influence of geofences and wind conditions. The second test series is meant to measure the performance of the CD&R method with geofences implemented. The performance of the algorithm with geofences can be compared with respect to the baseline algorithm in order to determine the influence of a geofence in terms of its size and distance with respect to an UAV. The third test series measures the influence of wind on the performance of a CD&R algorithm with respect to the baseline situation. Finally, the fourth test series will be performed in order to measure the influence of wind on the performance of a CD&R method in which geofences are implemented.

5.2.4. Limitations and Assumptions

There are some limitations identified and some assumptions made regarding the ATM simulations. Those limitations and assumptions are listed below:

- The simulated flight models may not represent the real UAV dynamics.
- The simulated wind is constant and contains no turbulence.
- There is no corruption or delay in reception of state information of an intruder.
- Avoidance manoeuvres are only performed in the horizontal plane.

5.2.5. Results

The results of the experiments discussed in section 5.2.3 will be presented in terms of the IRPZ and VRG performance parameters of the CD&R method in order to test the five hypotheses given in section 5.2.2. The estimated probability and variance of the IRPZ will be calculated for each test series given in table 5.6 for each applied resolution rule-set. The estimated probability and variance of the VRG will be calculated for test series 2 and 4 in which geofences have been implemented.

In addition, in order to test the hypothesis, the results will be presented the following way corresponding to each hypothesis:

1. The IRPZ of the base CD&R algorithm with respect to the IRPZ of the CD&R algorithm with geofences implemented needs to be assessed in order to test the first hypothesis. Therefore the results of test series 1 and 2 will be compared with each other by means of scatter plots where the test number is plotted on the horizontal axis against the minimum distance at the CPA d_{CPA} on the vertical axis. All d_{CPA} values lower than the R_{PZ} can be classified as a LoS.

2. The second hypothesis can be tested by two types of scatter plots constructed from the data generated in test series 2. The first scatter plot scatters the size of the geofenced area on the horizontal axis versus the minimum distance encountered at CPA d_{CPA} on the vertical axis. The second scatter plots gives the geofenced area on the horizontal axis versus the minimum encountered distance with respect to the geofence on the vertical axis in order to visualise the VRG. A geofence violation can be seen in the plot when the minimum distance to the geofence encountered is negative.

3. The third hypothesis can be tested by measuring the IRPZ of the base CD&R algorithm tested in test series 1 with respect to the IRPZ of the CD&R algorithm with wind implemented as performed in test series 3. A plot scattering the test number on the horizontal axis versus the minimum distance to the CPA d_{CPA} on the vertical axis for both test series gives insight in the performance of the algorithm in terms of the total number of violations of the horizontal PZ.

4. The fourth hypothesis can be tested comparing the performance parameters of test series 2 versus test series 3. Two types of scatter plots will be generated for both test series in order to measure performance in terms of IPRZ and VRG. The first scatter plot gives the test number on the horizontal axis versus the minimum distance to the CPA d_{CPA} on the vertical axis. The second plot gives the test number on the horizontal axis versus the minimum encountered distance d_{geo} with respect to a geofence on the horizontal axis.

5. The fifth hypothesis can be tested by generating two types of scatter plots out of test series 2. The first diagram is a scatter plot plotting the distance of the UAV with respect to the geofence when a conflict has been detected on the horizontal axis versus the minimum distance to the closest point of approach d_{CPA} on the vertical axis. The second plot scatters the distance of the UAV with respect to the geofence when a conflict has been detected on the horizontal axis versus the minimum distance to the geofence on the vertical axis.

5.3. Flight Test Validation

A set of flight tests will be performed in order to validate the ATM simulations as discussed in section 5.2. The ATM simulation will be validated in terms of applied flight models and behaviour of the CD&R algorithm running on-board of the UAVs involved in the flight test. A pre defined scenario that has been tested in simulation will be tested in a real flight test. A set of conflict types will be tested by simulating intruders to verify the applicability and behaviour of the CD&R method on a real UAV. However, legal regulations have to be met in order to perform flight tests with an UAV. The vehicle should for example stay withing Visual Line of Sight (VLOS) during the flight tests, which excludes a range of scenarios that have been tested in simulation. Secondly, due to the fact that flight tests take a lot of time, only a limited number of scenarios will be performed in order to verify the simulations.

The limitations and assumptions regarding flight tests are given below.

Limitations and assumptions

- Airspace is limited in size for the flight tests due to safety and regulations.
- Only a limited amount of UAVs can be tested due to availability of those UAVs in the research laboratory.
- There can be corruption or delay in reception of state information send by intruders.
- There is only a limited number of flight tests and scenarios possible due to operational constraints.
- Avoidance manoeuvres are only performed in the horizontal plane.
- The test UAV should stay withing VLOS.

5.4. Outcome and Relevance

The flight test data logs will be used in order to verify the simulation regarding the UAV dynamics and flight behaviour with the CD&R algorithm activated. A simple scenario with a single intruder and predefined geofence will be performed in simulation and flight test in order to verify the simulation.

The outcome of this research project could be relevant for the NextGen and U-Space projects in order to have data on reliability of such a CD&R algorithm in the first place. Secondly, no research has been done before that includes geofences in a dynamic CD&R algorithm. In the third place, recommendations on a minimum geofence size for a drone can be made such that it can perform a successful avoidance manoeuvre with an acceptable probability of success. Finally, recommendations will be made on the the steps to take next by future researchers.

6 Conclusion

In line with the development of the UTM system, a tactical CD&R method should be implemented for UAVs in the near future. It is therefore important to implement additional constraints that hold for UAVs in a CD&R method. In the first place, a major constraint that applies to UAV operations is that missions should be performed within a horizontally geofenced airspace. This means that UAVs should perform their avoidance manoeuvres within this constrained airspace. Secondly, wind has a greater influence on the UAV's flightpath as drones fly at lower speeds than is done by manned air vehicles.

This research aims to investigate the performance of a velocity obstacle based CD&R method in terms of predicting the chance of violating the PZ of an intruder for a single conflict pair within a horizontally geofenced airspace with the presence of wind. Also the performance in terms of geofence violations will be measured. A SSD will be extended with geofences as velocity obstacles and used to find possible resolutions within the allowed reachable velocity space. Simulations of the velocity obstacle based CD&R method will be performed with different resolution rule-sets that have already been tested by researchers before. Next, a new rule-set can be implemented and tested to try to improve the performance of the velocity obstacle based CD&R method compared to the other rule-sets. Finally, recommendations can be made on the implementation of an implicit coordinated, tactical, velocity obstacle based CD&R method to be applied on UAVs.

The research is divided in seven research activities. This preliminary thesis report discusses the literature review, the selected rule-sets for conflict resolution and the implementation of geofences as VOs on a SSD. The ATM simulation software, in-flight CD&R software, result analysis and performance evaluation will be discussed in the final thesis report of this research.

It is expected that the implementation of geofences as VOs on a SSD will negatively influence the performance of the CD&R method in terms of the chance of a PZ intrusion. It has been found out that the distance of the ownship with respect to the geofence at the moment a conflict has been detected has a negative correlation with the size of the VO of that geofence. This means that the manoeuvring space near geofences reduces drastically. Those effects will be further investigated in the next phase of this research. This project strives for the development of a new conflict resolution rule-set that can improve the performance of the CD&R method with respect to other applied rule-sets.

A

VOs of Geofences

This appendix gives additional insight in VOs of geofences induced by conflicts with intruders. How the coordinates of geofence VOs are determined can be read in section A.1. Finally, section A.2 gives insight in correlations between the dependent and independent geofence VO parameters.

A.1. Construction of Geofence VOs

This section explains how the geofence VOs are constructed for the three types of geometries identified in section 4.2. The meaning of the parameters and the general equation of a VO of a geofence segment can be found in section 4.1. A VO is constructed depending on the sign of the b^2 parameter. Information regarding the state of the intruder and geofence geometry are needed in order to construct a VO of a geofence segment. The algorithms to construct objects of an intruder and geofence segment are given by algorithm 1 and 2 respectively. The intruder object contains the position and speed vector of the intruder. The geofence segment object contains the distance to the geofence, the rotation of the geofence with respect to the East North reference system and a parallel and perpendicular unit vector with respect to the geofence segment. Two arbitrary points on a geofence are needed as input to generate a geofence segment object.

Algorithm 1 Generates an intruder object

function SET_INTRUDER($\vec{d}_{int}$, $\vec{v}_{int}$)
    $Intruder \leftarrow$ **empty intruder object**
    $Intruder.\vec{d} \leftarrow \vec{d}_{int}$
    $Intruder.\vec{v} \leftarrow \vec{v}_{int}$
    return $Intruder$

Algorithm 2 Generates a geofence segment object

function SET_GEOFENCE_SEGMENT($\vec{p}_1$, $\vec{p}_2$)
    $Geofence\_Segment \leftarrow$ **empty Geofence Segment object**
    $\delta\vec{p} \leftarrow \vec{p}_2 - \vec{p}_1$
    $\phi \leftarrow \text{atan2}\left(\delta\vec{p}_x, \delta\vec{p}_y\right)$
    $R \leftarrow \begin{bmatrix} \cos(\phi) & -\sin(\phi) \\ \sin(\phi) & \cos(\phi) \end{bmatrix}$
    $Geodence\_Segment.\phi \leftarrow \phi$
    $Geofence\_Segment.\hat{x} \leftarrow R \begin{bmatrix} 1 \\ 0 \end{bmatrix}$ ▷ This is the $\hat{x}'$ unit vector described in section 4.1
    $Geofence\_Segment.\hat{y} \leftarrow R \begin{bmatrix} 0 \\ 1 \end{bmatrix}$ ▷ This is the $\hat{y}'$ unit vector described in section 4.1
    $Geofence\_Segment.d_{geo} \leftarrow -\vec{p}_1 \cdot Geofence\_Segment.\hat{y}$
    return $Geofence\_Segment$

Parameters for a geofence VO can be generated from the intruder and geofence segment. All these parameters will be saved in a VO parameter object which is performed by algorithm 3. The VO parameter object contains the squared values of the a and b semi major axes of the VO objects. Also the coordinates of the center points along the $\hat{x}''$ and $\hat{y}''$ primary unit vectors are saved in the VO parameter object.

Algorithm 3 Generates parameters for a VO of a geofence segment

function SET_GEOFENCE_VO_PARAMS($Intruder, Geofence\_Segment$)

$Geofence\_VO\_Params \leftarrow$ **empty Geofence VO Params object**

$\hat{x}' \leftarrow Geofence\_Segment.\hat{x}$

$\hat{y}' \leftarrow Geofence\_Segment.\hat{y}$

$d_{geo} \leftarrow Geofence\_Segment.d_{geo}$

$\vec{d}_{int} \leftarrow Intruder.\vec{d}$

$\vec{v}_{int} \leftarrow Intruder.\vec{v}$

$\phi' \leftarrow \frac{1}{2}\,\text{atan2}\left(-\vec{d}_{int}\cdot\hat{x}', \vec{d}_{int}\cdot\hat{y}'\right)$

$R' \leftarrow \begin{bmatrix} \cos\left(\phi'\right) & -\sin\left(\phi'\right) \\ \sin\left(\phi'\right) & \cos\left(\phi'\right) \end{bmatrix}$

$\hat{x}'' \leftarrow R'\hat{x}'$

$\hat{y}'' \leftarrow R'\hat{y}'$

$C_1 \leftarrow 1 + \sin\left(\phi'\right)\frac{\vec{d}_{int}\cdot\hat{x}''}{d_{geo}}$

$C_2 \leftarrow 1 + \cos\left(\phi^i\right)\frac{\vec{d}_{int}\cdot\hat{y}''}{d_{geo}}$

$C_3 \leftarrow -2\left(\vec{v}_{int}\cdot\hat{x}''\right) - \sin\left(\phi'\right)\frac{\vec{d}_{int}\cdot\vec{v}_{int}}{d_{geo}}$

$C_4 \leftarrow -2\left(\vec{v}_{int}\cdot\hat{y}''\right) - \cos\left(\phi'\right)\frac{\vec{d}_{int}\cdot\vec{v}_{int}}{d_{geo}}$

$C_{x''} \leftarrow -\frac{C_3}{2C_1}$

$C_{y''} \leftarrow -\frac{C_4}{2C_2}$

$Geofence\_VO\_Params.a^2 \leftarrow \frac{-|\vec{v}_{int}|^2 + C_2 C^2_{y''}}{C_1} + C^2_{x''}$

$Geofence\_VO\_Params.b^2 \leftarrow \frac{-|\vec{v}_{int}|^2 + C_1 C^2_{x''}}{C_2} + C^2_{y''}$

$Geofence\_VO\_Params.C_x \leftarrow C_{x''}$ ▷ This is the $C_{x''}$ parameter described in section 4.1

$Geofence\_VO\_Params.C_y \leftarrow C''_y$ ▷ This is the $C_{y''}$ parameter described in section 4.1

return $Geofence\_VO\_Params$

The geometry of a geofence VO depends on the sign of the b^2 variable in the VO parameter object. The possible geometries of a geofence VO are parabolic, elliptical or hyperbolic. The algorithm used to construct this VO is given by algorithm 4. The input parameter N is the number of points that the polygon to be constructed of the VO consists.

The algorithms that are used to construct polygons of parabolic, elliptical or hyperbolic VOs are explained by sections A.1.1, A.1.2 and A.1.3 respectively.

A.1.1. Construction of Parabolic Geofence VOs

A parabolic VO of a geofence segment will be approximated by a hyperbolic VO with a big value of b. A parabolic VO can exists when an elliptical VO transitions to a hyperbolic VO or backwards. However, it is unlikely that in reality a parabolic VO has to be constructed as b goes to infinity for only a specific combination of input parameters.

The algorithm used to construct a parabolic VO of a geofence segment is given by algorithm 5. An explanation of the parameters used in order to construct the parabolic VO can be found in section A.1.3.

A.1.2. Construction of Elliptical Geofence VOs

The parametric equation for a ellipse is given by equation A.1. Polygon points of a elliptical geofence VO can be constructed using this parametric equation.

Algorithm 4 Construct a geofence VO and classify the geometry as ellipse, parabola or hyperbola

function CONSTRUCT_GEOFENCE_VO(N, V_{max}, $Geofence\_Segment$, $Geofence\_VO\_Params$)
  $a^2 \leftarrow Geofence\_VO\_Params.a^2$
  $b^2 \leftarrow Geofence\_VO\_Params.b^2$
  if $b^2 \to \infty$ **then** ▷ Parabolic VO, see section A.1.1
    $Geofence\_VO \leftarrow$ CONSTRUCT_PARABOLIC_VO($N, Geofence\_VO\_Params, Geofence\_Segment$)
  else if $b^2 > 0$ **then** ▷ Elliptical VO, see section A.1.2
    $Geofence\_VO \leftarrow$ CONSTRUCT_ELLIPTICAL_VO($N, Geofence\_VO\_Params, Geofence\_Segment$)
  else ▷ Hyperbolic VO, see section A.1.3
    $Geofence\_VO \leftarrow$ CONSTRUCT_HYPERBOLIC_VO($N, Geofence\_VO\_Params, Geofence\_Segment, V_{max}$)
return $Geofence\_VO$ ▷ The output of this equation is a polygon of coordinates

Algorithm 5 Constructs the points of a parabolic geofence VO polygon

function CONSTRUCT_HYPERBOLIC_VO(N, $Geofence\_VO\_Params$, $Geofence\_Segment$, V_{max})
  $a \leftarrow \sqrt{Geofence\_VO\_Params.a^2}$
  $b \leftarrow$ **big value**
  $\phi' \leftarrow Geofence\_VO\_Params.\phi$
  $\phi_{total} \leftarrow \phi' + Geofence\_Segment.\phi$
  $t_{max} \leftarrow \ln\left(\frac{2V_{max}+\sqrt{4V_{max}^2+a^2}}{a}\right)$
  $t_{min} \leftarrow -t_{max}$
  $\delta t \leftarrow \frac{t_{max}-t_{min}}{N}$
  $polygon \leftarrow$ **empty polygon object** ▷ Polygon that can hold polygon points (x, y)
  for $i = 0$ **to** $N-1$ **do**
    $\gamma \leftarrow \delta t i$
    if $\phi' > 0$ **then** ▷ The hyperbola must be constructed for negative $\hat{x}''$ values
      $x'' \leftarrow -a\cosh(t) + Geofence\_VO\_Params.C_x$
    else ▷ The hyperbola must be constructed for positive $\hat{x}''$ values
      $x'' \leftarrow a\cosh(t) + Geofence\_VO\_Params.C_x$
    $y'' \leftarrow b\sinh(t) + Geofence\_VO\_Params.C_y$
    $x \leftarrow x''\cos(\phi_{total}) - y''\sin(\phi_{total})$ ▷ Rotate x'' back to (East, North) axis system
    $y \leftarrow x''\sin(\phi_{total}) + y''\cos(\phi_{total})$ ▷ Rotate y'' back to (East, North) axis system
    add (x, y) to $polygon$
  return polygon

$$\begin{cases} x(t) = a\cos(t) \\ y(t) = b\sin(t) \end{cases} \quad t \in [0, 2\pi] \tag{A.1}$$

The algorithm that is used in order to generate a polygon of an elliptical VO of a geofence segment is given by algorithm 6.

A.1.3. Construction of Hyperbolic Geofence VOs

Parametric equations of a horizontal hyperbola are given by equations A.2 and A.3. The hyperbolic geofence VOs are located in the half plane of the SSD at the side of the corresponding geofence segment as a geofence segment can only be crossed when the position of the ownship converges towards the geofence segment. Therefore, equation A.2 should be used for positive values of ϕ' and equation A.3 should be used for negative values of ϕ' to construct hyperbolic geofence VOs.

$$\begin{cases} x(t) = -a\cosh(t) = -\frac{a}{2}\left(e^t + e^{-t}\right) \\ y(t) = b\sinh(t) = \frac{b}{2}\left(e^t - e^{-t}\right) \end{cases} \quad t \in \langle -\infty, \infty \rangle \tag{A.2}$$

$$\begin{cases} x(t) = a\cosh(t) = \frac{a}{2}\left(e^t + e^{-t}\right) \\ y(t) = b\sinh(t) = \frac{b}{2}\left(e^t - e^{-t}\right) \end{cases} \quad t \in \langle -\infty, \infty \rangle \tag{A.3}$$

Algorithm 6 Constructs the points of an elliptical geofence VO polygon

function CONSTRUCT_ELLIPTICAL_VO(N, $Geofence\_VO\_Params$, $Geofence\_Segment$)
 $a \leftarrow \sqrt{Geofence\_VO\_Params.a^2}$
 $b \leftarrow \sqrt{Geofence\_VO\_Params.b^2}$
 $\phi_{total} \leftarrow Geofence\_VO\_Params.\phi + Geofence\_Segment.\phi$
 $\delta\gamma \leftarrow \frac{2\pi}{N}$
 $polygon \leftarrow$ **empty polygon object** ▷ Polygon that can holds polygon points (x, y)
 for $i = 0$ **to** $N-1$ **do**
  $\gamma \leftarrow \delta\gamma i$
  $x'' \leftarrow a\cos(\gamma) + Geofence\_VO\_Params.C_x$
  $y'' \leftarrow b\sin(\gamma) + Geofence\_VO\_Params.C_y$
  $x \leftarrow x''\cos(\phi_{total}) - y''\sin(\phi_{total})$ ▷ Rotate x'' back to (East, North) axis system
  $y \leftarrow x''\sin(\phi_{total}) + y''\cos(\phi_{total})$ ▷ Rotate y'' back to (East, North) axis system
  add (x, y) to $polygon$
 return polygon

The maximum length of the hyperbolic VO along the $\hat{x}''$ unit vector is twice the maximum reachable airspeed V_{max} of the ownship to fit completely in the SSD that is constrained by V_{max}. Therefore the maximum and minimum values of parameter t in order to construct the VO can be calculated using equations A.4 and A.5 respectively. The coordinate of the hyperbola along the $\hat{x}''$ unit vector is twice the value of V_{max} for t_{min} and t_{max}.

$$t_{max} = \ln\left(\frac{2V_{max} + \sqrt{4V_{max}^2 + a^2}}{a}\right) \tag{A.4}$$

$$t_{min} = -t_{max} \tag{A.5}$$

The algorithm used in order to construct the hyperbolic VO polygon for a geofence segment is given by algorithm 7.

Algorithm 7 Constructs the points of an hyperbolic geofence VO polygon

function CONSTRUCT_HYPERBOLIC_VO(N, $Geofence\_VO\_Params$, $Geofence\_Segment$, V_{max})
 $a \leftarrow \sqrt{Geofence\_VO\_Params.a^2}$
 $b \leftarrow \sqrt{-Geofence\_VO\_Params.b^2}$
 $\phi' \leftarrow Geofence\_VO\_Params.\phi$
 $\phi_{total} \leftarrow \phi' + Geofence\_Segment.\phi$
 $t_{max} \leftarrow \ln\left(\frac{2V_{max}+\sqrt{4V_{max}^2+a^2}}{a}\right)$
 $t_{min} \leftarrow -t_{max}$
 $\delta t \leftarrow \frac{t_{max}-t_{min}}{N}$
 $polygon \leftarrow$ **empty polygon object** ▷ Polygon that can hold polygon points (x, y)
 for $i = 0$ **to** $N-1$ **do**
  $\gamma \leftarrow \delta t i$
  if $\phi' > 0$ **then** ▷ The hyperbola must be constructed for negative $\hat{x}''$ values
   $x'' \leftarrow -a\cosh(t) + Geofence\_VO\_Params.C_x$
  else ▷ The hyperbola must be constructed for positive $\hat{x}''$ values
   $x'' \leftarrow a\cosh(t) + Geofence\_VO\_Params.C_x$
  $y'' \leftarrow b\sinh(t) + Geofence\_VO\_Params.C_y$
  $x \leftarrow x''\cos(\phi_{total}) - y''\sin(\phi_{total})$ ▷ Rotate x'' back to (East, North) axis system
  $y \leftarrow x''\sin(\phi_{total}) + y''\cos(\phi_{total})$ ▷ Rotate y'' back to (East, North) axis system
  add (x, y) to $polygon$
 return polygon

A.2. Geofence VO Correlations

This section describes correlations between some independent geofence VO parameters and dependent geofence VO parameters as described in section 5.2.1. Section A.2.1 gives the relationship between the distance of the ownship with respect to the geofence and the specific parameters of a geofence VO. Finally, section A.2.2 gives an overview of the shapes a geofence VO can take for a range of distances with respect to the geofence.

A.2.1. Effect of Distance with respect to the Geofence

This section gives the effects of the distance of the ownship with respect to a geofence segment on the VO induced by this geofence segment. A reference scenario has been used in order to generate plots that are presented in this section. The inputs given by table A.1 are used for the reference scenario.

Variable name	**Symbol**	**Value**	**Unit**
Intruder speed	$\vec{v}_{int}$ (East, North)	(-10, 0)	m/s
Geofence rotation	ϕ	$-\frac{\pi}{2}$	rad

Table A.1: Variables used for the reference scenario to generate plots regarding the effect of d_{geo} on geofence VO parameters

Five intruder reference positions are used in order to generate the plots presented in this chapter. Table A.2 gives the reference position of those reference intruders. Mind that those positions are relative to the ownship as the ownship is assumed to be located at the origin of the reference system.

Intruder number	**Position** (East, North) [m]
1	(100, 0)
2	(100, 100)
3	(0, 100)
4	(-100, 100)
5	(-100, 0)

Table A.2: Reference positions used for the intruders to generate plots regarding the effect of d_{geo} on geofence VO parameters

The geometrical situation of the reference scenario is depicted in figure A.1. The speed vectors of the intruders are directed towards the geofence segments at a velocity of 10 m/s as can be read from table A.1.

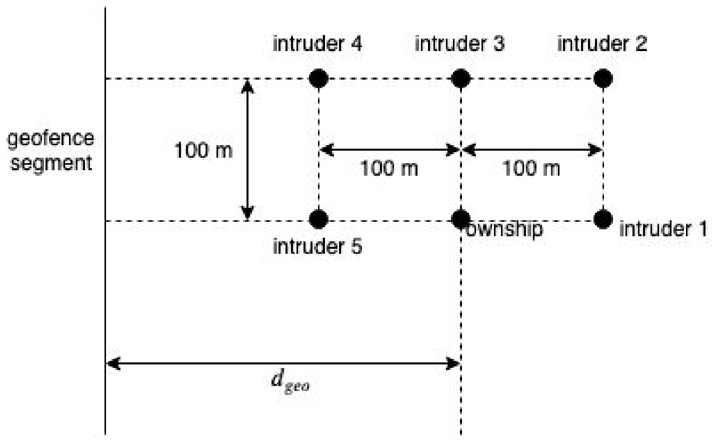

Figure A.1: Geometry of reference scenario used to generate plots regarding the effect of d_{geo} on geofence VO parameters

The diagrams given by figures A.2 and A.3 reflect the a^2 and b^2 parameters of a geofence VO for a range of values of d_{geo} respectively. It can be seen from the figures that for the given range of d_{geo} parameters the VOs are ellipse shaped as all plotted a^2 and b^2 parameters are positive. It can be concluded that the major axis of the ellipse shaped VO increase with a decreasing d_{geo}.

The diagrams given by figures A.4 and A.5 reflect the values of $C_x^{''}$ and $C_y^{''}$ of the ellipse shaped geofence VO for a range of d_{geo} values respectively. It can be seen that the $C_x^{''}$ value is most sensitive to d_{geo}. This can

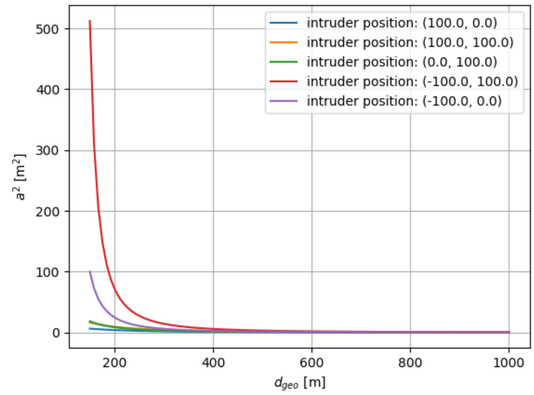

Figure A.2: d_{geo} versus a^2 for the reference scenario

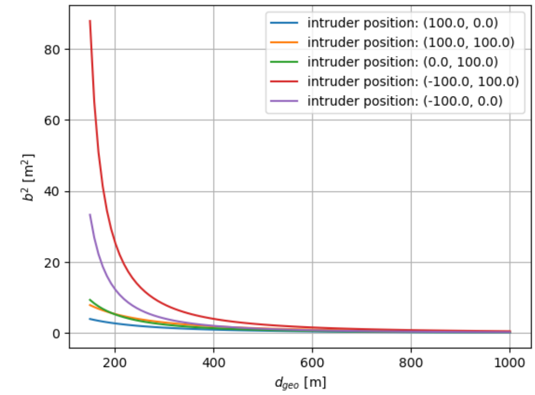

Figure A.3: d_{geo} versus b^2 for the reference scenario

be explained by the fact the the ellipse expands faster along the $\hat{x}_i''$ primary axis than along the $\hat{y}_i''$ primary axis as the value of a^2 is more sensitive to d_{geo} as can be seen in the diagram given by figure A.2.

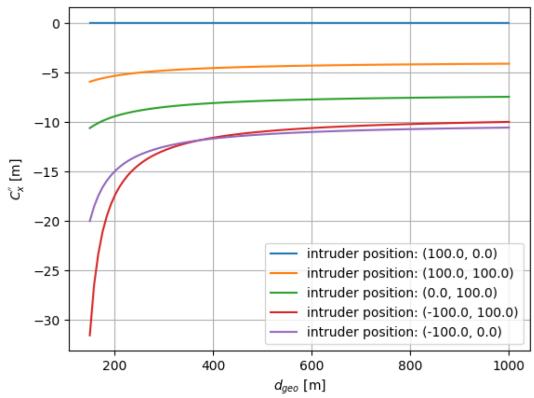

Figure A.4: d_{geo} versus C_x'' for the reference scenario

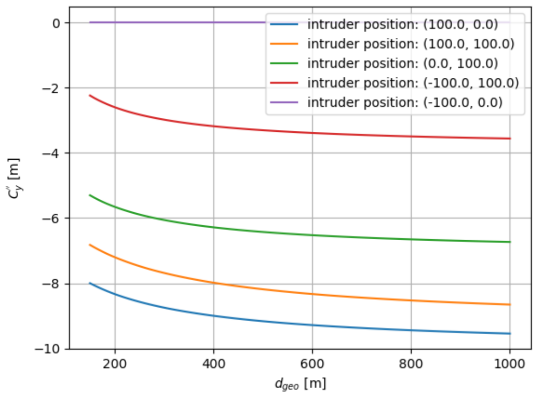

Figure A.5: d_{geo} versus C_y'' for the reference scenario

Finally, the area of the ellipse shaped geofence VO is plotted against d_{geo} as can be seen in figure A.6. The area enclosed by an ellipse is calculated using equation A.6. It can be concluded that the the area of the geofence VO and d_{geo} is negatively correlated.

$$\text{Ellipse area} = \pi ab \tag{A.6}$$

A.2.2. Effect of Distance with respect to the Geofence on the Geofence VO Shape

This section gives insight in the shapes a VO of a geofence segment can take. It was already discovered in section A.2.1 that the distance with respect to the geofence of the ownship has a big effect on the parameters that define a geofence VO. The most sensitive relative intruder position has been chosen to generate plots that are shown in this section. Therefore, intruder position 4 indicated in table A.2 and figure A.1 will be used to generate diagrams in this section. The variables for the reference scenario given by table A.1 are applied on the diagrams shown throughout this section.

Four diagrams are shown in this section giving the geometry of a geofence VO with varying distance of the ownship with respect to the geofence. Figure A.7 shows the elliptical geofence VO for a distance with respect to the geofence of 200 meters. Figures A.8 and A.9 show the elliptical geometry of a geofence VO for a distance with respect to the geofence of 175 and 150 respectively. It can be concluded from those figures that the size of the VO increases with decreasing distance of the ownship with respect to the geofence. Finally, figure A.10

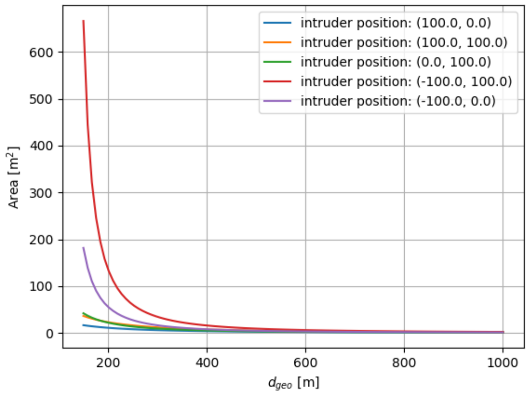

Figure A.6: d_{geo} versus area of elliptical geofence VO for the reference scenario

shows the hyperbolic geometry of a geofence VO for a distance with respect to the geofence of 100 meters. It can be seen that the geofence VO turned into a hyperbolic shape with a decreasing value of d_{geo} .

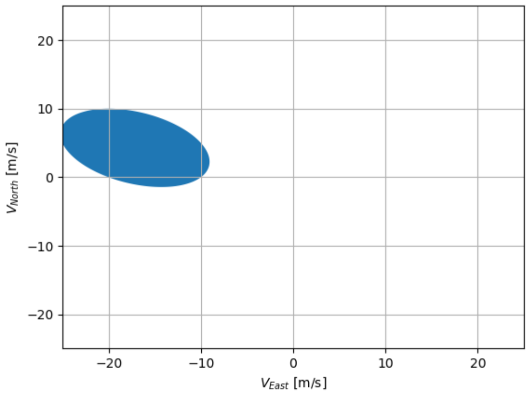

Figure A.7: The shape of a geofence VO for the reference scenario at d_{geo} = 200m and relative intruder position (-100, 100)

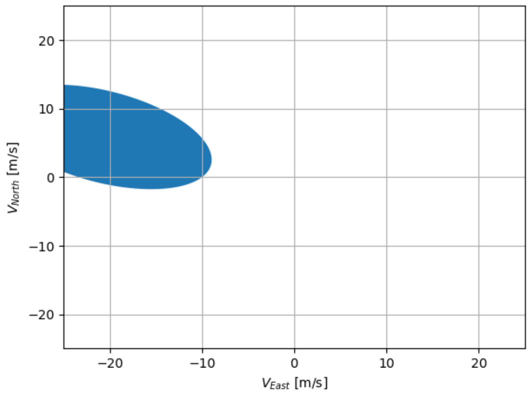

Figure A.8: The shape of a geofence VO for the reference scenario at d_{geo} = 175m and relative intruder position (-100, 100)

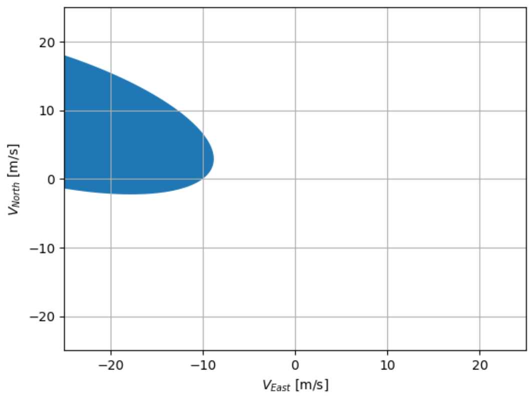

Figure A.9: The shape of a geofence VO for the reference scenario at d_{geo} = 150m and relative intruder position (-100, 100)

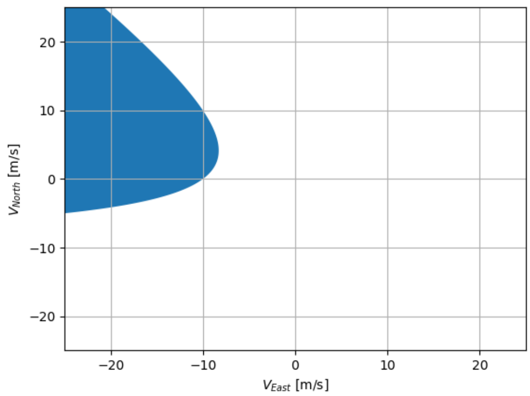

Figure A.10: The shape of a geofence VO for the reference scenario at d_{geo} = 100m and relative intruder position (-100, 100)

Bibliography

[1] S. Balasooriyan. Multi-aircraft Conflict Resolution using Velocity Obstacles. 2017.

[2] M. S. Eby. A Self-Organizational Approach for Resolving Air Traffic Conflicts. *The Lincoln Laboratory Journal*, 7(2):239–254, 1994.

[3] J. Ellerbroek, K. C. R. Brantegem, M. M. Van Paassen, N. De Gelder, and M. Mulder. Experimental evaluation of a coplanar airborne separation display. *IEEE Transactions on Human-Machine Systems*, 43(3): 290–301, 2013. ISSN 21682291. doi: 10.1109/TSMC.2013.2238925.

[4] J. M. Hoekstra, R. N.H.W. Van Gent, and R. C.J. Ruigrok. Designing for safety: The 'free flight' air traffic management concept. *Reliability Engineering and System Safety*, 75(2):215–232, 2002. ISSN 09518320. doi: 10.1016/S0951-8320(01)00096-5.

[5] Y. I. Jenie, E. J. Van Kampen, C. C. De Visser, J. Ellerbroek, and J. M. Hoekstra. Selective velocity obstacle method for deconflicting maneuvers applied to unmanned aerial vehicles. *Journal of Guidance, Control, and Dynamics*, 38(6):1140–1145, 2015. ISSN 07315090. doi: 10.2514/1.G000737.

[6] Y. I. Jenie, E. J. Van Kampen, C. C. De Visser, J. Ellerbroek, and J. M. Hoekstra. Three-dimensional velocity obstacle method for uncoordinated avoidance maneuvers of unmanned aerial vehicles. *Journal of Guidance, Control, and Dynamics*, 39(10):2312–2323, 2016. ISSN 07315090. doi: 10.2514/1.G001715.

[7] Y. I. Jenie, E. J. Van Kampen, J. Ellerbroek, and J. M. Hoekstra. Taxonomy of Conflict Detection and Resolution Approaches for Unmanned Aerial Vehicle in an Integrated Airspace. *IEEE Transactions on Intelligent Transportation Systems*, 18(3):558–567, 2017. ISSN 15249050. doi: 10.1109/TITS.2016.2580219.

[8] Y. I. Jenie, E. J. Van Kampen, J. Ellerbroek, and J. M. Hoekstra. Safety assessment of a UAV CDR system in high density airspace using monte carlo simulations. *IEEE Transactions on Intelligent Transportation Systems*, 19(8):2686–2695, 2018. ISSN 15249050. doi: 10.1109/TITS.2017.2758859.

[9] T. Jiang, J. Geller, D. Ni, and J. Collura. Unmanned Aircraft System traffic management: Concept of operation and system architecture. *International Journal of Transportation Science and Technology*, 5(3): 123–135, 2016. ISSN 20460430. doi: 10.1016/j.ijtst.2017.01.004. URL `http://dx.doi.org/10.1016/j.ijtst.2017.01.004`.

[10] P. Kopardekar, J. Rios, T. Prevot, M. Johnson, J. Jung, and J. E. Robinson. Unmanned aircraft system traffic management (UTM) concept of operations. *16th AIAA Aviation Technology, Integration, and Operations Conference*, pages 1–16, 2016.

[11] A. Martinoli, F. Mondada, N. Correll, and G. Mermoud. *Springer Tracts in Advanced Robotics: Preface*, volume 83 STAR. 2012. ISBN 9783642327223.

[12] G. A. Mercado Velasco, C. Borst, J. Ellerbroek, M. M. Van Paassen, and M. Mulder. The Use of Intent Information in Conflict Detection and Resolution Models Based on Dynamic Velocity Obstacles. *IEEE Transactions on Intelligent Transportation Systems*, 16(4):2297–2302, 2015. ISSN 15249050. doi: 10.1109/TITS.2014.2376031.

[13] Parrot. PARROT DISCO FPV. URL `https://www.parrot.com/us/drones/parrot-disco-fpv`. Accesed on 03/02/2020.

[14] B. Syd Ali. Traffic management for drones flying in the city. *International Journal of Critical Infrastructure Protection*, 26:100310, 2019. ISSN 18745482. doi: 10.1016/j.ijcip.2019.100310.

[15] C. Y. Tan, S. Huang, K. K. Tan, and R. S. H. Teo. Three Dimensional Collision Avoidance for Multi Unmanned Aerial Vehicles Using Velocity Obstacle. *Journal of Intelligent and Robotic Systems: Theory and Applications*, 97(1):227–248, 2020. ISSN 15730409. doi: 10.1007/s10846-019-01055-5.

[16] UAV Challenge. UAV Challenge Medical Rescue 2020 Competition Rules v5, 2020. URL `https://uavchallenge.org/medical-rescue/`. Accesed on 18/02/2020.

[17] S. B. J. Van Dam, M. Mulder, and M. M. van Paassen. Ecological interface design of a tactical airborne separation assistance tool. *IEEE Transactions on Systems, Man, and Cybernetics Part A:Systems and Humans*, 38(6):1221–1233, 2008. ISSN 10834427. doi: 10.1109/TSMCA.2008.2001069.